

# **MICROFABRICATION OF A MEMS PIEZORESISTIVE FLOW SENSOR - MATERIALS AND PROCESSES**

A Thesis  
Presented to  
The Academic Faculty

by

Avishek R. Aiyar

In Partial Fulfillment  
of the Requirements for the Degree  
Master of Science in Chemical Engineering

Georgia Institute of Technology  
August 2008

# MICROFABRICATION OF A MEMS PIEZORESISTIVE FLOW SENSOR - MATERIALS AND PROCESSES

Approved by:

Professor Mark G. Allen, Committee Chair  
Schools of Electrical and Computer  
Engineering and Chemical and  
Biomolecular Engineering  
*Georgia Institute of Technology*

Professor C.P. Wong  
School of Materials Science and Engineering  
*Georgia Institute of Technology*

Professor Sue Ann Bistrup Allen  
School of Chemical and Biomolecular  
Engineering  
*Georgia Institute of Technology*

Date Approved: 2nd July 2008

*“If you lead life the right way, karma will take care of itself,  
the dreams will come to you”*

*Randy Pausch, The Last Lecture*

## ACKNOWLEDGEMENTS

I owe this work to a lot of people, who have been a constant source of encouragement and support throughout my research.

I am and I will always remain indebted to my advisor, Professor Mark Allen, who has supported me through good times and bad. I have learnt more from him than I ever can by reading a thousand books. I am indeed proud and privileged to have him as my advisor.

I would like to thank Professor C.P. Wong and Professor Sue Ann Bidstrup Allen for serving on my thesis committee. I really appreciate their advice and their support. The classes I have taken with Professor Wong have been instrumental in enhancing my understanding of electronic materials and writing this thesis.

I would like to thank my colleagues and friends in the Microsensors and Microactuators (MSMA) group at the Georgia Institute of Technology for always entertaining this “curious guy”, popping at someone’s door and shooting a hundred questions. I made bonds here that will remain with me for life. Special thanks to Yong Kyu Yoon, for being ever so patient with me and for a being a wonderful friend and guide and Seong-Hyok Kim, my “partner-in-crime” in the MURI project, who has been great to work with. I would also like to express my deepest gratitude to Mr. Richard Shafer, our laboratory manager, who was always around to setup equipments for me at a moment’s notice, to help me with my experiments or to simply talk research with, and Mrs. Purnima Sharma, our laboratory administrator. Thanks also to all the staff at the MiRC, who made my stay a pleasurable one.

I am also thankful to all my group members for making every working day at



the MiRC a pleasure. Special thanks to Seong-O Choi, for being a wonderful lab-mate, friend and guide, Florian Herrault, for our everyday discussions on the Arsenal football club and French football (and research sometimes!), Chang-Hyeon Ji, for always being there to help me out, and Preston Galle, Maxine McClain, Yanzhu Zhao and Wenjun Xu, for simply being the nicest people I have known. I am also indebted to one of my best friends, Edward Park, for being just that. I consider myself extremely lucky to have met Nisarga Naik, the elder sister I never had. I cannot thank her enough for supporting me, chiding me, spoiling me and being my local crisis manager.

I am extremely grateful to my PhD advisor, Professor Elsa Reichmanis, without whose support and cooperation this work would have remained in the laboratory. I am extremely fortunate to have got the opportunity to work for both Professor Allen and Professor Reichmanis, wonderful people and wonderful advisors.

Finally, I would like to thank my family - my parents, whose dream this was. I am indeed blessed to have got such parents who gave me limitless freedom to do whatever I wanted. To my brother Arvind, who has been a great brother and guide and my sister-in-law, Sukanya.

To my grandmother, who long left the earth for greener pastures, I dedicate this thesis. She has been the single greatest influence of my life.

# TABLE OF CONTENTS

ACKNOWLEDGEMENTS . . . . .	iv
LIST OF TABLES . . . . .	ix
LIST OF FIGURES . . . . .	xi
SUMMARY . . . . .	xvi
I INTRODUCTION . . . . .	1
1.1 Biomimetics . . . . .	2
1.2 Biomimetics, MEMS and flow sensors . . . . .	3
1.3 Outline . . . . .	6
II PIEZORESISTIVE MATERIALS IN MEMS AND REVIEW OF MEMS FLOW SENSORS . . . . .	8
2.1 Piezoresistive thin films and materials . . . . .	8
2.1.1 Metal thin film piezoresistors . . . . .	9
2.1.2 Doped silicon piezoresistors . . . . .	11
2.1.3 Conductive composite polymer piezoresistors . . . . .	13
2.2 Flow sensors . . . . .	15
2.2.1 Silicon MEMS flow sensors . . . . .	16
2.2.2 Polymer MEMS flow sensors . . . . .	19
III OBJECTIVES AND APPROACHES . . . . .	23
3.1 Objectives . . . . .	23
3.2 Approaches . . . . .	23
3.2.1 Design principles and transduction . . . . .	24
IV METAL TRANSFER MICROMOLDING . . . . .	28
4.1 Fabrication process . . . . .	31
4.1.1 SU-8 photolithography . . . . .	31
4.1.2 Molding and microtransfer printing . . . . .	33
4.1.3 Final device fabrication . . . . .	35

4.2	Discussion . . . . .	35
4.3	Testing results . . . . .	38
4.4	Technical issues with MTM . . . . .	40
V	DISSOLVING MOLD METAL TRANSFER MICROMOLDING . . . . .	43
5.1	Identifying problems with conventional MTM . . . . .	43
5.2	Fabrication process . . . . .	45
5.3	Dissolving molds-materials and processing . . . . .	47
5.3.1	Polymethylmethacrylate (PMMA) molds . . . . .	48
5.3.2	Polyacrylic Acid (PAA) molds . . . . .	51
5.4	Testing: Static deflection and Wind tunnel . . . . .	57
5.5	Analysis of performance of MTM and dissolving mold process based devices-Failure modes . . . . .	66
5.5.1	Low sensitivity . . . . .	66
5.5.2	Effect of thin film metal quality on device performance . . . . .	68
VI	LASER MICROFABRICATION AND CONDUCTIVE ELASTOMER COM- POSITES . . . . .	72
6.1	Device design and sensing principle . . . . .	74
6.2	Materials . . . . .	75
6.2.1	Kapton <sup>®</sup> . . . . .	75
6.2.2	Carbon black-elastomer composite - characterization of the material properties . . . . .	76
6.3	Fabrication process . . . . .	87
6.3.1	CO <sub>2</sub> laser machining of the base . . . . .	88
6.3.2	Lamination of Kapton <sup>®</sup> . . . . .	91
6.3.3	Microstenciling of the conductive composite . . . . .	92
6.3.4	Patterning of electrodes . . . . .	96
6.3.5	Improving the flow-structure interaction-deposition of stress inducing layers . . . . .	100
6.3.6	Release of the microtuft structures . . . . .	104
6.3.7	Final device . . . . .	105

6.4	Wind tunnel testing . . . . .	107
6.4.1	Results . . . . .	107
6.4.2	Analysis of device performance . . . . .	111
6.5	Stress induced curvature - Intrinsic or thermomechanical stress? . .	117
VII	CONCLUSION . . . . .	130
7.1	Summary and contributions . . . . .	130
7.2	Future work . . . . .	133
	REFERENCES . . . . .	135

## LIST OF TABLES

1	Transverse and longitudinal piezoresistance coefficients in doped silicon resistors oriented in the [110] direction . . . . .	12
2	Process conditions for 3 layer SU-8 master fabrication . . . . .	33
3	Process conditions for surface treatment of the metalized PDMS mold	34
4	Number of baking steps seen by different layers in the 3 layer process (Layer 1 is the bottommost layer) . . . . .	36
5	Deflection testing results. ‘-’ indicate intermediate deflections which were not recorded . . . . .	39
6	Cyclic deflection testing results. $D_i$ is the starting deflection; $D_f$ is the final deflection; $R_i$ is the initial resistance corresponding to $D_i$ ; $R_f$ is the final resistance corresponding to $D_f$ . . . . .	39
7	PDMS spray coating parameters . . . . .	55
8	Device response “zones” - Experiments # 1 and 2 . . . . .	64
9	Device response “zones” - Experiment # 3 . . . . .	64
10	Summary of device performance. $R_i$ is the resistance at the start of the expt., $R_m$ is the maximum change in resistance, $R_h$ is the baseline resistance hysteresis before and after the experiment, $T_s$ is the time taken for the resistance to stabilize after turning the wind tunnel off .	66
11	Physical properties of Kapton films (data obtained from Dupont) . .	76
12	Properties of Elastosil <sup>®</sup> LR3162 (measured on sheets that are vulcanized for 5 min at 165 <sup>0</sup> C)[8] . . . . .	77
13	Young’s Modulus of the composite elastomer extracted from different samples. $\epsilon$ is the strain and $E$ is the Young’s modulus. $L$ , $W$ , $t$ are the unstrained length, width and thickness of the sample respectively . .	79
14	Gage factors calculated at different strains using the same sample . .	83
15	CO <sub>2</sub> laser parameters used for through ablation of Kapton <sup>®</sup> . . . . .	88
16	Oxygen plasma treatment parameters used in the RIE . . . . .	92
17	Excimer laser parameters used for cutting the microstencil . . . . .	94
18	Processing conditions for NR9-8000 patterning . . . . .	98
19	NR9-8000 descum recipe used after development . . . . .	98

20	NR9-8000 descum recipe used after copper plating and stripping of the resist . . . . .	99
21	Conditions used for PECVD deposition of silicon dioxide . . . . .	101
22	Conditions used for PECVD deposition of silicon nitride . . . . .	101
23	Device and piezoresistor dimensions for the devices fabricated. L and W are the length and width respectively. T is the thickness of the Kapton <sup>®</sup> used for the tuft fabrication. Subscript t is for the tuft and subscript p is for the piezoresistor . . . . .	105
24	Rigidity analysis for 1.5mm x 0.4 mm microtufts for different thicknesses of Kapton <sup>®</sup> . L and W are the length and width respectively .	107
25	Resistance variations with experiments. $R_i$ , $R_f$ are the device resistances before and after the wind tunnel experiment. Hysteresis is defined as $R_i - R_f$ . The % hysteresis is calculated with respect to the initial resistance . . . . .	107
26	Sensitivity analysis for Type I and II experiments . . . . .	116
27	Resistance variations with experiments, for 1.5mm x 0.4mm microtufts. $R_i$ , $R_f$ are the device resistances before and after the wind tunnel experiment. Hysteresis is defined as $R_i - R_f$ . The % hysteresis is calculated with respect to the initial resistance . . . . .	116

## LIST OF FIGURES

1	Technology based on Biomimetics [7] . . . . .	3
2	Biomimetic MEMS sensors . . . . .	5
3	Biomimetics and flow sensing . . . . .	6
4	The working concept of a standard strain gage [11] . . . . .	9
5	Change in resistance with strain for various strain gage element materials	10
6	The piezoresistive properties of silicon (Pfann and Thurston [82]) . .	12
7	Piezoresistive behavior in filled polymers . . . . .	15
8	A 3-D out of plane flow sensor based on thermal anemometry (Chen et.al. [19]) . . . . .	18
9	Flow sensors based on momentum transfer principles . . . . .	20
10	Artificial sensory hairs for flow sensing using polymer MEMS . . . . .	21
11	SU-8 three-axis sensors with piezoresistive strain gauges (Klejwa et.al. [56]) . . . . .	22
12	Modeling of a cantilever beam . . . . .	25
13	Velocity profile seen by the sensor (Fan et.al. [35]) . . . . .	26
14	“Soft” micromachining techniques (Xia et.al. [107]) . . . . .	29
15	Fabrication process sequence for PDMS to PDMS MTM . . . . .	32
16	SEM pictures of the three layer SU8 master structures . . . . .	33
17	Patterning of Au on PDMS mold using microtransfer printing . . . . .	34
18	Final device photomicrographs. Figure 18(a) and Figures 18(b), 18(c) belong to different fabrication iterations. Figure 18(c) is the close-up of Figure 18(b) . . . . .	35
19	Interconnections of the final device to the external circuit . . . . .	36
20	Deflection of the sensing pillar using a probe tip . . . . .	39
21	Change in device response with # of experiments for cyclic 8.75 $\mu\text{m}$ deflections . . . . .	40
22	Technical issues with MTM . . . . .	41
23	Damage to the metal film on the PDMS mold after microtransfer printing	42

24	Problems observed with microneedle structures fabricated by conventional MTM . . . . .	44
25	Fabrication process sequence for the dissolving mold MTM process . .	45
26	Comparison of PMMA and PDMS molds after microtransfer printing	48
27	PMMA molds after microtransfer printing . . . . .	49
28	Final PDMS 186 devices for the two designs after dissolving the PMMA mold. Figures 28(a) and 28(a) are of the updated geometry; Figures 28(c) and 28(d) are for the old geometry . . . . .	50
29	Selection of water soluble sacrificial polymers (Linder et.al. [67]) . . .	52
30	Comparison of the quality of PAA molds made using two different techniques . . . . .	53
31	The centrifugation process for making the PAA mold (Adapted from Lee et.al. [62]) . . . . .	53
32	A typical spray coating setup (Pham et.al. [83]) . . . . .	54
33	Spray coating of PDMS on PAA molds. Figures (a) and (b) are for 3 spray coating cycles, while Figure (c) is for 5 . . . . .	56
34	PAA molds with spray coated PDMS after microtransfer printing . .	56
35	Final PDMS (Figures 35(a),35(b)) and PU (Figures 35(c),35(d),35(e)) devices after dissolving the PAA mold. The figures show good metal film quality and no structural damage . . . . .	58
36	Interconnection scheme used to connect the chip to the PCB . . . . .	59
37	Static deflection tests with devices made using the dissolving mold process with PMMA molds . . . . .	60
38	Screen shot of the HP-VEE data acquisition software used . . . . .	60
39	Wind tunnel experiment setup . . . . .	61
40	Direction of load for static as well wind tunnel tests . . . . .	61
41	Wind Tunnel testing of devices fabricated by the dissolving mold process. Both experiments are conducted on the <i>same</i> sample . . . . .	62
42	Wind Tunnel testing - experiment # 3 . . . . .	63
43	Circuit diagram of the device sensing element . . . . .	67
44	Warpage observed in thin metal films (Au) on elastomeric substrate .	69
45	Bond pads of devices fabricated by the dissolving mold process. The pad on the left has been probed, while the pad on the right is untouched	70



46	Sensing principle for the microtuft based flow sensor . . . . .	75
47	Stress-strain curve for a 5mm wide composite elastomer sample. The thickness of the material is about 97 $\mu\text{m}$ and the unstrained length is 21 mm. The applied strain is 10% . . . . .	78
48	The <i>poor man's Instron</i> - experimental setup for gage factor characterization . . . . .	80
49	Resistance vs Time graph for strain loading and unloading with 10% maximum strain in a 23mm length composite elastomer sample. Both loading profiles are one and the same, but represented in different ways to demonstrate the drift of resistance with time and the hysteresis respectively . . . . .	81
50	Loading profile for a maximum strain of 10% . . . . .	83
51	Resistance vs Time graph for strain loading and unloading. the sample is untested and unstrained when it is subjected to 1% strain. The 10% strain experiment is performed immediately after that Figure (a) shows that the sample resistance is not stablized even after a long time, both before and after loading. But during the second strain cycle, the resistance stabilization is almost immediate . . . . .	87
52	Fabrication process flow for 1x3 arrays of test devices . . . . .	89
53	Fabrication process for a 5x5 array with backside interconnections . .	90
54	The LS500XL series CO <sub>2</sub> laser . . . . .	91
55	Lamination of Kapton® . . . . .	92
56	Excimer laser for micromachining of Kapton® . . . . .	93
57	SLA alignment jigs for stencil printing of the conductive elastomer . .	95
58	Microstenciling of Elastosil® LR3162 . . . . .	95
59	Piezoresistor designs after curing of the conductive elastomer . . . . .	96
60	Interconnection of the piezoresistors to an external PCB using silver epoxy . . . . .	97
61	Plating of Copper electrodes on the Kapton® substrate. Figure (c) shows the delamination of the copper because of the poor adhesion with Kapton® . . . . .	100
62	Stress induced curvature of Kapton® 65E (16.51 $\mu\text{m}$ ) microtuft . . . .	101
63	Dependence of curvature of microtuft on thickness of Kapton® . The oxide thickness and the geometry are the same . . . . .	102

64	Dependence of curvature on thickness of oxide film deposited. The material of the microtufts are Kapton <sup>®</sup> 50 FPC (12.7 $\mu\text{m}$ thick). The curvature is not as pronounced because of the increased stiffness due to the presence of the piezoresistors. 20 mins of deposition corresponds to an oxide thickness of 1 $\mu\text{m}$ . . . . .	103
65	Bending of the microtuft into the plane of the paper. The material of the microtuft is Kapton <sup>®</sup> 50HN (12.7 $\mu\text{m}$ thick) . . . . .	103
66	Alignment control in the Excimer laser . . . . .	104
67	Scaling of the microtuft dimensions. Figures (a) and (b) are macroscale tufts that are fabricated using the CO <sub>2</sub> laser alone. Figures (c) and (d) are for scaled down tufts. Devices (a) and (b) have no stress inducing films. Device (c) has 5000A of silicon nitride and device (d) has 1 micron of silicon dioxide deposited on the backside. The testing results shown in Section 6.4 are for the devices shown in Figures (c) and (d) . . . . .	106
68	Backside interconnects on a large area array . . . . .	108
69	(a) Experimental setup for the wind tunnel experiments of the microtuft based flow sensors (b) Kapton <sup>®</sup> 65E (16.5 $\mu\text{m}$ tuft ) . . . . .	109
70	3.5mm x 2.2 mm tufts with silicon nitride-device response . . . . .	110
71	Final device pictures of the 1.5 x 0.4 mm test devices showing the pronounced curvature. The devices are fabricated using Kapton <sup>®</sup> 30HN (7.6 $\mu\text{m}$ ) . . . . .	111
72	Experiment # 1 - 1.5mm x 0.4 mm microtufts-device response to Type I experiment . . . . .	112
73	Experiment # 2-1.5mm x 0.4 mm microtufts-device response to Type II experiment. (the same device as in experiment # 1 is used) . . . . .	113
74	Experiment # 3-1.5mm x 0.4 mm microtufts-device response to Type II experiment. (the same device as in experiment # 1 is used) . . . . .	114
75	Experiment # 4-1.5mm x 0.4 mm microtufts-device response to Type I experiment. (the same device as in experiment # 1 is used) . . . . .	115
76	Heat treatment experiments of Kapton <sup>®</sup> with oxide. Both experiments were performed on the same sample with a thickness of 7.6 $\mu\text{m}$ . The test in Figure (b) was conducted after the one in Figure (a)) . . . . .	119
77	Decomposition of stress into its components for 40 $\mu\text{m}$ oxide films. Intrinsic stress is obtained by subtracting the thermal stress from the measured stress. (Chen et.al. [22]) . . . . .	123
78	Film stress in silicon dioxide as a function of storage time (Haque et.al. [41]) . . . . .	125

79	Tensile creep properties of Kapton <sup>®</sup> Type HN films (obtained from Dupont) . . . . .	126
80	Investigation of residual stresses in a 3.5mm x 2.2 mm Kapton <sup>®</sup> 65E (16.5 $\mu\text{m}$ thick) with 1 $\mu\text{m}$ thick oxide layer. Figure 80(a)(i) is the original curvature of the structure before any thermal treatment. Figure 80(a)(ii) is the final curvature at the end of the first thermal treatment	127

## SUMMARY

Microelectromechanical systems (MEMS) based artificial sensory hairs for flow sensing have been widely explored, but the processes involved in their fabrication are lithography intensive, making the process quite expensive and cumbersome. Most of these devices are also based on silicon MEMS, which makes the fabrication of out-of-plane 3D flow sensors very challenging. This thesis aims to develop new fabrication technologies based on Polymer MEMS, with minimum dependence on lithography for the fabrication of piezoresistive 3D out-of-plane artificial sensory hairs for sensing of air flow. Moreover, the fabrication of a flexible sensor array is proposed and new materials are also explored for the sensing application.

Soft lithography based approaches are first investigated for the fabrication of an all elastomer device that is tested in a bench top wind tunnel. Micromolding technologies allow for the mass fabrication of microstructures using a single, reusable mold master that is fabricated by SU-8 photolithography, reducing the need for repetitive processing. Polydimethylsiloxane (PDMS) is used as the device material and sputter deposited gold is used as both the piezoresistive as well as the electrode material for collection of device response. The fabrication results of PDMS to PDMS metal transfer micromolding (MTM) are shown and the limitations of the process are also discussed. A dissolving mold metal transfer micromolding process is then proposed and developed, which overcomes the limitations of the conventional MTM process pertinent to the present application. Testing results of devices fabricated using the dissolving mold process are discussed with emphasis on the role of micro-cracking as one failure mode in elastomeric devices with thin film metal electrodes.

Finally, a laser microfabrication based approach using thin film Kapton® as the

device material and an electrically conductive carbon-black elastomer composite as the piezoresistor is proposed and demonstrated. Laminated sheets of thick and thin Kapton<sup>®</sup> form the flexible substrate on which the conductive elastomer piezoresistors are stencil printed. Excimer laser ablation is used to make the micro-stencil as well as to release the Kapton<sup>®</sup> cantilevers. The fluid-structure interaction is improved by the deposition of a thin film of silicon dioxide, which produces a stress-gradient induced curvature, strongly enhancing the device sensitivity. This new approach also enables the fabrication of backside interconnects, thereby addressing the commonly observed problem of flow intrusion while using conventional interconnection technologies like wire-bonding. Devices with varying dimensions of the sensing element are fabricated and the results presented, with smallest devices having a width of 400  $\mu\text{m}$  and a length of 1.5 mm with flow sensitivities as high as 60  $\Omega\text{s/m/s}$ . Recommendations are also proposed for further optimization of the device.

# CHAPTER I

## INTRODUCTION

Unmanned aerial vehicles (UAVs) have emerged as important machines for a number of military roles including reconnaissance and attack and also for a number of civil applications such as police observations, firefighting etc. [12]. Rapid, dynamic maneuvering of the UAVs is often required, involving very high flight speeds and extreme maneuvers for military warfare and other applications. Thus, flight control has assumed paramount importance in aerodynamic systems. The Wright brothers, through their patented *three axis control*, were the first to exploit flight control to conquer the “flying problem”, rather than focusing on more powerful engines to master flight [105].

To achieve dynamic maneuvering of UAVs, rapid and distributed sensing of the flow conditions near the lifting surface is very important. Flow sensors are required for such an application and have been widely used. Such flow sensing would have to be performed across a large area of the wing span of the UAV to map flow distributions accurately and often requiring information about the velocity distributions in the boundary layer of the flow. Thus, a flow sensor chosen for such an application would have to satisfy the following criteria:

1. High spatial resolution-the sizes must be such that the sensors can be densely packed allowing for determination of flow patterns, rather than the flow at a single point [104]
2. Fast time response
3. Integrated signal processing [35]

Existing flow sensors based on pressure distribution measurements have large sizes and are generally not suited for forming distributed arrays [35].

Microelectromechanical systems (MEMS) sensors and actuators have been extensively integrated into aerodynamic systems to extract flow information and to provide extreme flight maneuvers respectively. The actuators are guided by the sensors and controlled by the outputs of the feedback control system, thereby providing an efficient flight control mechanism for UAVs. A MEMS based flow sensor would be an ideal candidate for applications requiring high sensitivity and fast response, combined with a low-cost scheme that enables large area fabrication on flexible substrates.

A comprehensive review of existing flow sensors is presented in Section 2. Many flow sensors found in the literature are biomimetic in nature. In other words, the designs and sensing mechanisms of these flow sensors have drawn inspiration from biological species that have highly developed sensory organs that can detect not only flow and pressure waves, but a host of other stimuli. Since these organisms have evolved through the ages, their sensory organs are highly evolved and optimized and thus an ideal model to copy from. The following sections discuss biomimetics and its impact on MEMS based sensors.

## **1.1 Biomimetics**

“**Biomimicry** (from *bios*, meaning life, and *mimesis*, meaning to imitate) is the science that studies nature, its models, systems, processes and elements and then imitates or takes creative inspiration from them to solve human problems sustainably [6].” The principle of ‘survival of the fittest’ forces organisms (both flora as well as fauna) to constantly evolve and assume a highly optimized and efficient architecture. Thus, its only logical that we design and develop engineering systems that “mimic” nature. This area of research is known as **biomimetics**.

**Velcro**, invented by George Mestral, was inspired by the “burr” which clung on

tightly to his dog’s fur, and is perhaps the best example of the use of biomimetics (Figure 1(a)). Other examples include **morphing aircraft wings** inspired from different bird species with different flying patterns, **Lotus-effect** surfaces that are superhydrophobic and have self-cleaning properties (Figure 1(b)) and of course, Leonardo Da Vinci’s flying machines (Figure 1(c)) [7].

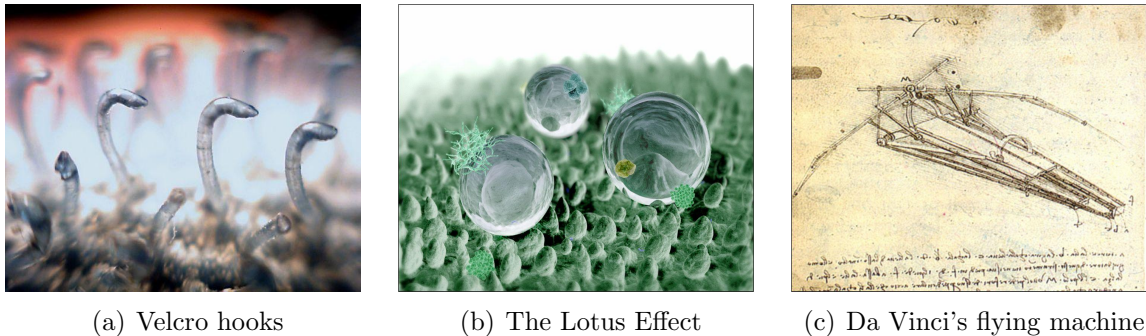


**Figure 1:** Technology based on Biomimetics [7]

## 1.2 *Biomimetics, MEMS and flow sensors*

The rigors of evolution have ensured that nature develops a stunning diversity of sensory systems. Humans and animals rely on the senses of smell, taste, touch and vision to interact with the external world. Organisms other than human beings, in particular, have developed sharp acoustic, olfactory and tactile senses for object detection and spatial orientation [14]. Some of the common kinds of “natural sensors” found include infrared organs in buprestid beetles for detection of forest fires, the use of echolocation by many nocturnal fish for objection detection [14] and mechanoreceptive sensory hairs in crickets for low frequency sound detection [27].

Microelectromechanical systems (MEMS) is the technology of the very small involving the fabrication of “micromachines” that perform a variety of sensing and actuation jobs ranging from power generation [4] to sensing of chemicals and gases [61]. The demand for MEMS devices in the commercial market is increasing, thus creating a need for building high efficiency devices at low cost. Researchers are therefore



turning their attention to building bio-inspired devices with improved performance and efficiency, combining with it a low cost fabrication process. Thus a variety of bioinspired MEMS sensors have been fabricated and some of the examples are listed below. This only represents a small fraction of the bio-inspired sensors and actuators being fabricated.

- Multimodal tactile sensors shown in Figure 2(a) [30], which mimic mechanoreceptors in the human skin
- Directional MEMS microphone inspired by the ears of the parasitoid fly, *Ormia Ochracea*, shown in Figure 2(b) [24]
- Taste and smell sensor shown in Figure 2(c) [98]
- *Ionic polymer-metal composites*(IPMCs) as biometric sensor actuators and artificial muscles [92]
- Qualcomm’s MEMS based display - IMOD(Interferometric Modulator Display), shown in Figure 2(d), mimic the bright colors that are seen in butterfly wings [10, 9]

Flow control and sensing also has been the subject of intense investigation for a long period of time. In fact, the airplane also began as a biomimetics experiment. The Wright brothers used wing warping to assist in stability and control of the *Wright flyer* after Wilbur watched pigeons rotate their wings independently through positive and negative angles of attack. Fishes use lateral line sensors to monitor surrounding flow fields for movement and position control. A lateral line system consists of an array of sensor nodes, known as *neuromasts*, that in turn contain clusters of hair cells that function as flow sensors, as shown in Figure 3(a). Fan et.al. have exploited these lateral line sensors to fabricate flow sensors [35]. Biological hair cells are typically used for hearing and maintaining body equilibrium in humans. This has been implemented

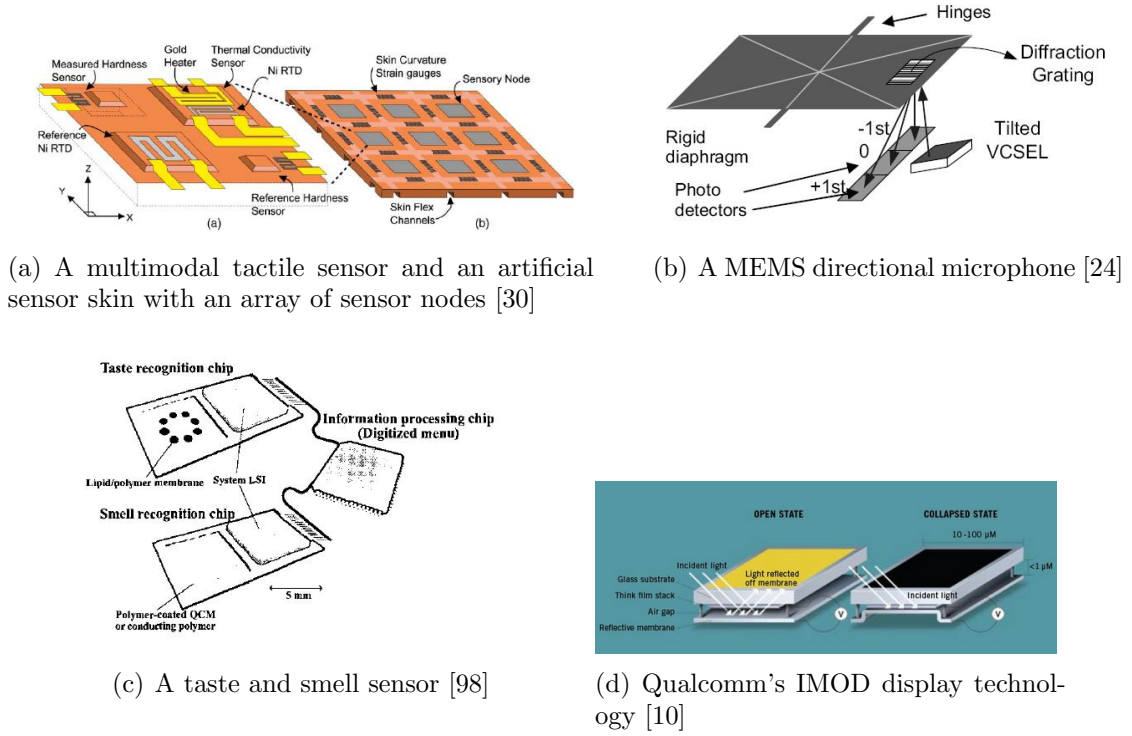


**Figure 2:** Biomimetic MEMS sensors

as an *artificial hair cell (AHC)* by Li et.al., using MEMS technology, to fabricate flow sensors [65]. In order to escape from danger, an insect has the ability to detect low velocity of airflow by using wind receptor hairs at the base of its tail [93]. Shimozawa et.al. have investigated the structural scaling and functional design of the cercal wind receptor hairs of insects [94]. The mechanoreceptors that are responsible for flow sensing in these insects have also been investigated [38]. Dijkstra et.al. have exploited such similar flow sensitive receptor hairs in crickets, shown in Figure 3(b) to fabricate a capacitive flow sensor [27]. The sensory hairs of the cricket are situated on the back on the cricket's body on appendices called *cerci*. Airflow around the receptor hairs causes a neuron to be fired by rotation of the hair base. By combining the inputs from many such hairs, the cricket is able to pinpoint low-frequency sound from any direction [60]. MEMS based biomimetic micro-UAVs are also being developed which are modeled on the flight patterns of insects [42] (Figure 3(c))

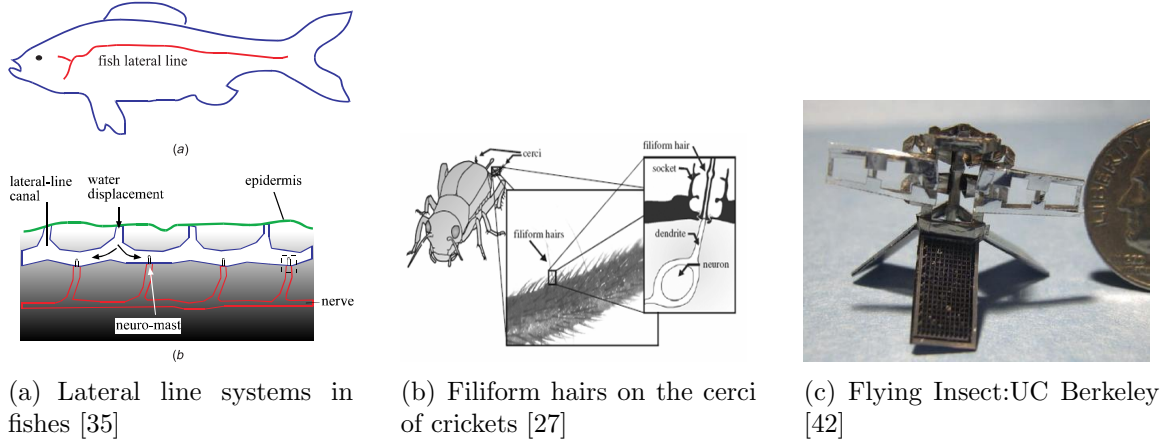


**Figure 3:** Biomimetics and flow sensing

The sensors that are fabricated in this research are based on the sensory hairs of crickets as they are excellent models for development of MEMS flow sensors, representing a well packaged and ultra-sensitive flow sensor. Moreover, the length scales of cricket hairs match well with boundary layer thicknesses at nominal flow velocities, thus a good measure of the dimensional requirements of the sensors to be fabricated. These sensory hairs are mimicked in the form of artificial *microtufts* that respond to wind velocity and are ultimately to be used for flow control applications.

### 1.3 Outline

This thesis consists of a total of seven chapters, including this introduction chapter. Chapter 2 focuses on the two key words in the thesis title-“materials and processes”. The first half of the chapter introduces piezoresistive materials and piezoresistivity. Some of the conventional and non-conventional piezoresistive materials are discussed here. The latter half of the chapter introduces MEMS flow sensors fabricated by other researchers. These include silicon MEMS flow as well as polymer MEMS flow sensors. Chapter 3 discusses the objectives and approaches of the research. The design principles and transduction scheme used are discussed in detail in this chapter. Chapter 4, 5 and 6 are dedicated to the fabrication technologies that have been exclusively developed for the microfabrication of flow sensors. Chapter 4 discusses

metal transfer micromolding (MTM) and the modifications used to fabricate an all elastomer piezoresistive flow sensor and some of the technical issues and difficulties associated with it. Chapter 5 introduces a novel dissolving mold MTM process, which overcomes some of the technical challenges of the modified MTM process. Chapter 5 concludes with a detailed discussion on the failure modes of devices fabricated by both MTM and the dissolving mold process. In Chapter 6, a third and final fabrication technique is proposed that uses a new scheme based on a microcantilever architecture that proves to be much more robust and sensitive to air flow. This section also introduces a composite elastomer based piezoresistive material, whose mechanical and electrical properties are characterized. The thesis is concluded in Chapter 7 with an overall summary and contribution of the research conducted. It also talks about some of the existing technical challenges and a brief discussion of the future work.

## CHAPTER II

### PIEZORESISTIVE MATERIALS IN MEMS AND REVIEW OF MEMS FLOW SENSORS

#### *2.1 Piezoresistive thin films and materials*

The discovery of piezoresistance in silicon and germanium at Bell Laboratories in 1954 [95] is considered one of the milestones that fueled the growth of the MEMS industry [15]. Piezoresistance is a change in resistivity of the material under the influence of an externally applied stress or strain. The resistivity of a material depends on the internal atomic positions and their motions. Strain changes these arrangements and hence, the resistivity [91]. The electrical resistance of any material of length  $L$  and cross-sectional area  $A$  with a resistivity of  $\rho$ , is given by Equation 1.

$$R = \rho \frac{L}{A} \quad (1)$$

If the conductive material is deformed elastically in tension (or compression), its change in resistance can be expressed by Equation 2.

$$\frac{dR}{R} = \frac{d\rho}{\rho} - \frac{dA}{A} + \frac{dL}{L} \quad (2)$$

Assuming an isotropic Poisson's ratio of  $\sigma$ , the fractional change in the area can be expressed as shown in Equation 3.

$$\frac{dA}{A} = -2\sigma \frac{dL}{L} \quad (3)$$

Consequently, the change in resistance can be finally expressed as shown in Equation 4.

$$\frac{\frac{dR}{R}}{\frac{dL}{L}} = (1 + 2\sigma) + \frac{\frac{d\rho}{\rho}}{\frac{dL}{L}} = \gamma \quad (4)$$

Where  $\gamma$  is the dimensionless number describing the variation of the electrical resistance with applied strain and is known as the *gage factor*. In equation 4,  $(1+2\sigma)$  is purely a geometric effect due to change in dimensions of the piezoresistor. The term  $(d\rho/\rho)/(dL/L)$  is a physical effect that depends on the nature of the material involved. It is this term that differentiates between the gage factors of the various thin film piezoresistors [79].

Piezoresistors can be broadly classified as (i) metal thin film piezoresistors (ii) doped silicon piezoresistors and (iii) conductive composite piezoresistors. Typical applications for thin film strain gages are in piezoresistive cantilevers used in force and bio-sensing and in pressure sensors. Figure 4 shows the working concept of a strain gage [11].

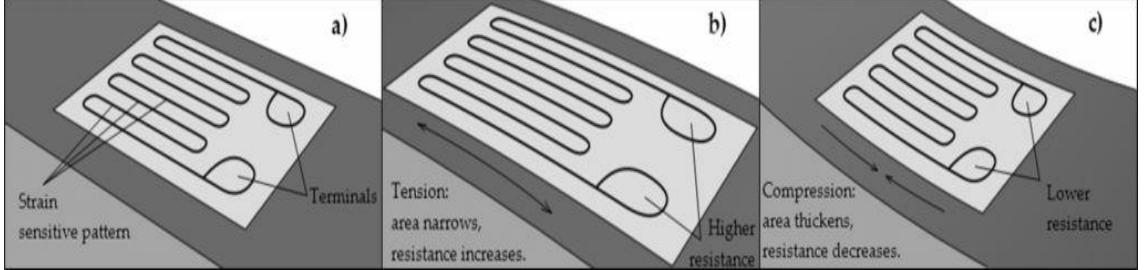


**Figure 4:** The working concept of a standard strain gage [11]

### 2.1.1 Metal thin film piezoresistors

The origin of piezoresistivity in metals lies in the changing of the internal atomic positions by the application of stress, as explained before. Stress causes the energy bands in the metals to distort slightly, resulting in small changes in the amount of conduction and this leads to the manifestation of piezoresistance [91]. Metal thin film strain gages are typically bonded onto components in which it is desired to measure

the strain. Figure 5 shows the change in resistance as a function of applied strain for various strain gage elements.

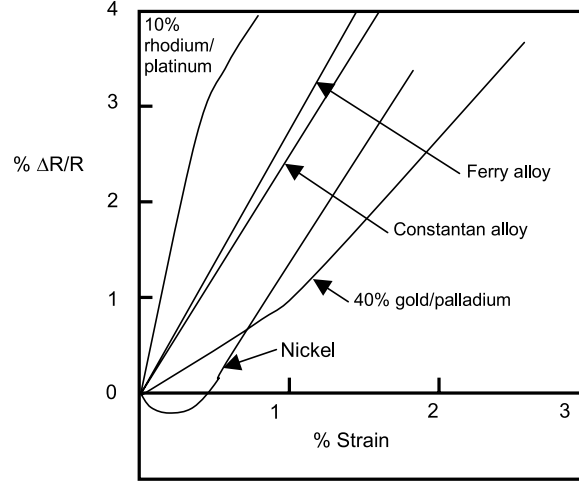


**Figure 5:** Change in resistance with strain for various strain gage element materials

From equation 4, it is clear that the differences in gage factors of various materials is essentially controlled by the fractional change in resistivity, as mentioned before. The piezoresistive gage factor of thin metals films deposited by evaporation or sputtering have additional contributions to the resistivity terms, because of their structure (especially grain size and separation between the grains) [79].

Metal thin film resistors are very popular in the fabrication of MEMS devices where the transduction mechanism is piezoresistivity. Lei et.al have reported the fabrication of thin film strain gages (TSFGs) using palladium-13% rhodium as the piezoresistive material, to meet the needs of aeronautics and aerospace research, where stress gradients encountered are high [63]. Gold piezoresistors are also commonly used for the fabrication of MEMS devices. Klejwa et.al. report the use of gold piezoresistors in the fabrication of an SU-8 three axis sensor for measuring the tactile sensitivity and forces exerted during locomotion of small biological organisms [56]. Rajanna et.al. have investigated Au-Ti (89:11) thin film strain gages for applications in pressure sensors [85]. Engel et.al. have developed an artificial skin that consists of a contact force and hardness testing sensor that is based on a piezoresistive transduction mechanism.

They fabricate their strain gages using thin film nickel-chromium (Ni-Cr:80-20%) [30]. But typical metal thin film resistors have gage factors between 2-3, yielding a very low sensitivity. Thus, some researchers have investigated semiconducting films of indium tin oxide (ITO), which are reactively sputtered. Such films have exhibited gage factors as high as -77.71 at room temperature, after annealing [29]. Gregory et.al. have also demonstrated a high gage factor of 15 in reactively sputtered aluminum nitride, for use in high temperature strain gage applications [40].

From a brief literature survey, it is observed that metal thin films are not the preferred piezoresistors for sensor applications, primarily because of its low gage factor compared to doped silicon piezoresistors. But, metal thin film piezoresistors are desirable in devices fabricated using polymer MEMS technology, where low processing temperatures are required.

### **2.1.2 Doped silicon piezoresistors**

Charles Smith, a researcher at Bell Labs, first reported that uniaxial tension causes a change in resistivity in silicon and germanium of both n and p type [95]. The source of piezoresistivity in silicon is same as that in metal thin films. When a stress is applied to a semiconductor, the band energies move by small amounts. But, unlike metals, these small shifts can have enormous effects on the conductivity properties in semiconductors. This, in turn, gives rise to the large piezoresistive gage factors of doped silicon piezoresistors. These have other distinct advantages over metal thin film piezoresistors. There is no need to consider adhesion issues between the material and the device itself, since these are diffused into the silicon wafer. Hence, the piezoresistors and the device are both part of the same wafer [91]. Pfann and Thurston were the first to demonstrate semiconducting stress transducers using the transverse and shear piezoresistance effects [82]. Figure 6(a) shows the piezoresistive coefficients of silicon and germanium at room temperature reported in their work.



Material	Resistivity (ohm cm)	$\pi_{11}$	$\pi_{12}$	$\pi_{44}$
		(10 <sup>-12</sup> cm <sup>2</sup> /dyne)		
<i>n</i> -Ge	~1	...	...	-138
<i>p</i> -Ge	~1	...	...	+97
<i>n</i> -Si	~12	-102	+53	...
<i>p</i> -Si	~8	...	...	+138

(a) Room temperature piezoresistance coefficients of silicon and germanium.

Longi- tudinal direction, 1	Longitudinal coefficient, $\pi_{11}'$	Trans- verse direction, 2	Transverse coefficient, $\pi_{12}'$
001	$\pi_{11}$	010	$\pi_{12}$
001	$\pi_{11}$	110	$\pi_{12}$
111	$\frac{1}{3}(\pi_{11} + 2\pi_{12} + 2\pi_{44})$	$\bar{1}\bar{1}0$	$\frac{1}{3}(\pi_{11} + 2\pi_{12} - \pi_{44})$
111	$\frac{1}{3}(\pi_{11} + 2\pi_{12} + 2\pi_{44})$	11 $\bar{2}$	$\frac{1}{3}(\pi_{11} + 2\pi_{12} - \pi_{44})$
$\bar{1}\bar{1}0$	$\frac{1}{2}(\pi_{11} + \pi_{12} + \pi_{44})$	111	$\frac{1}{3}(\pi_{11} + 2\pi_{12} - \pi_{44})$
$\bar{1}\bar{1}0$	$\frac{1}{2}(\pi_{11} + \pi_{12} + \pi_{44})$	001	$\pi_{12}$
$\bar{1}\bar{1}0$	$\frac{1}{2}(\pi_{11} + \pi_{12} + \pi_{44})$	110	$\frac{1}{2}(\pi_{11} + \pi_{12} - \pi_{44})$
$\bar{1}\bar{1}0$	$\frac{1}{2}(\pi_{11} + \pi_{12} + \pi_{44})$	11 $\bar{2}$	$\frac{1}{6}(\pi_{11} + 5\pi_{12} - \pi_{44})$
11 $\bar{2}$	$\frac{1}{2}(\pi_{11} + \pi_{12} + \pi_{44})$	$\bar{1}\bar{1}0$	$\frac{1}{6}(\pi_{11} + 5\pi_{12} - \pi_{44})$
$\bar{1}\bar{1}0$	$\frac{1}{2}(\pi_{11} + \pi_{12} + \pi_{44})$	221	$\frac{1}{9}(4\pi_{11} + 5\pi_{12} - 4\pi_{44})$
22 $\bar{1}$	$\pi_{11} - 16(\pi_{11} - \pi_{12} - \pi_{44})/27$	$\bar{1}\bar{1}0$	$\frac{1}{9}(4\pi_{11} + 5\pi_{12} - 4\pi_{44})$

(b) Longitudinal and transverse piezoresistive coefficients for cubic crystals along various directions

**Figure 6:** The piezoresistive properties of silicon (Pfann and Thurston [82])

The change in resistance due to a longitudinal strain of  $\sigma_l$  and a transverse strain of  $\sigma_t$  is given by Equation 5 [91].

$$\frac{dR}{R} = \pi_l \sigma_l + \pi_t \sigma_t \quad (5)$$

**Table 1:** Transverse and longitudinal piezoresistance coefficients in doped silicon resistors oriented in the [110] direction

Doping type	$\pi_l$	$\pi_t$
n-type	-31.2	-17.6
p-type	71.8	-66.3

As can be seen from Figure 6(a) and Table 1, the extremely high gage factors of n-type and p-typed silicon piezoresistors as compared to metal thin film piezoresistors, makes them a popular choice for a variety of sensors. Moreover, for p-type piezoresistors, which have opposite signs of the coefficients, a full Wheatstone bridge can be used to almost double the output response of the device. However, because of the high temperature coefficient of resistance of doped silicon, compensation becomes a major issue in such piezoresistors. The Motorola manifold-absolute-pressure (MAP) sensor is a MEMS pressure sensor that uses such doped piezoresistors [91].

As will be seen in the review of silicon MEMS based flow sensors, a majority involve doped silicon piezoresistors [20, 21, 35, 77].

### **2.1.3 Conductive composite polymer piezoresistors**

Conductive composite polymers have been extensively reported because of their widespread applications. Plastics are usually considered insulating materials. However, if electrically conducting fillers such as metal powders or fibers, carbon black (CB), graphite fibers etc., are dispersed into the plastic matrix above a certain threshold value, it will become conducting [48]. The major applications for which these conductive polymers are used depend on the loading of the conductive material and the volume resistivity. Although metals have an inherently higher conductivity, they have a tendency to oxidize and form an insulating coating, which disrupts conductivity. Carbon black is thus a popular filler material to achieve conductivity. Carbon black is an amorphous form of carbon that is formed by the high temperature incomplete decomposition of aromatic hydrocarbons, through the rupture of the C-H bonds. Subsequently, the carbon atoms and the aromatic radicals react to form layer structures composed of hexagonal carbon rings, which tend to stack in layers forming crystallographic structures with high order, thus imparting conductivity to the material [48]. Carbon nanotubes are also being increasingly used as the filler material, on account of

its much higher conductivity.

Conductive polymers have been explored for a number of applications. Philip et.al. have developed composite thin films of polymethylmethacrylate (PMMA) with multi-walled carbon nanotubes (CNTs) for gas sensing applications [84]. Lewis et.al have also demonstrated a similar application with carbon-black filled organic polymers that swell with the absorption of different gases and thus undergoing a change of resistance [64]. Engel et.al. have used MWNT-polydimethylsiloxane (PDMS) composites to fabricate heaters integrated into microfluidic channels, and capacitive pressures sensors [34]. The other applications of such composite polymers include anti-static applications, electrostatic dissipation applications, and positive temperature coefficient materials (PTC) [48].

Filled polymers that are made conductive by the addition of carbon black particles, often exhibit a large piezoresistive behavior. The mechanism of the piezoresistivity in such systems is different from that in metal thin films and doped silicon. It has its origins in particle separations in the polymer matrix. This inter-particle separation, in turn, is controlled by the filler concentration. The transition from insulator to conductor for a polymer takes place abruptly at a threshold concentration of the filler particles known as the *percolation threshold*. Since the intrinsic mechanism behind the abrupt change in resistance lies in the separation of these filler particles, any process that can change the separations, can also change the resistivity of the material, leading to the phenomenon of piezoresistivity. The main reason for this piezoresistivity is thought to be because of the difference between the filler and matrix compressibilities [111]. Figure 7 demonstrates the piezoresistive behavior of filled polymers.

As can be seen from Figure 7(a), applying tension to the polymer increases the distance between the filler particles, which will change the inherent resistivity of the polymer. The conduction mechanism is also controlled to a certain extent by quantum mechanical tunneling between the filler particles in the matrix.

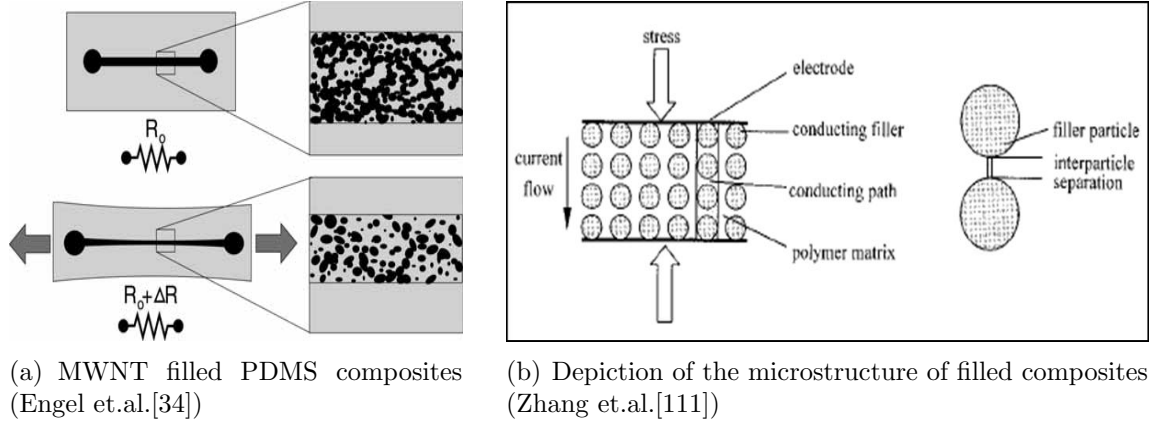


**Figure 7:** Piezoresistive behavior in filled polymers

A number of sensors have been fabricated that have exploited the piezoresistive properties of filled conductive polymer composites. Engel et.al. have demonstrated the fabrication of an all polymer two-axis artificial hair cell flow sensor, using a carbon black-polyurethane composite with a loading of 30 wt% [31]. They also report the fabrication of a similar sensor using MWNTs instead of CB, which reduces the required loading to 10 wt% in PDMS [32]. They report gage factors as high as 10 for the composite polymers they process. Frazier et.al. have reported the fabrication of a graphite-polyimide composite thin films that have gage factors as high as 16.8 at graphite loadings of 18 wt%, which could potentially be used in pressure sensors [36]. Lu et.al have also reported the fabrication of a piezoresistive conductive PDMS for microfingerprint sensors. They use a loading of 20 wt% carbon black and report a gage factor of 7.4 [70].

## 2.2 *Flow sensors*

The motivation behind the development of new fabrication techniques and the use of new materials (preferably polymeric) was partly discussed in Section 1. Many research groups have thus focused their attention on developing novel sensing and fabrication schemes that are aimed at simultaneously reducing fabrication costs and improving device sensitivity. The fabrication of large area arrays is also a challenge

that is being addressed. In this chapter, some of the flow sensors that have been fabricated by other researchers is briefly discussed.

Flow sensors fabricated for flow control essentially consist of shear stress sensors that are in fabricated *in the plane of the substrate* and 3D out of plane microstructures. Shear stress sensors are designed for detection of airflow separation on the leading edge of aircraft wings. They are typically fabricated as *flexible skins* that can be wrapped around the airfoil [47, 50, 52]. But, such shear stress sensors give no information about the mean free stream velocity and the velocity fluctuations that arise out of that [35]. Since the focus of this research is the fabrication of 3D out-of-plane flow sensors, this section reviews these types of sensors only.

A variety of flow sensors have been fabricated by research groups around the world using different transduction mechanisms. Some of the typical transduction schemes used are capacitive sensing, sensing based on Doppler frequency shift, thermal anemometry, piezoresistivity etc. Of these, bulk of the research has involved the fabrication of piezoresistive flow sensors, mainly because of the extremely high gage factors of doped silicon, as was explained in Section 2.1. Flow sensors reported over the years can be broadly classified into two categories based on the sensing principle: Sensors (i) based on heat transfer principles and (ii) based on momentum transfer principles [20]. Based on the material and the fabrication techniques used, these can also be classified as Silicon MEMS based flow sensors and the emerging area of Polymer MEMS based flow sensors.

### **2.2.1 Silicon MEMS flow sensors**

Single crystal silicon is a vastly popular material that is employed in a variety of commercial products, not only because of its well-established electronic properties, but also because of its excellent mechanical properties [81]. Since most of the established fabrication processes, both in the IC industry as well as in MEMS have been

developed with silicon, it is an automatic choice for the device material.

Bulk of the silicon MEMS based flow sensors fabricated use thermal anemometry to sense the flow. Hot wire anemometry (HWA) utilizes a thermal element (essentially a resistor) that functions as both a Joule heater, as well as a temperature sensor, though the two functions could be performed by different elements. Under no flow conditions, the thermal element assumes a steady state temperature, for a given current/voltage input. But in the presence of flow, it undergoes forced convective cooling. Depending on the temperature coefficient of resistance of the thermal element, its resistance will typically drop along with its temperature and this drop in resistance can provide information about the flow [20]. MEMS based thermal anemometers fabricated can be further classified as in-plane structures or out-of-plane structures.

Park et.al. have reported the fabrication of a silicon HWA capable of flow direction as well as velocity sensing, using platinum (Pt) as the material for the thermal element. The sensor consists of a central Pt heater and four detectors surrounding the heater, resting on top of a silicon diaphragm that is formed by backside etching. The direction and velocity of the flow can be computed from the output of each of the four detectors [78]. Ashauer et.al. have demonstrated the fabrication of a thermal flow sensor using thermopiles, consisting of polysilicon and gold, on a silicon nitride membrane. The device operates as a thermo-transfer sensor as well as a time of flight (TOF) detector [5]. Mailly et.al. have fabricated a anemometer with a low power consumption of 20 mW and a high sensitivity of 4.8 mV/(m/s) in the laminar flow regime. The heating element itself is made using a thin film of Pt evaporated onto a suspended membrane of silicon rich silicon nitride to thermally insulate the heater from the substrate [73]. Baar et.al. and Dijkstra et.al. have also reported on similar gas and liquid flow sensors respectively based on thermal anemometry [28, 100]. For dynamic low flow velocity detection of acoustic waves, Bree et.al. have demonstrated the fabrication of a device also based on thermal transfer principles, known as the

*microflow* [26]. Relatively little amount of work has been done in the area of 3-D out of plane thermal anemometers. Chen et.al. have used a novel *plastic deformation magnetic assembly (PDMA)* process to fabricate a 3-D thermal anemometer. Electroplated permalloy is used to bend the structure, which is initially fabricated in the 2-D plane, into the 3-D plane, by applying a magnetic field. The thermal resistor used is a nickel-chrome composite [19]. Figure 8 shows the 3-D out plane flow sensor based on thermal transfer principles.

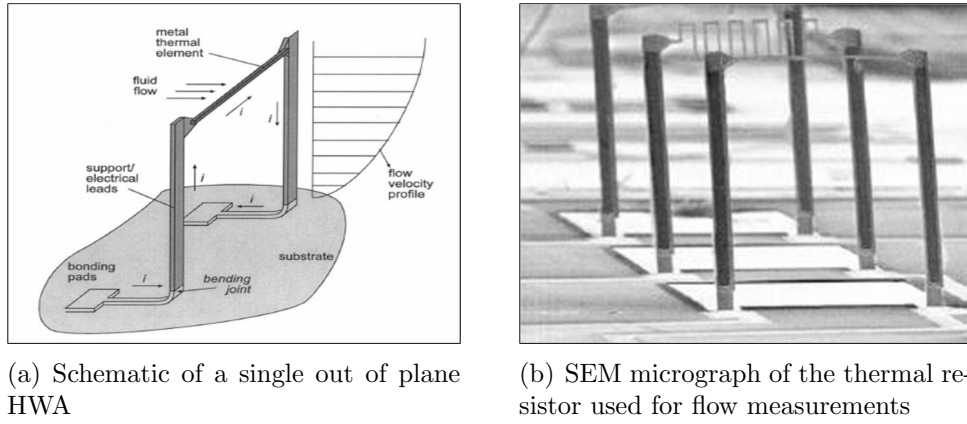


**Figure 8:** A 3-D out of plane flow sensor based on thermal anemometry (Chen et.al. [19])

Devices based on momentum transfer principles are also becoming increasingly popular. Such devices are not limited to a single transduction mechanism as in the case of HWA and employ variety of transduction schemes such as capacitive, piezoresistive etc. Chen et.al. have extended their novel PDMA process to the fabrication of a biomimetic, piezoresistive 3D flow sensor as well, mimicking the artificial lateral line in fishes. The piezoresistors are patterned using doped silicon and the vertical haircell itself consists of permalloy, which also allows for the 3D out of plane bending of the structure (Figure 9(a)). The fabricated sensor can sense flow velocities as low as 1 m/s [20]. Ozaki et.al. have reported the fabrication of an air flow sensor modeled on the wind receptor hairs of insects. They demonstrate both, 1-DOF and 2-DOF sensors using doped silicon piezoresistors. Backside silicon etching is used to create

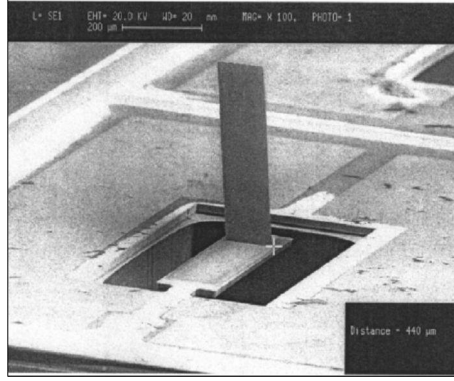
suspended silicon structures and cantilevers. In the case of the 2-DOF sensor, a long thin wire is manually glued to the center of the cross shaped section [77] (Figure 9(b)). Wiegerink et.al. have demonstrated the fabrication of a biomimetic flow-sensor array based on the filiform hairs of crickets. They use a surface micromachined suspended silicon nitride membrane and double layer SU-8 (a negative photoresist) processing to form 1 mm long artificial hairs, in a capacitive sensing scheme. The electrodes for the capacitor are formed by chromium and the underlying highly doped silicon substrate. The sensors use a drag-torque mechanism to displace the SU-8 hairs, which in turn cause rotation of the torsional membranes, creating a change in capacitance [104] (Figure 9(c)). Wang et.al. have reported a free-standing microcantilever based flow sensor that has a reported sensitivity of  $0.0284 \Omega\text{s/m/s}$ . They use platinum electrodes on a free standing silicon nitride microcantilever that curls up during the process due to a CTE mismatch with the silicon substrate [103] (Figure 9(d)). Finally, Yang et.al. have fabricated an *artificial hair cell (AHC)* based on silicon cantilevers with doped piezoresistors. They create the suspended cantilever with the doped piezoresistors using DRIE of an silicon-on-insulator (SOI) wafer. They create the out of plane structure, by spinning and defining an SU-8 post at the edge of the suspended cantilever [109] (Figure 9(e)).

### 2.2.2 Polymer MEMS flow sensors

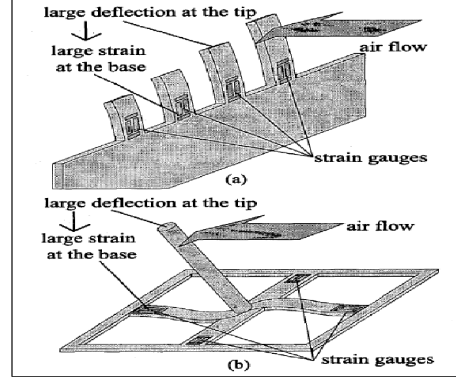
Polymer MEMS flow sensors are gaining importance because of the ease of fabrication of complex three dimensional geometries and relatively low costs to achieve the same. But its potential is only just being realized and thus polymer MEMS flow sensors are not as widely researched as silicon sensors.

A number of polymeric materials have been investigated for use as the device material. Engel et.al. have reported the use of polyurethane rubber (PU) for the fabrication of an all polymer two-axis artificial hair cell flow sensor. They have

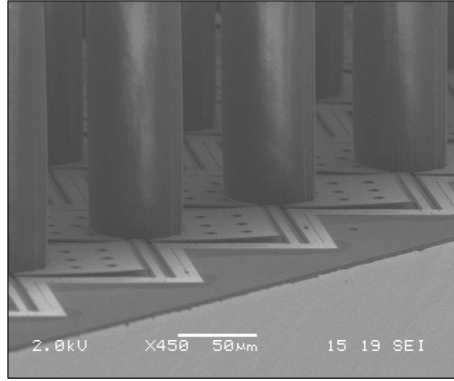




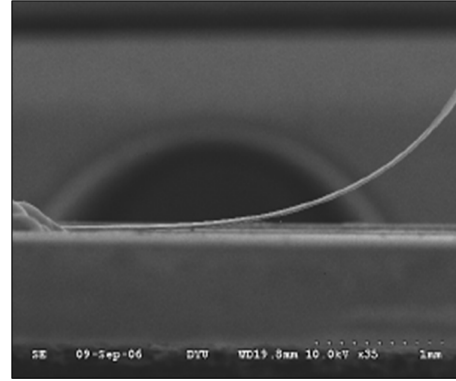
(a) SEM of a single artificial hair cell for flow sensing (Chen et.al. [20])



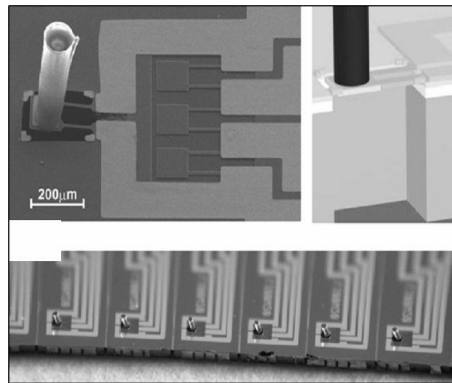
(b) Schematic of a 1-DOF and 2-DOF air flow sensor (Ozaki et.al. [77])



(c) Capacitive flow sensors with SU8 hairs on a suspended silicon nitride membrane (Wiegerink et.al. [104])



(d) SEM of a curved silicon nitride microcantilever based flow sensor (Wang et.al. [103])



(e) An artificial hair cell sensor (AHC) and sensor array (Yang et.al. [109])

**Figure 9:** Flow sensors based on momentum transfer principles

used PU in conjunction with conductive rubber force sensitive resistors (FSRs) to fabricate a piezoresistive flow sensor [31]. The FSRs are made by mixing carbon black particles into polydimethylsiloxane (PDMS). The artificial sensory hairs are made using PU. Figure 10(a) shows the fabricated device. The authors report an unamplified sensitivity of  $245 \text{ ppm}/\mu\text{m}$ . They extend the fabrication in a later report, by fabricating their flow sensors on a flexible Kapton<sup>®</sup> substrate [31, 32, 33], as shown in Figure 10(b).

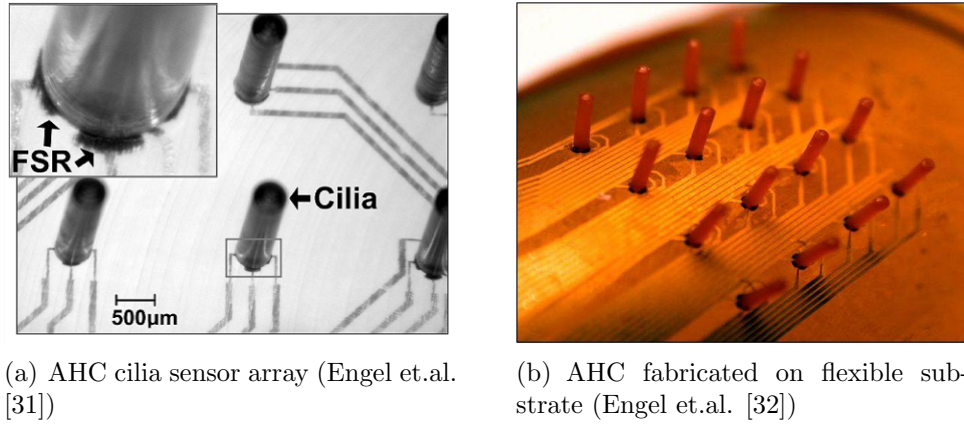


**Figure 10:** Artificial sensory hairs for flow sensing using polymer MEMS

Klejwa et.al. have reported a transparent three-axis micro strain gage force sensing pillar arrays for measuring tactile sensitivity in biological organisms. Each three-axis sensor in the array consists of four fixed-guided cantilever arms in a plus configuration, with a vertical pillar extending from the central suspended junction. Metal strain gauges are then patterned at the edge of the suspended arms using thin film gold piezoresistors. The devices fabricated have a  $1\mu\text{N}$  force sensitivity [56] (Figure 11). Although their application is biological in nature, their device satisfies all the requirements of a flow sensor and could be potentially used as one.

Schmitz et.al. have reported a novel *lost wax process* for the manufacture of high aspect ratio micro-hair sensor arrays. Their fabrication is based on the laser drilling of high aspect ratio holes in a wax foil, followed by the casting of an elastomeric

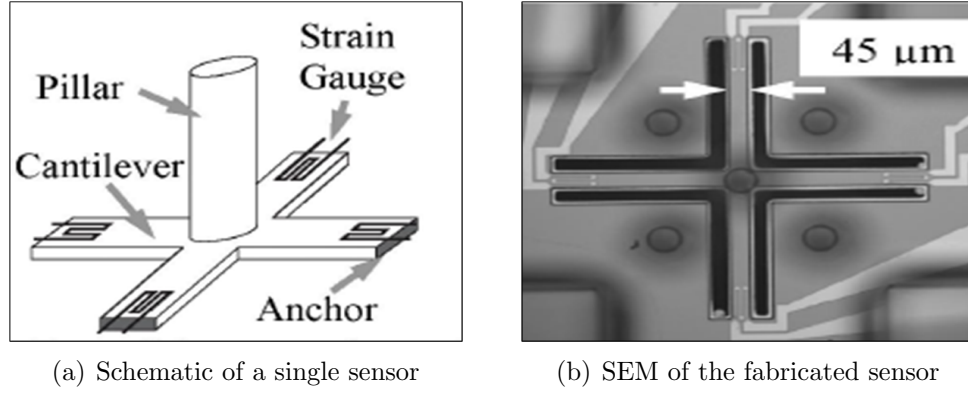


**Figure 11:** SU-8 three-axis sensors with piezoresistive strain gauges (Klejwa et.al. [56])

material into the mold. On dissolving the mold, the cured PDMS is released and high aspect ratio micro-hairs are obtained [90]. Although they do not report any application, it has potential applications in the fabrication of flow sensors. Finally, Thaysen et.al. have reported the fabrication of a polymer based mechanical sensor with an integrated gold thin film piezoresistor strain gage. The authors fabricate the sensor using SU-8 photolithography. They claim that because of the fact that polymer SU-8 is much softer than silicon, SU-8 based cantilevers are as sensitive to strain as silicon cantilevers, inspite of the low gage factor of gold [97]. Although not reported as a flow sensor, it could used as one, similar to the device fabricated by Yang et.al. [109].

## CHAPTER III

### OBJECTIVES AND APPROACHES

#### **3.1 Objectives**

MEMS based flow sensors technology so far has predominantly used silicon as the device material and piezoresistivity as the transduction mechanism. Because of the extremely high Young's modulus of silicon ( 160GPa), the high gage factor of doped silicon has been exploited to improve device sensitivity. Also, as mentioned before, fabrication of arbitrary geometries and 3-D out of plane structures using silicon micro-machining is very difficult. But the use of polymer MEMS and elastomeric materials in particular, allows for the fabrication of highly compliant structures which can greatly improve device response for 3-D out of plane flow sensors.

The primary objective of this research is to develop fabrication technologies that enable (i) low-cost (ii) mass reproducible (iii) high sensitivity 3-D out of plane piezoresistive flow sensors on flexible substrates, preferably with backside interconnects to avoid the disturbance of the flow profile being sensed. The fabrication techniques developed do not require the extensive use of photolithography, making the process cheap. The fabrication results of three different techniques followed by the results of testing will be shown in the following sections.

#### **3.2 Approaches**

To achieve the above objectives, the following approaches have been employed:

1. Use of soft lithography to enable mass fabrication of devices without repetitive fabrication of the master structure. The structure itself is defined by micro-molding, but to provide electrical functionality simultaneously with structural

definition, *metal transfer micromolding (MTM)* is used. This approach requires the use of photolithography just once and repetitive fabrication is done merely by using the negative polydimethylsiloxane (PDMS) molds.

2. A dissolving mold MTM process is developed and used. This technique overcomes some of the technical difficulties with conventional MTM (primarily microcracking) by eliminating the need for a final demolding of the casting polymer.
3. Both the above techniques contribute significantly to the field of metal transfer micromolding, but they have some inherent flaws that make them unsuitable for the current application. Thus laser fabrication is used to fabricate *microtufts* that can respond to wind flow. New materials are also investigated that are compatible with laser fabrication.

### 3.2.1 Design principles and transduction

Artificial sensory hairs or microtufts for flow sensing are typically 3D out-of-plane structures that undergo deflection when subjected to air flow. Most of these structures are modeled as fixed cantilevers that experience maximum strain at the point of attachment to the substrate (the base) when deflected. The integration of piezoresistive strain sensors allows for direct determination of the strain and thus the deflection the the sensory hairs or microtufts are subjected too. In other words, the flow velocity being sensed can be translated into a corresponding strain that can be sensed by the piezoresistors, which in turn would register a corresponding change of resistance. The other advantage of using piezoresistive sensing is the ease of fabrication, especially for MTM, where the process is directly applicable to this transduction mechanism with very little modification to the process. In this section, analytic models are used to describe both the piezoresistive transduction as well as deflection of these “cantilevers”. The transduction mechanism for all three fabrication techniques described

above are the same.

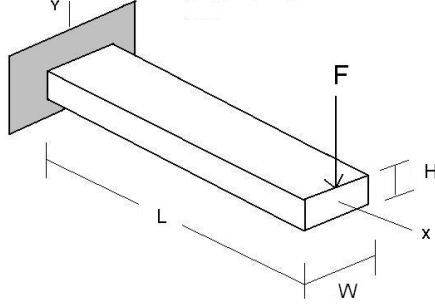


**Figure 12:** Modeling of a cantilever beam

Cantilever based structures are usually modeled as transversely loaded beams under pure bending [91]. Elementary solutions of the beam equation (Equation 6) exist under conditions of small deflection. For a cantilever beam with a point load at its end (Figure 12), the maximum deflection at the end of the cantilever of with the dimensions given in Figure 12 is given by:

$$w_{max} = \left( \frac{L^3}{3EI} \right) F \quad (6)$$

The corresponding maximum stress (Equation 7) and strain (Equation 8) developed at the base of the cantilever are given by:

$$\sigma_{max} = \left( \frac{6L}{H^2W} \right) F \quad (7)$$

$$\epsilon_{max} = \left( \frac{6L}{H^2WE} \right) F \quad (8)$$

In the actual testing environment, this deflection is induced by an imposed air flow in the wind tunnel and not by a point load and an illustration of the velocity profile that a sensor element might see is shown in Figure 13.

Thus all the flow sensors that are demonstrated in this research have piezoresistors placed at the points of maximum strain to maximize the output response. The output

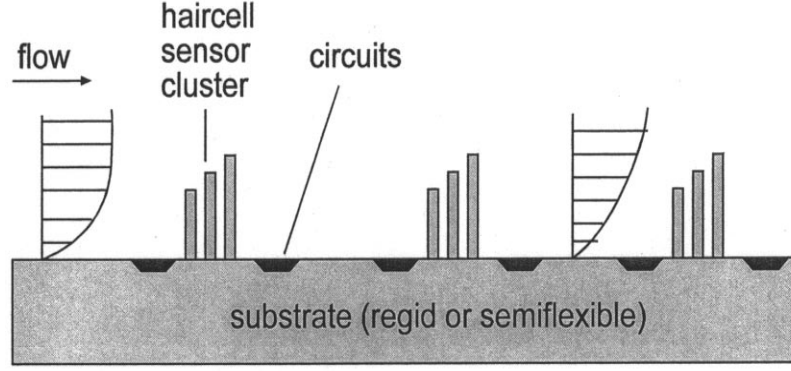


**Figure 13:** Velocity profile seen by the sensor (Fan et.al. [35])

response is usually sensed directly as a change in resistance and is related to the strain by the following expression:

$$\frac{\Delta R}{R} = G\epsilon \quad (9)$$

where  $\Delta R$  is the change in resistance observed for a given change in flow (and thus strain),  $R$  is the initial resistance of the device,  $G$  is the piezoresistive gage factor as discussed in section 2.1

From equation 8, it is clear that in order to maximize the strain for a given applied load  $F$ , either the geometry can be optimized to yield a low rigidity structure or the material itself can be chosen such that it has a low modulus, thereby increasing the deflection and the strain. This directly translates to an increase in the device response in the form of a higher change in resistance. The other factor to be considered is the piezoresistive gage factor that was discussed in Chapter 2. In summary, device sensitivity can be improved by controlling:

1. Geometry - high aspect ratio structures are less rigid and hence more flexible.

For real time scenarios where the devices are tested in the wind tunnel, the drag forces are higher for a rectangular geometry rather than a cylindrical geometry.

2. Device material - From equation 8, it can be seen that the Young's modulus of

the material is very important in controlling the maximum deflection and strain. A low modulus material such as an elastomer would yield a higher strain for the same applied force.

3. Gage factor of piezoresistor - a material with high gage factor is desired since that would also lead to an increased device response.

The following sections are dedicated to the three fabrication techniques which have been developed for microfabrication of artificial sensory hairs or microtufts for flow sensing.



## CHAPTER IV

### METAL TRANSFER MICROMOLDING

Soft lithography represents a non-lithographic approach to micromachining that has proved particularly useful in the fabrication of BioMEMS devices and microfluidics and other MEMS structures. It is an efficient, cost-effective and convenient method for making micro as well as nano-structures. Soft lithography uses an elastomeric stamp with patterned relief features on its surface to generate patterns and structures on another material [107]. The elastomeric stamp or the mold is usually prepared by cast molding of an elastomer like polydimethylsiloxane (PDMS), by pouring it over a master structure that has the required relief structure. The elastomer is cured and peeled off to give a negative replica of the master structure. The master structure itself is fabricated by conventional lithographic techniques, typically using a thick negative photoresist, SU-8. Soft lithography essentially comprises five main techniques, some of which are illustrated in Figure 14:

1. **Microcontact printing** uses the relief pattern on the surface of the PDMS mold to print self-assembled monolayers (SAMs) onto other substrates
2. **Replica molding (REM)** is a technique for duplicating a single master structure without actually having to pattern it by lithography every time. A negative copy of the master structure is made by casting PDMS. Subsequent copies of the master are made by casting polymers into this PDMS mold and demolding
3. **Microtransfer molding** is another patterning technique where the material to be printed is poured into the PDMS mold with the relief patterns. The excess material is scraped off from the surface and then placed in contact with

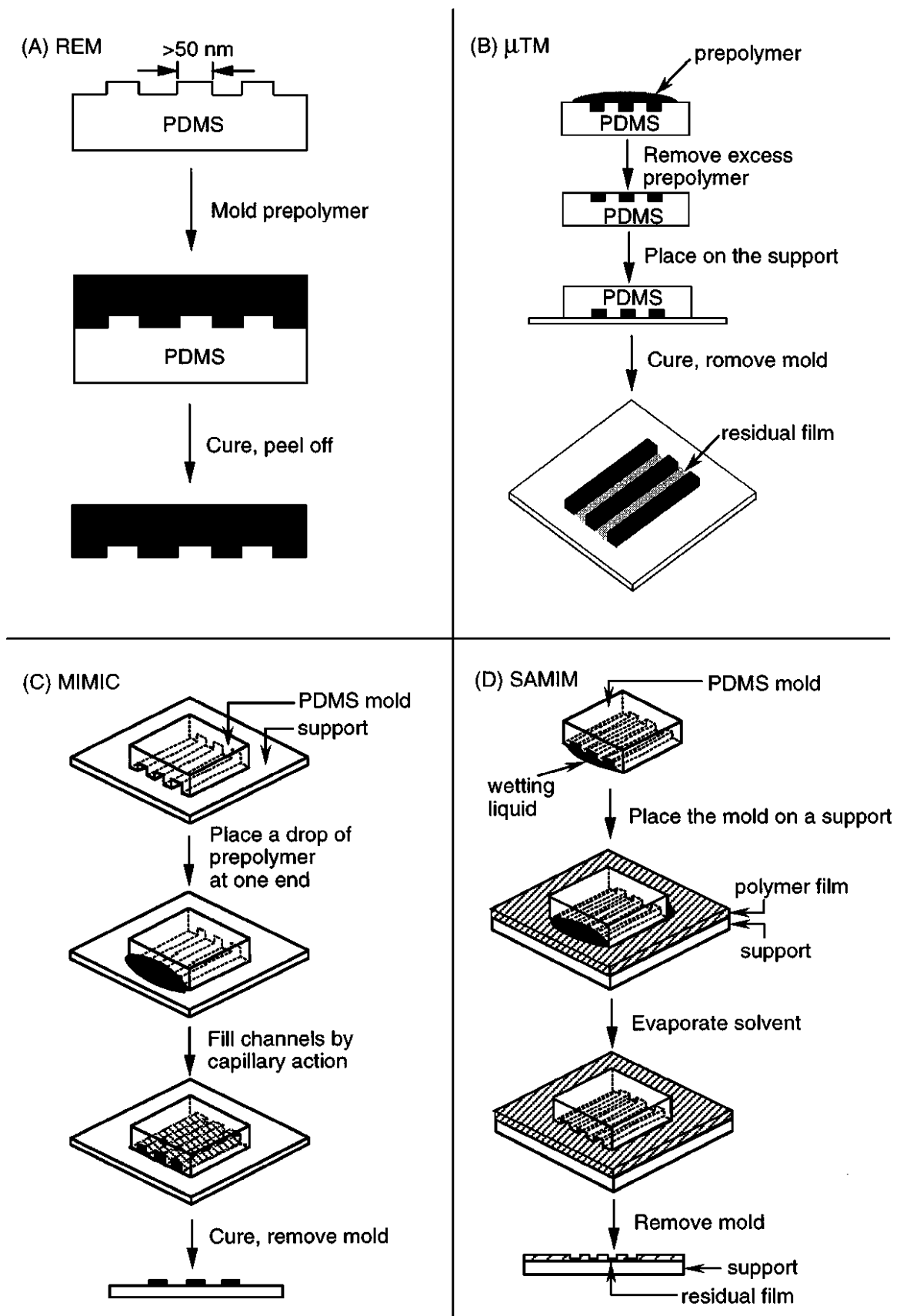


Figure 14: “Soft” micromachining techniques (Xia et.al. [107])

another substrate. The cast polymer is then thermally or UV cross-linked and the PDMS mold carefully peeled off leaving a patterned microstructure behind

4. **Micromolding in capillaries (MIMIC)** is achieved by placing the PDMS mold face down on a rigid substrate to form a network of empty channels between them. The casting polymer, typically a low viscosity material is then placed at the mouth of these channels and allowed to fill the channels spontaneously by capillary action
5. **Solvent-Assisted Micromolding (SAMIM)** generates features in a material that can dissolve in a solvent that does not attack the PDMS. The mold with the necessary pattern is wetted with the solvent and brought in contact with the surface to be patterned, usually an organic polymer. The solvent dissolves the material that it comes in contact with and the resulting gel is molded against the features in the mold

Micromolding, thus, is a powerful technique that has shown tremendous potential in replacing silicon as a device material, thereby reducing complexities in fabrication procedures, as well as costs. But, molding does not encompass the wide range of sensors that can be fabricated by silicon micromachining, primarily because achieving electrical functionality simultaneously with structural definition is not a well explored problem.

Metal transfer micromolding (MTM) is an attractive approach to achieve complex 3-D structures at low-cost and high volume while achieving microtexturing and electrical functionality simultaneously [106]. It is a fairly new technique that builds on the well established soft lithography technique, and allows one to fabricate devices with *electrical functionality*, vastly expanding the range of microsensors that can be fabricated using polymer MEMS technologies. In this section, the typical process

flow of the MTM process will be discussed, but the materials used here are pertinent to the application and are not the *typical* materials used. The applications that have been demonstrated for MTM [23, 86, 87, 106, 112, 113] all use a rigid polymer (Polymethylmethacrylate(PMMA), SU-8, PU etc.) which are well suited to the MTM process because of their strong metal adhesion (except PMMA) and ease of demolding. However, use of such materials for fabricating cantilever type structures which show large deflections under fluid flow conditions would be extremely challenging. Moreover, the high modulus of the material must be compensated by fabricating an extremely thin and high aspect ratio structure with low rigidity. As can be seen from the general fabrication sequence of MTM, it would be very difficult to do so, without causing heavy damage to the structure.

Hence, a slightly modified MTM process is proposed and demonstrated to suit the current application.

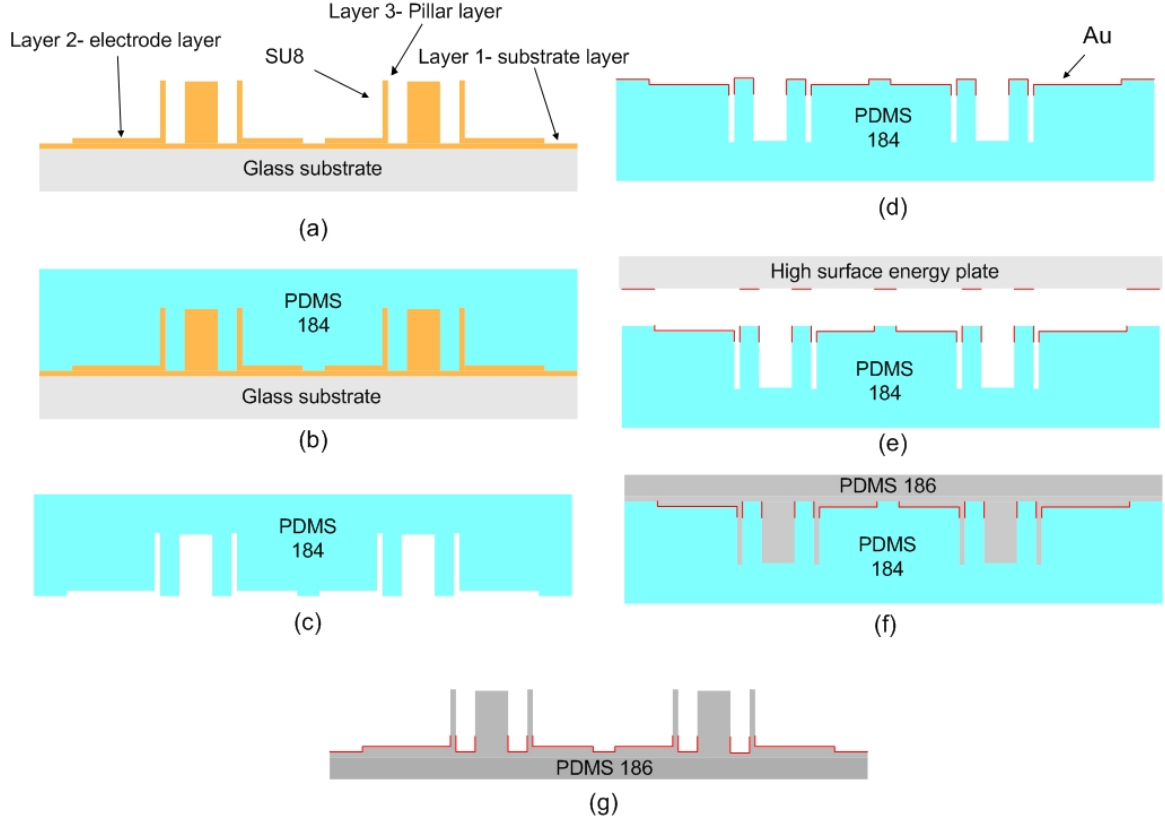
## ***4.1 Fabrication process***

The fabrication scheme is shown in Figure 15 and it consists of the following steps:

### **4.1.1 SU-8 photolithography**

The process sequence starts with fabrication of the SU-8 (Microchem Inc.) master structures by UV photolithography (Figure15(a)). SU-8 is a negative tone, epoxy based near-UV photoresist based on EPON SU-8 epoxy resin (from the Shell Oil Chemical) that was originally developed and patented by IBM [37, 68]. This photoresist can be processed to fabricate structures as thick as 2 mm. Aspect ratios of developed patterns greater than 20 have been demonstrated with standard contact lithography equipment at an exposure wavelength of 365 nm.

The structure consists of rectangular cantilevers with two electrodes for sensing the resistance change at the base of the cantilever (Figure 16). The SU-8 master is fabricated as a three layer structure using SU-8 2050. Piranha cleaned glass slides

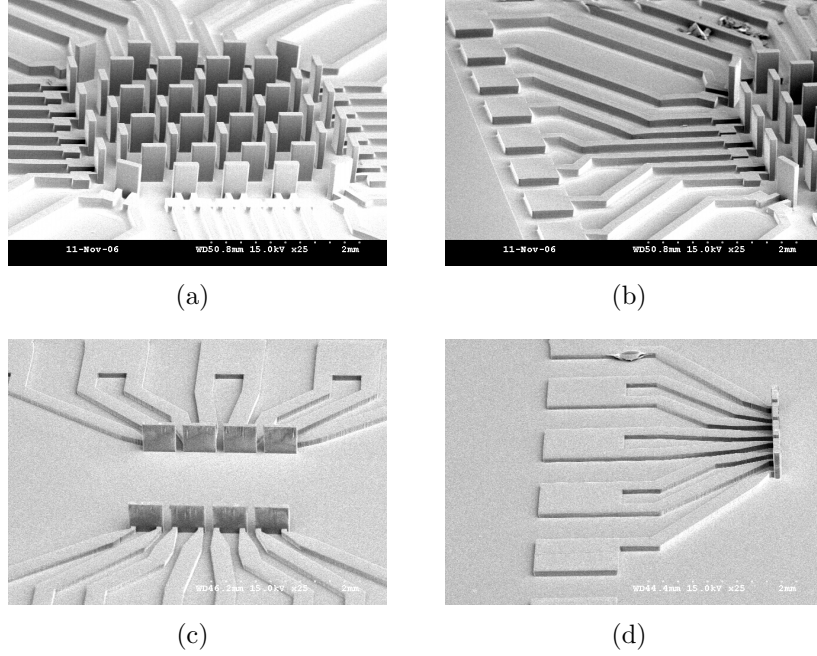


**Figure 15:** Fabrication process sequence for PDMS to PDMS MTM

are used as the substrate for the master fabrication. The soft-bake, exposure and post-exposure bake (PEB) conditions are given in Table 2. The sample is developed in Thinner-P developer (Rohm and Hass) for about 3 hours without stirring and then rinsed in Isopropanol (IPA) and dried. Scanning electron microscope (SEM) images of the fully fabricated SU-8 master structures are shown in Figure 16. The master structures are fabricated so that the final structure consists of patterns that are *protruding* from the substrate. The fully fabricated master structures have a Layer 1 (substrate layer) thickness of about  $200\ \mu\text{m}$ , a layer 2 (electrodes) thickness of about  $50\text{-}100\ \mu\text{m}$  and a Layer 3 (pillars) thickness of  $400\text{-}450\ \mu\text{m}$ . Figures 16(a),16(b) are for the original geometry, that has a Layer 2 thickness of about  $100\text{-}120\ \mu\text{m}$ . Figures 16(c),16(d) are for the updated geometry, as will be discussed later in the thesis, that has a Layer 2 thickness of about  $50\text{-}60\ \mu\text{m}$ .

**Table 2:** Process conditions for 3 layer SU-8 master fabrication

Layer	Spin speed	Soft Bake	Exposure dose	PEB
1	750/300/30	5:30 hrs at 95 <sup>0</sup> C	250 mJ/cm <sup>2</sup>	20 mins at 95 <sup>0</sup> C
2	1700/300/30	1 hr at 95 <sup>0</sup> C	200 mJ/cm <sup>2</sup>	15 mins at 95 <sup>0</sup> C
3	450/300/30	6 hrs at 95 <sup>0</sup> C	2100 mJ/cm <sup>2</sup>	30 mins at 95 <sup>0</sup> C

**Figure 16:** SEM pictures of the three layer SU8 master structures

#### 4.1.2 Molding and microtransfer printing

After successful fabrication of the three layer master, the structure is coated with a thin layer of gold (1000Å) with titanium (200Å) as the adhesion layer in the unifilm sputterer. A 10:1 mixture of PDMS elastomer base and curing agent (Sylgard 184, Dow Corning Inc.) is well mixed and degassed in a vacuum chamber to remove bubbles and then cast onto the SU-8 master pattern to obtain the negative replica (Figure 15(b)). It is then allowed to cure at a temperature of about 60<sup>0</sup>C for a period of 8-10 hours and separated from the master, yielding the PDMS mold (Figure 15(c)). At this stage in the process, microtexturing or replication of the microstructures required for the flow sensors has already been achieved. The negative PDMS mold now consists

of *depressions* at locations exactly corresponding to *protrusions* in the SU-8 master structure. The next step is adding electrical functionality to the structures. This is achieved by sputter depositing a layer of gold (4000Å @200Å/min), followed by an adhesion layer of titanium (400Å @200Å/min) on top using the unifilm sputterer (Figure 15(d)). The PDMS mold is rinsed briefly in IPA for a few minutes and dried at about 100°C for 30 mins before depositing metal on it. At this point, the gold film covers the entire mold and is not yet patterned. The patterning is achieved by bringing a high surface energy plate in contact with the mold, transferring the metal on the protruding surface to the plate in a 2-D metal transfer scheme (Figure 15(e)). A photomicrograph of the patterned metal is shown in Figure 17.

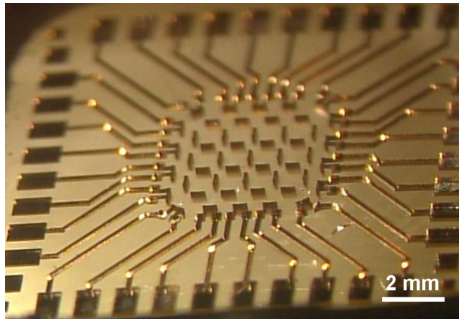


**Figure 17:** Patterning of Au on PDMS mold using microtransfer printing

The metalized PDMS mold is then surface treated in a plasma reactive ion etching system (RIE, Plasma Therm Inc.) using the parameters shown in Table 3 for about 1 minute. This ensures an easier release of the subsequently cast polymer.

**Table 3:** Process conditions for surface treatment of the metalized PDMS mold

Gases	Power	Pressure (mTorr)
CHF <sub>3</sub> (45 sccm), O <sub>2</sub> (5 sccm)	200 W	200

### 4.1.3 Final device fabrication

A 10:1 mixture of PDMS 186 (Dow Corning inc.) elastomer base and curing agent is then mixed and degassed and subsequently cast into the PDMS 184 mold with the pre-patterned metal film (Au/Ti) and cured at room temperature for a period of about 24 hours (Figure 15(f)). The structures are then demolded, whereby the metal film preferentially transfers to the casting polymer (PDMS 186), yielding the final device with electrical functionality (Figure 15(g)). Photomicrographs of the final device are shown in Figure 18.

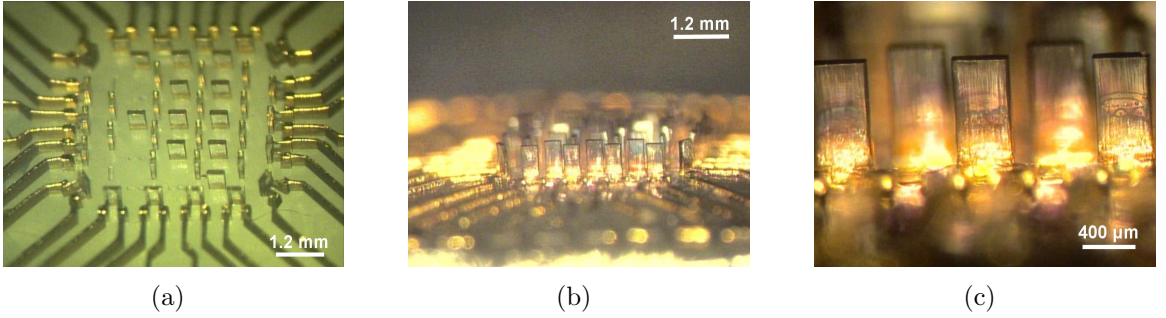


**Figure 18:** Final device photomicrographs. Figure 18(a) and Figures 18(b), 18(c) belong to different fabrication iterations. Figure 18(c) is the close-up of Figure 18(b)

Once the device is fabricated, interconnection to the external circuit is achieved using conductive silver ink (Ekote Inc.), which is used to wire bond fine wire (100  $\mu\text{m}$  diameter) onto the individual bond pads on the device, manually. Once the solvent in the conductive ink evaporates, it holds the wire in place on the bond pads. To further strengthen the connection, quick set epoxy is used. This procedure is repeated for each bond pad as shown in Figure 19.

## 4.2 Discussion

1. The development of the fabrication process sequence presented technical challenges at various point starting with the SU-8 master fabrication. Thermo-mechanical stresses leading to delamination of SU-8 from the substrate is a well



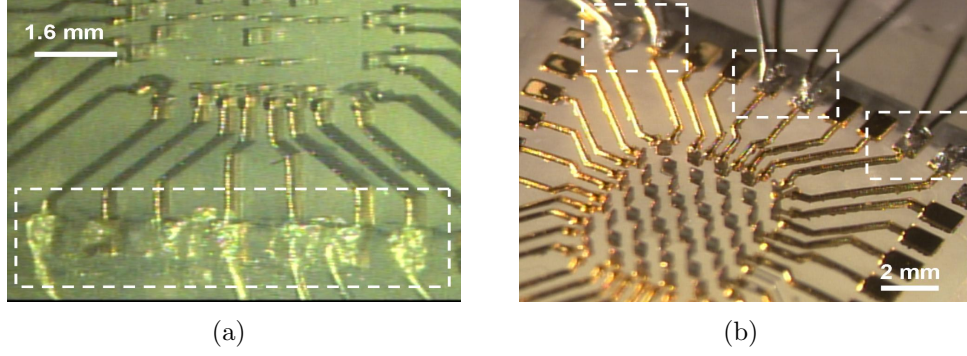


**Figure 19:** Interconnections of the final device to the external circuit

known phenomenon and has been extensively studied [3, 13, 46, 53]. These stresses arise during soft bake and the post exposure bake steps in the processing due a coefficient of thermal expansion (CTE) mismatch between SU-8 and the substrate (glass in this case). SU-8 has a CTE of about 52 ppm/ $^{\circ}\text{C}$  and glass has a CTE of about 9 ppm/ $^{\circ}\text{C}$ . The baking conditions are modified to run the bake for longer times at lower temperatures to alleviate this problem. But, when processing mutiple layers of ultra-thick SU-8, this could increase the processing time significantly. Hence, a new technique is proposed whereby the problem with SU-8 delamination is solved.

A *blanket* layer of SU-8 (about 200 microns thick) is first spun onto the glass slide and baked. Following the bake step, this layer is flood exposed without a mask, followed by a PEB. The remaining two layers are processed as usual. In such a scheme, different layers of SU-8 see a different number of bake (soft bake as well as PEB) steps, which are summarized in Table 4.

**Table 4:** Number of baking steps seen by different layers in the 3 layer process (Layer 1 is the bottomost layer)

Layer	# of Soft bakes	# of PEBs	Total # of bakes
1	3	3	6
2	2	2	4
3	1	1	2

Thus, the bottommost layer, which is in direct contact with the substrate would experience the most stress due the number of thermal cycles it is subjected to and thus it delaminates off the substrate. But the *active* layers of the master structure are layers 2 and 3, which are sitting on top of layer 1, the *substrate layer*. Thus, even though delamination occurs, the master structures are still unaffected.

2. Two different kinds of master structures are fabricated. Figures 16(a) and 16(b) show the fabrication of a densely populated array with the functional pillars consisting of only those that lie along the periphery of the structure. Figure 16(c) and 16(d) show a different design where all the pillars occupy only one row. The latter represent the final changes in the design to account for the obstruction of the fluid flow by other pillars in the preliminary dense array.
3. A fluorine plasma treatment is done on the PDMS molds after metal deposition and microtransfer printing. This acts like a release step, to increase the ease of demolding of the final device. Without this surface treatment, the casting PDMS (PDMS 186) would stick to the mold PDMS (PDMS 184).
4. Two different types of PDMS are used in the process. PDMS 184 and PDMS 186, which differ in their molecular weights, with the latter being the higher molecular weight elastomer. It was initially found that the transfer of metal between PDMS 184 and PDMS 184 was only partial, but the transfer to PDMS 186 was near 100%.
5. To ensure that a 100% metal transfer is achieved, an adhesion layer of titanium (Ti) is deposited on top of the gold (Au). Thus, the casting polymer (PDMS 186) is in direct contact with the adhesion layer and the original mold polymer, PDMS 184, is in direct contact with low surface energy Au. This scheme ensures that all the metal is transferred to the casting PDMS 186.

6. As equations 6, 7, 8 have shown, the maximum strain occurs at the point of attachment of the pillar to the substrate. Thus, the piezoresistors would have to be positioned close to the point of attachment. Patterning of thin film metal on the side walls of a 3-D high aspect ratio structure is extremely challenging, especially when using MTM. The metal in this case is deposited by a DC sputtering process and it is well known that sputtering of thin films leads to conformal coverage, including coverage on the side walls of the structure. In this case, the extent of side-wall coverage is a strong function of the geometry of the trench opening. The trenches in the PDMS mold (for the pillars) are roughly 70-100 microns by 400 microns (Figures 16(a),16(c)). For this opening size, the metal coverage on the side walls of the pillars extends upto 50-60 microns (roughly), which represents the region of maximum strain. Thus, one direct consequence of using the MTM process is side-wall coverage of the piezoresistive thin film, without adding any complexity to the process.

### ***4.3 Testing results***

The initial testing of the devices is conducted using a four point measurement by deflecting the sensing pillars using probe tips as shown in Figure 20. The deflection is estimated by capturing images of the deflected pillars using the camera attached to the probe station. A constant current supply is used to supply a current of about 5mA, while a voltmeter is used to record the changes in voltage. Table 5 shows the results of the deflection tests.

A second deflection experiment conducted on a different device is shown in Table 6. In this experiment, the deflection is cycled between 0 and 8.75 microns and the hysteresis in the starting resistance is studied. The change in resistance over the number of cycles is also recorded. Figure 21 shows the device response to the cyclic deflection tests.

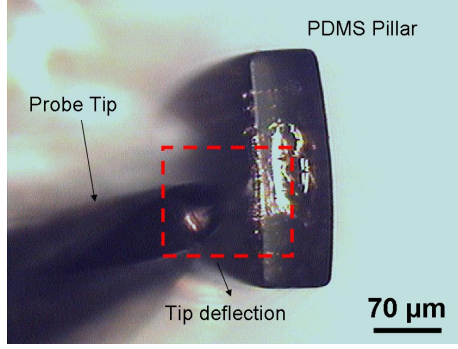


**Figure 20:** Deflection of the sensing pillar using a probe tip

**Table 5:** Deflection testing results. ‘-’ indicate intermediate deflections which were not recorded

Deflection( $\mu\text{m}$ )	Voltage(mV)	Resistance ( $\Omega$ )	Change in resistance ( $\Omega$ )
0	276.8	55.36	0
-	280.8	56.16	0.8
67.5	288	57.6	2.24
-	289.5	57.9	2.54
200	290	58	2.64

One of the possible causes of such variations in response is the poor interconnection scheme used. The wire-bonding is done manually and the silver ink used does not bond effectively to the gold pads on PDMS, leading to huge contact resistances. Moreover, even though a four point scheme is used to eliminate this contact resistance, the bonding is so unstable that it became difficult to differentiate between the response

**Table 6:** Cyclic deflection testing results.  $D_i$  is the starting deflection;  $D_f$  is the final deflection;  $R_i$  is the initial resistance corresponding to  $D_i$ ;  $R_f$  is the final resistance corresponding to  $D_f$

Expt. #	$D_i(\mu\text{m})$	$D_f(\mu\text{m})$	$R_i(\Omega)$	$R_f(\Omega)$	$\Delta R (\Omega)$
1	0	8.75	106.535	107.906	1.371
2	0	8.75	107.906	108.469	0.564
3	0	8.75	108.469	109.711	1.241
4	0	8.75	109.711	110.652	0.941
5	0	8.75	110.652	111.231	0.579
6	0	8.75	111.231	111.548	0.317

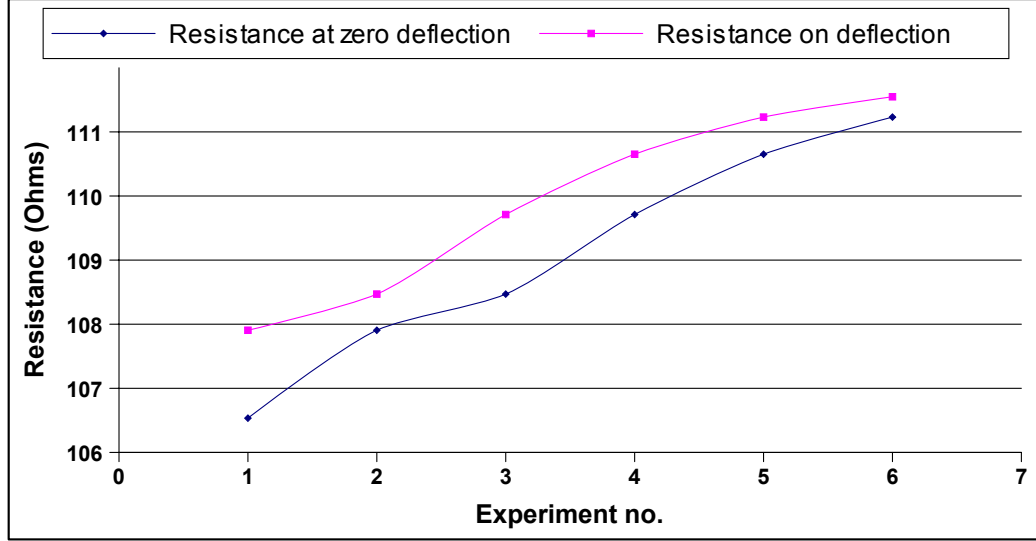


**Figure 21:** Change in device response with # of experiments for cyclic  $8.75 \mu\text{m}$  deflections

of the sensing element (the pillar) and variations due to shifting of the contact wires. The next chapter discusses another interconnection technique used that effectively eliminates any variation due to the contacts. The next section discusses the other possible causes of variation of response of devices fabricated using the modified MTM process.

#### 4.4 *Technical issues with MTM*

To summarize, the conventional MTM process that utilizes “rigid” casting polymers such as SU-8, PMMA etc., has been modified to suit the application, which requires large deflection and strains, by using an elastomer as the mold material as well as the casting polymer. Thus, the thin metal film deposited on the mold is now transferred to a *soft material* that is capable of suffering large deformations. This represents the biggest problem while using MTM to fabricate an all elastomer device.

The testing results (Tables 5,6 and Figure 21) clearly show the large difference in resistance between two devices fabricated using the same technique, and both are much higher than the theoretical resistance. This also means that controlling the

device response and device repeatability would be very challenging. One possible cause of the drift is the temperature coefficient of resistance of the gold film (TCR), and the other cause is the variation in the structure of the gold film.

It has often been reported that gold, aluminum and copper films, free-standing or polymer supported, rupture at strains of 1%-2% [58, 59, 66]. This phenomenon, known as micro-cracking, greatly affects repeatability of performance and device yield. Although the strains that are expected during actual device operation fall in the low strain regime (2% or less), the step that leads to device failure or poor yield is the final demolding step in the MTM process. Because the process involves application of physical forces to separate the two elastomeric pieces (the mold and the final device), both undergo considerable deformation causing irreparable damage to the metal thin film. Thus, most of the devices fabricated by this technique are either completely damaged or the resistance is extremely high (as can be seen from Table 5). Figure 22(a) shows a close-up of the metal film on the final PDMS 186 device fabricated using MTM.

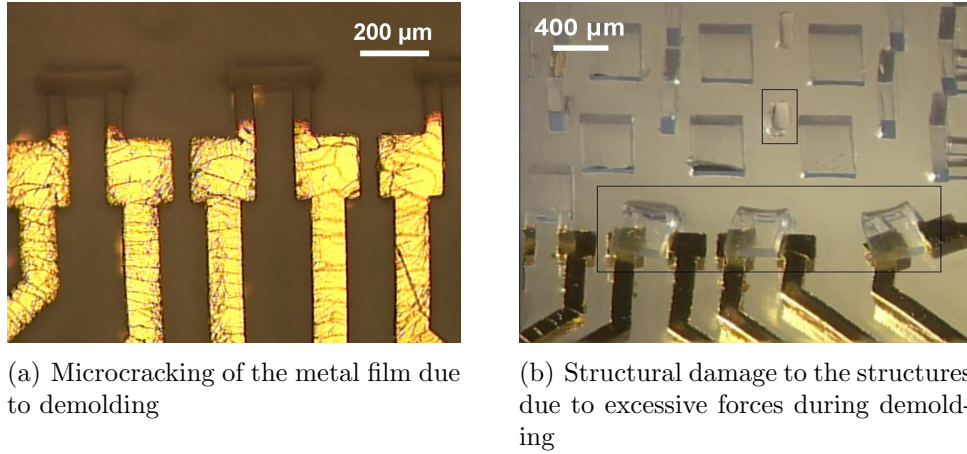


**Figure 22:** Technical issues with MTM

The other problem commonly observed while using MTM with elastomeric materials is structural damage to the device, caused by application of excessive forces, possibly in combination with the low tear strength of PDMS ( $\sim 2.6\text{kN/m}$ ), that are

often required during the demolding step. Figures 22(b) and 18(a) demonstrate this.

The problems with the device response (large drifts in resistance and hysteresis, inconsistent device response over time etc.) may well be caused by the poor metal film quality. Since the metal is deposited on an easily deformable polymer, minor forces during handling of the mold can also cause damage to the metal film. Thus, in some cases, the metal film may already be cracked or even *warped* before the metal transfer even takes place. This is demonstrated in Figures 23(a) and 23(b). However, it must be noted that this by itself is not responsible for device failure, as the microcracking here is well below the failure regime.

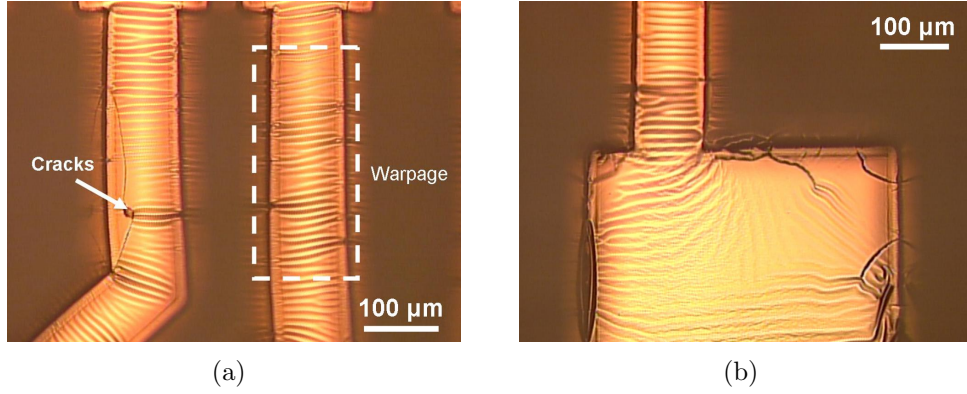


**Figure 23:** Damage to the metal film on the PDMS mold after microtransfer printing

Hence, although a new MTM process has been proposed and demonstrated, it is unsuitable given its incompatibility with the set of materials being used. Thus, given the nature of the application, other techniques must be explored if metal on elastomer is to be used as the device materials. The subsequent chapters are dedicated to establishing fabrication processes that solve the issues discussed here.

## CHAPTER V

### DISSOLVING MOLD METAL TRANSFER MICROMOLDING

Sacrificial polymers/materials form an important class of materials for micromachining applications in MEMS, especially in *surface micromachining* of silicon [16]. Linder et.al. [67] have also reported on water soluble sacrificial layers suited to surface micromachining applications. In this section, a process is proposed and demonstrated for the fabrication of an all elastomer flow sensor using a *dissolving* or *sacrificial* mold, which overcomes some of the technical challenges pertinent to the current application that were encountered while using the conventional MTM process.

#### ***5.1 Identifying problems with conventional MTM***

Section 4.4 highlighted some of the technical issues that were encountered while using the conventional MTM process to fabricate all elastomer PDMS devices. In summary, some of the problems observed in devices fabricated using MTM are:

- Device resistances far exceeding theoretically calculated values for thin gold films (Table 6)
- Variability of device response and large drifts in resistance
- Hysteresis and non repeatability of results for same values of deflection (Figure 21)
- Structural damage to the final device

It was proposed that irreparable damage to the thin metal film was caused by the forces applied to demold the cured casting polymer (PDMS 186) from the mold



material (PDMS 184). Figure 22(a) clearly demonstrates the presence of large cracks in the metal film after demolding. This often leads to near zero yields of devices. Repeated experiments with conventional MTM yield the same results as far as damage to the metal thin film as well the structure are concerned. Both high aspect ratio rectangular pillars as well as tapered microneedle structures were fabricated using this process to demonstrate that the damage caused is a flaw inherent to the process and is independent of the structures being fabricated. Figure 24 reveals the same issues in fabrication of tapered microneedle structures as seen with vertical side-walled pillars. All devices are fabricated using PDMS 186.

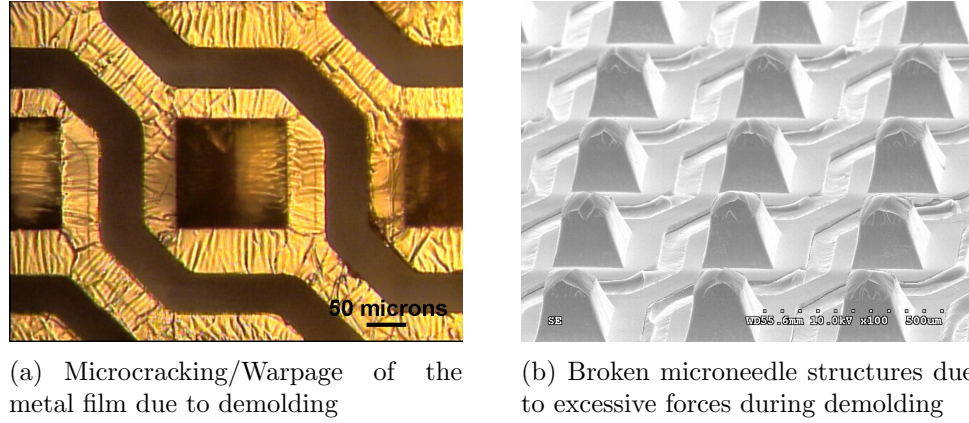


**Figure 24:** Problems observed with microneedle structures fabricated by conventional MTM

From the fabrication process sequence shown in Figure 15, it can be seen that the final demolding step is a physical step and would involve large forces that cause the damage described above. Hence, in order to successfully use MTM to fabricate electrically functional devices, it is essential *to eliminate the need for a demolding step*, especially given the fact that device sensitivity required for the proposed application must be high and the performance robust. Thus, an extra modification is incorporated into the conventional MTM process and a novel dissolving mold metal transfer molding (DMTM) process is proposed, where the conventional PDMS mold is replaced by a sacrificial or dissolving mold that can be dissolved in an appropriate solvent, without

applying any physical forces to separate it from the device material. It is shown in the following sections that this new process greatly enhances device yield with excellent metal film quality.

## 5.2 Fabrication process

The fabrication process sequence is shown in Figure 25.

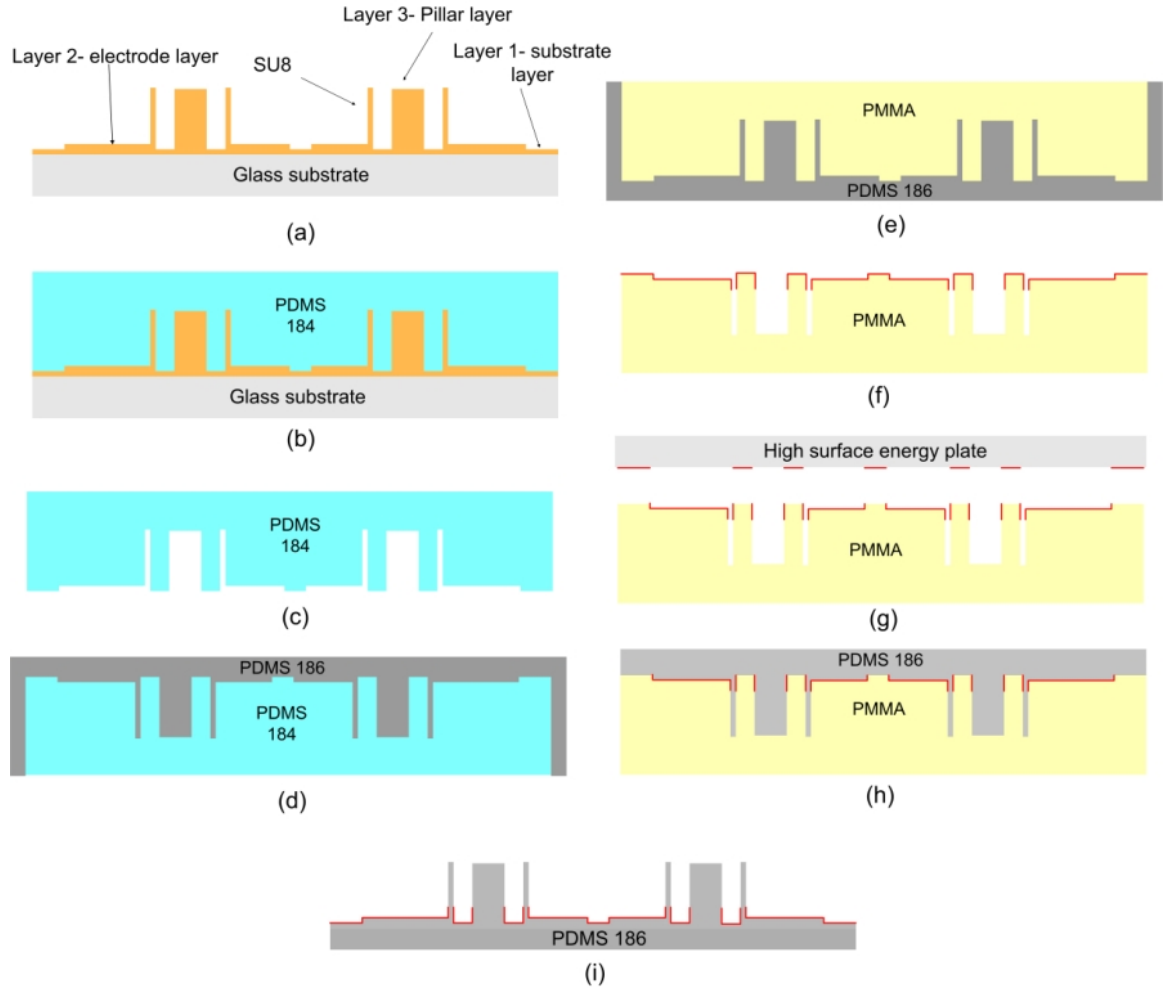


**Figure 25:** Fabrication process sequence for the dissolving mold MTM process

- The first few steps of the process are the same as in the conventional MTM process. The SU-8 master fabrication (Figure 15(a)) and subsequent casting and demolding of the PDMS 184 negative mold (Figures 15(b) and (c)) are

used as such in the dissolving mold MTM process, without any modifications as shown in Figures 25(a),(b) and (c). After the fabrication of the PDMS 184 negative mold, it is plasma treated using the same recipe as shown in Table 3. The plasma treatment reduces the adhesion between the two elastomers. PDMS 186 is then processed and cast into the mold using the same conditions as described in Section 4.1.3 (Figure 25(d)). The two molds are then carefully demolded to prevent any damage to the structures. At this point, a PDMS 186 master structure is obtained.

- For the dissolving mold MTM process, the PDMS 186 *master* structure is the reusable structure, as against the conventional MTM process, where the PDMS 184 *mold* is reusable. The next step is the casting of the sacrificial material that forms the dissolving mold (Figure 25(e)). Details of the dissolving mold materials and their processing will be covered in the next section. The casting polymer is usually processed by solvent casting and is a thermoplastic polymer that can be dissolved by a variety of solvents. The materials chosen have excellent film forming properties, which is very critical in forming a mold with very smooth surfaces, an important requirement for the process. Once the solvents in the casting thermoplastic polymer are evaporated, the sacrificial/dissolving mold can be easily demolded from the PDMS 186 master structure without any damage to the master structures.
- Metal is then deposited on the dissolving mold using the same conditions as was used for the conventional MTM process (4000Å of Au, followed by 400Å of Ti using the Unifilm sputterer). As before, the patterning is achieved by bringing a high surface energy plate in contact with the mold, transferring the metal on the protruding surface to the plate in a 2-D metal transfer scheme (Figure 25(g)). When using water soluble sacrificial materials, it is necessary to coat its

surface with a low surface energy material before the metal deposition since the microtransfer printing process requires poor adhesion between the metal film and the underlying surface.

- Once the metal is patterned, the casting polymer (PDMS 186 in our case) is poured into the mold and cured at room temperature (Figure 25(h)) (the procedure is different for the water soluble polymer used, as will be explained in Section 5.3.2) for 24 hours (conditions same as used in Section 4.1.3). The final step is separating the casting polymer from the mold. In the dissolving mold process, this is achieved without the application of any physical force, but by using an appropriate solvent to dissolve the mold material, whereby all the metal transfers to the casting polymer (Figure 25(i)), almost always with 100% efficiency. The quality of the metal film is also vastly improved as compared to the conventional MTM process.

### ***5.3 Dissolving molds-materials and processing***

A number of materials are available that are commonly used in MEMS as sacrificial materials. Linder et.al.[67] have published an excellent paper reporting the use of a number of water soluble sacrificial materials in MEMS surface micromachining. Schmitz et.al. [90] have reported the use of a *lost mould process* for the fabrication of high aspect ratio micro-hair sensor arrays. The one thing common to all the literature reporting sacrificial materials is the fact that they are all used for *releasing* other structures. Even in the case of the dissolving mold process, the main purpose of the dissolving mold is to *release* the casting polymer without having to demold it. But it also has the additional advantage of adding electrical functionality simultaneously with structural definition. In this section, details of the fabrication process will be discussed, focussing primarily on the materials aspects of the process.

### 5.3.1 Polymethylmethacrylate (PMMA) molds

Polymethylmethacrylate (PMMA) was the first sacrificial material to be considered for the dissolving mold process, primarily because it was already being used for the fabrication of multielectrode arrays (MEAs) [87] and microneedles for electroporation [23]. The PMMA molds are made by solvent casting a 20%(by weight) solution of PMMA (average MW  $\sim 75,000$ , Scientific polymer products Inc.) in ethyl lactate solvent (97%, Acros Organics). The PMMA solution is prepared by mixing the PMMA powder and the ethyl lactate solvent in a ball mill for 2 days. It is then poured into the PDMS 186 molds and placed on a contact hot plate at  $55^{\circ}\text{C}$  for a period of 2-3 days, until all the ethyl lactate solvent has evaporated. Multiple casts of the PMMA solution (2-3) are required to completely cover the PDMS structures. The PMMA *mold* is then easily demolded from the PDMS master structure, yielding the dissolving mold for subsequent metal deposition, patterning and final device fabrication. Photomicrographs of the PMMA molds after the microtransfer printing of the metal are shown in Figure 26(a). Figure 26(b) shows a *PDMS* mold after microtransfer printing of metal deposited under the same conditions. Both pictures were taken at the same magnification (10x).

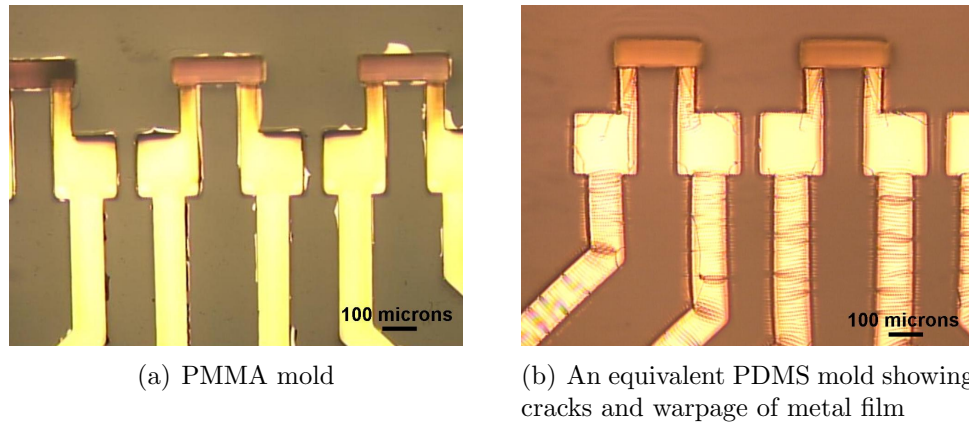


**Figure 26:** Comparison of PMMA and PDMS molds after microtransfer printing

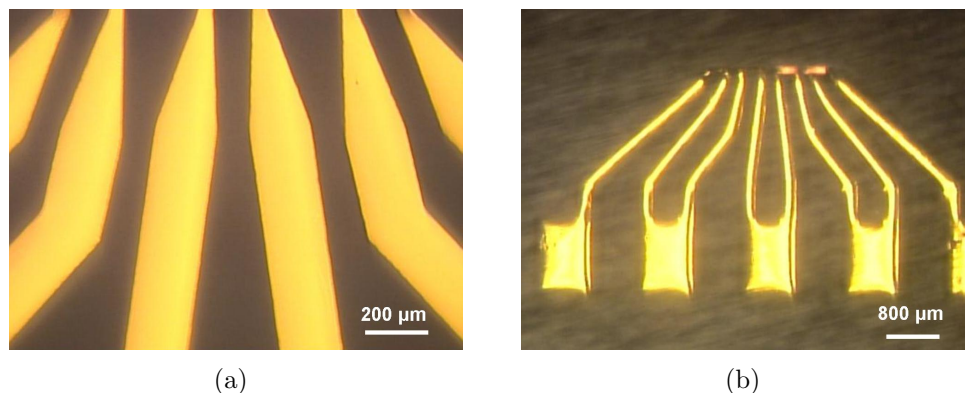


**Figure 27:** PMMA molds after microtransfer printing

#### 5.3.1.1 Dissolving the PMMA mold

After microtransfer printing of metal film, PDMS 186 is cast into the mold and cured as usual. The sacrificial PMMA mold then has to be dissolved to achieve the metal transfer and release the PDMS structures. A number of solvents are available for dissolving PMMA like acetone, ethyl lactate, propylene glycol methyl ether acetate (PGMEA) etc., but for use with the dissolving mold process, not all solvents can be used. The solvent chosen for the process must not swell the casting polymer (PDMS 186) at all or the swelling caused must be negligible. This has a direct bearing on the metal film quality. If the PDMS swells too much, the expansion will cause the metal film to either delaminate or crack. In either case, the damage is irreparable. This is the single most important criteria while selecting from the vast array of solvents available.

After some experimentation, it is found that 1-methyl-2-pyrrolidinone (NMP) (99.5%, anhydrous, Sigma-Aldrich) causes the least amount of swelling of the PDMS and the metal quality on the final device is excellent. PGMEA (Thinner P, Rohm and Hass) and ethyl lactate are also tried as solvents, but the results obtained are not as good as with NMP. The dissolving mold along with the cured casting PDMS 186 are placed in a beaker containing NMP solvent for about 2 days to ensure that all the PMMA is completely dissolved. Stirring is used to ensure that the PMMA always

receives a supply of fresh solvent. After complete dissolution (this is confirmed by analysis in the microscope as well by probing the surface of the PDMS), the sample is dried in a convection oven at a temperature of around 40°C to 50°C. The results of the fabrication are shown in Figures 28(a),28(b),28(c),28(d).

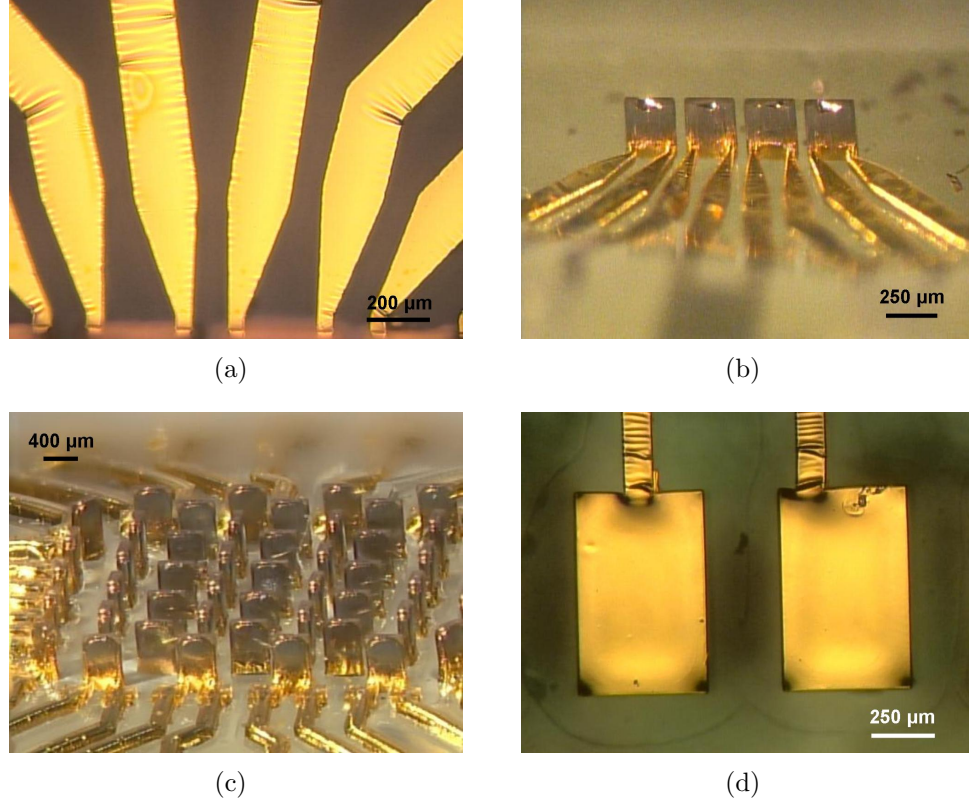


**Figure 28:** Final PDMS 186 devices for the two designs after dissolving the PMMA mold. Figures 28(a) and 28(a) are of the updated geometry; Figures 28(c) and 28(d) are for the old geometry

Upon dissolution of the sacrificial mold, the metal transfers to the casting polymer, as in the case of conventional MTM, but this time around, the transfer is almost always 100% and the metal film quality is excellent with little or no microcracking observed. In addition, there is no structural damage to the structures, which highlights the applicability of the process to applications requiring metal patterning on 3-D elastomeric structures.

### 5.3.2 Polyacrylic Acid (PAA) molds

Although using PMMA as a sacrificial material yields excellent results in terms of metal film quality and damage to the structures, it is always ideal to use a sacrificial material that can be dissolved in water. Water is a benign solvent and it extends the range of casting polymers that can be used for fabricating the final device by the dissolving mold process. Some of the disadvantages of an organic solvent based sacrificial material (PMMA) are:

1. Different solvents must be used for different casting materials, since different polymers react differently to different solvents. For e.g., NMP must be used when the final device must be fabricated using PDMS. The use of acetone (which dissolves PMMA much faster), would cause the PDMS to swell and thus damage the metal film. When using polyurethane (PU) (Smooth-Cast 310, Smooth-on Inc.), NMP cannot be used since it degrades the PU. In fact, PU is attacked by almost all the solvents tested (NMP, Ethyl lactate, PGMEA etc.).
2. Some of the casting polymers commonly used to fabricate final devices (SU-8 etc.) by solvent casting, contain solvents that dissolve the PMMA, which prevents their use.

For the reasons stated above, a water soluble mold material is investigated and used for the fabrication. The Whitesides group at Harvard have worked extensively on water soluble polymers for *surface micromachining* applications. The sacrificial materials investigated by them are deposited by spin coating and in the form of thin films. But, they can also be used for solvent casting, as will be described below. Figure 29 gives a list of the water soluble sacrificial polymers that are potentially useful in surface micromachining as well as in the dissolving mold fabrication [67].



	Film solubility in water <sup>[b]</sup>		Film solubility in water after photolithography <sup>[c]</sup>	Roughness (RMS in nm) <sup>[d]</sup>
	[a]			
Poly(acrylic acid)	good	good	good	0.28
Dextran	good	good	good	0.27
Poly(methacrylic acid)	good	good	good <sup>[e]</sup>	—
Poly(acrylamide)	good	good	irreproducible	—
Poly(ethylene imine)	good	only in acidic or alkaline media	—	—
Poly(vinyl alcohol)	good	insoluble	—	—
Poly(ethylene oxide), 2 kDa	good	good, but also soluble in organic solvents	—	—
Poly(ethylene oxide), 100 kDa	Not uniform	—	—	—
Chitosan	Not uniform	—	—	—
Sucrose (table sugar)	Not uniform	—	—	—

[a] The films were prepared by spin-coating (3000 rpm, 15 s) from a 5% (w/v) polymer solution in water, except for the polymers with a poor solubility in water, including poly(ethylene oxide) (100 kDa; 1% w/v), poly(methacrylic acid) (1.7% w/v), and poly(vinyl alcohol) (2.5% w/v). The films were then dried by placing the substrates on a hot plate at 150°C for 2 min. "Good" is a subjective finding of fewer than two inhomogeneities detectable by optical microscopy (bright-field mode) on a 3-inch wafer. [b] "Good" indicates that dissolution of the film in water required less than 1 s. [c] "Good" means that disks of SU8-2010 photoresist could be lifted-off in water (refer to text for further details). [d] Root mean square (RMS) roughness of the film as measured by AFM. Before preparation of the films, we measured a RMS roughness of 0.21 nm on silicon substrates. [e] The poor solubility of the polymer in water limits the range of film thicknesses that can be prepared, in comparison to dextran and PAA (see text for details).

**Figure 29:** Selection of water soluble sacrificial polymers (Linder et.al. [67])

### 5.3.2.1 Casting

Of the polymers shown in this list compiled by the Whitesides group, Polyacrylic Acid (PAA)(50 kDa, Polysciences Inc.) is initially chosen and tried for use in the dissolving mold process. Solvent casting of PAA solution with different concentration of solids (15%,20% and 25% by weight) is tried by pouring the solutions into the PDMS masters at temperatures of 40°C-50°C for a period of about 2 days. But, unlike the PMMA solutions, where bubble formation and trapping rarely occurs, bubbles spontaneously form with PAA solutions and are trapped in the mold once all the water evaporates. Different experiments are tried where the PAA is cast into the PDMS master structure at room temperature. A pipette is used to remove some of the bubbles formed initially, but the formation and trapping of the bubbles could not be completely eliminated. Figure 30(a) shows a PAA mold made by conventional solvent casting technique at a temperature of 40°C with trapped bubbles.

Thus, a different technique, based on centrifugation [62], is used to make the PAA

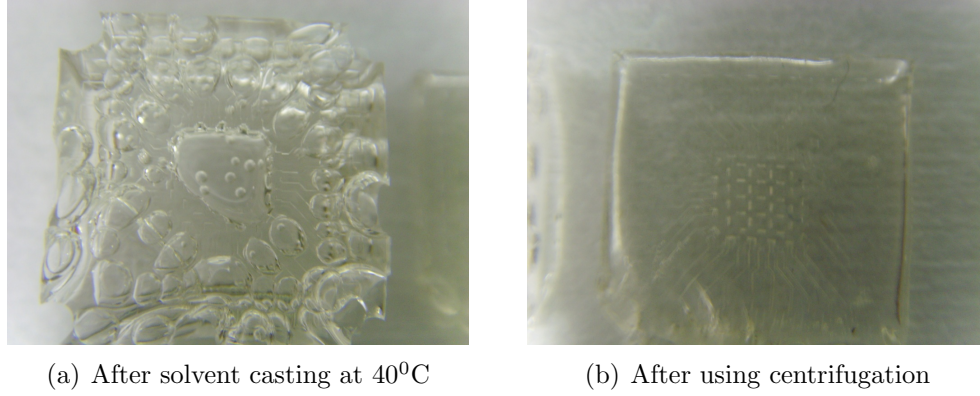


**Figure 30:** Comparison of the quality of PAA molds made using two different techniques

molds, that completely eliminates the problem with the formation and trapping of bubbles. To fabricate the sacrificial mold, 100-300 mg of a highly concentrated solution of PAA in water ( $\sim 90\%$ ) is placed on the PDMS master structure and centrifuged in a rotor (5702 RH, Eppendorf, NY) at  $3000 \times g$  and a temperature of  $42^\circ\text{C}$  for upto 4 hours. The sample is then allowed to remain at room temperature overnight, by which time the remaining water in the sample also evaporates and the PAA is ready for demolding. Using this technique, PAA molds with very smooth surfaces and no trapped bubbles are obtained. Figure 31 depicts the centrifugation process. Figure 30(b) shows a sample PAA mold made using the centrifugation process.

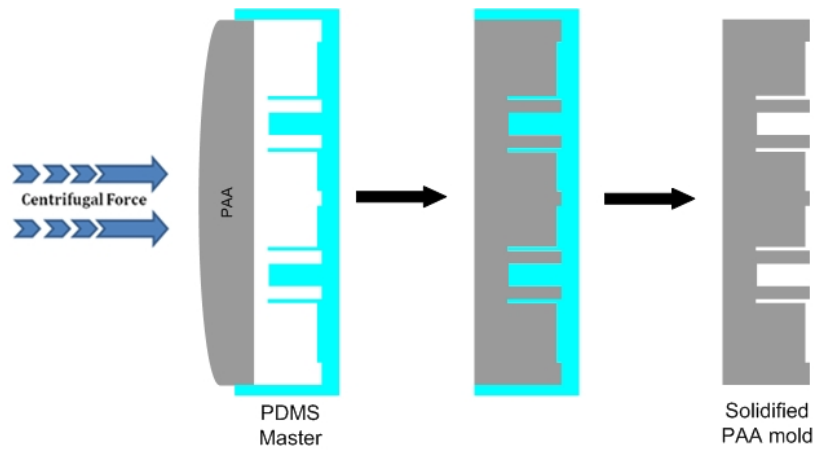


**Figure 31:** The centrifugation process for making the PAA mold (Adapted from Lee et.al. [62])

### 5.3.2.2 Microtransfer printing-spray coating of PDMS

Subsequent to fabrication of the PAA molds, metal is deposited. But, unlike the PMMA mold where the metal adhesion is very weak, the PAA molds exhibited strong enough adhesion with the metal to prevent microtransfer patterning of the metal. The strong metal adhesion is possibly due to the polar nature and thus high surface energy of PAA. Thus, to pattern the metal film, a low surface energy material has to be coated on the PAA mold, on which the metal can be subsequently deposited and patterned.

In MTM, PDMS is always used as the mold because of its low surface energy. Hence, it is an ideal candidate when choosing low surface energy materials for coating on the PAA mold. Conventional coating processes such as spin coating and dip coating cannot be used since a conformal thin coat of high aspect ratio trenches would be difficult to obtain. Spray coating of photoresist has often been used to pattern 3-D structures for MEMS applications [83]. PDMS has also been spray coated to fabricate ultra-thin non porous membranes by thinning it with a solvent [89]. A typical spray coating setup used is shown in Figure 32.

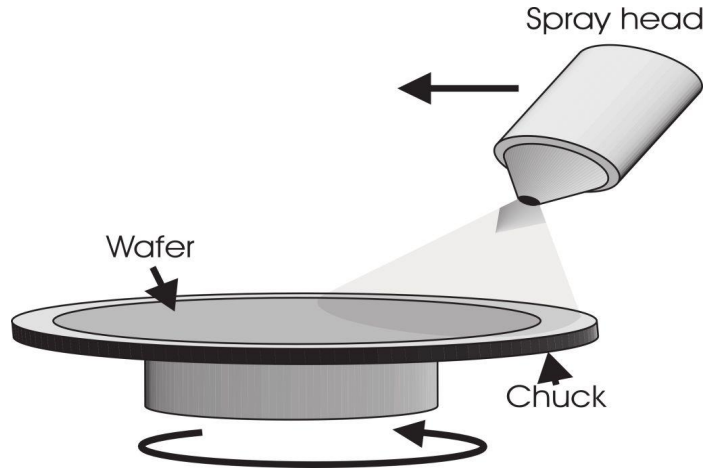


**Figure 32:** A typical spray coating setup (Pham et.al. [83])

However, for the spray coating of PDMS on PAA, a slightly modified approach is adopted. The mixture for spray coating is prepared by mixing PDMS-184 (already

mixed with the curing agent in the ratio of 10:1) with hexane (Fisher Scientific) to form a 5% (by weight) mixture. The PAA mold is mounted on a glass slide and placed on a stationary chuck. The mixture is then spray coated using the spray coating parameters given in Table 7, holding the brush **normal** to the substrate. In all, three spray coating cycles are used to get a conformal coat of PDMS, each cycle consisting of two horizontal runs with the spray coating brush (Paasche Airbrush Co.) held at a distance of 6" from the substrate, with the sample rotated by  $90^0$ , once in between runs. At the end of each cycle (or double coat), the sample is baked on a  $70^0\text{C}$  hotplate for 1 minute. Thus, the PAA mold sees a total of 6 horizontal runs or coats (3 cycles x 2 coats per cycle). It is estimated by interferometry (Wyko profilometer, Veeco Instruments) that the deposited PDMS thickness is approximately  $2\text{ }\mu\text{m}$  per cycle. Hence, the total thickness of spray coated PDMS on the PAA mold is estimated to be about  $6\text{ }\mu\text{m}$ .

**Table 7:** PDMS spray coating parameters

Pressure	Height	Flow rate	Soft bake temp.
1.5 bar	$\sim 6\text{ in}$	13 ml/min	$70^0\text{C}$

Figure 33 are SEM pictures of the PDMS coating profile for 2 different coating cycles. It can be seen that for 3 coating cycles (Figures 33(a) and 33(b)), the coating is quite conformal, but for 5 coating cycles (Figure 33(c)), the side wall coating becomes too thick.

From the SEM pictures, it is clear that using 5 coating cycles could potentially change the final structural profile of the PDMS 186 devices. Thus, 3 coating cycles are used while spraying the PDMS-hexane mixture.

Once the PAA is conformally coated with PDMS, metal thin film is deposited as before. The patterning of the metal using the microtransfer printing process proves to be much easier with the metal deposited on the low surface energy coating. Figures

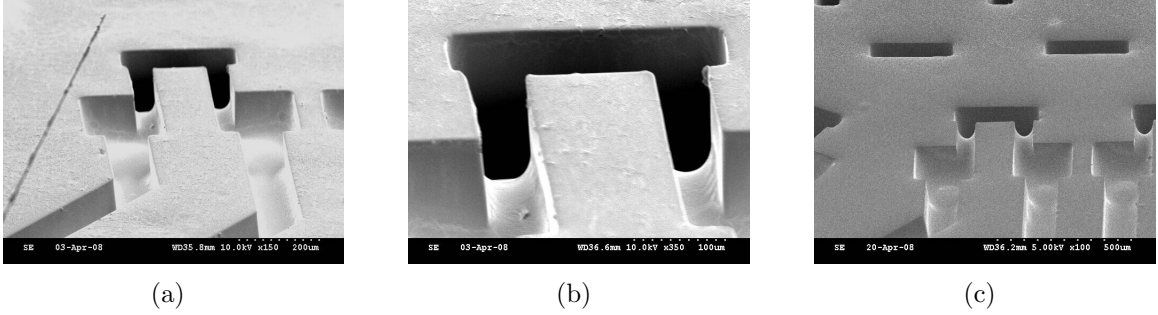


**Figure 33:** Spray coating of PDMS on PAA molds. Figures (a) and (b) are for 3 spray coating cycles, while Figure (c) is for 5

34 show the PAA mold after microtransfer printing.

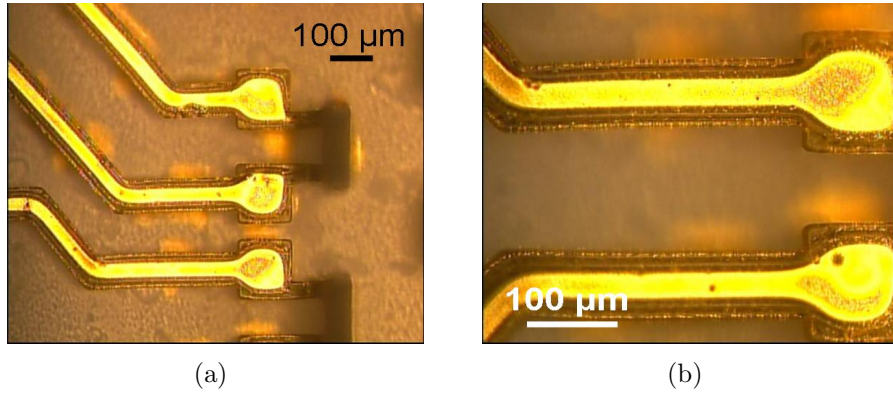


**Figure 34:** PAA molds with spray coated PDMS after microtransfer printing

The photomicrographs indicate that the metal is not warped or cracked in any way, a phenomenon which is commonly observed when using PDMS molds. But, the process needs to be optimized to improve the quality of metal further.

#### 5.3.2.3 Dissolving the PAA mold

After spray coating of PDMS on PAA and subsequent metal deposition and patterning, PDMS 186 is cast into the mold and cured. The PAA mold is then dissolved in water at about 50°C. Although the time for dissolution is very short (about 30 mins to 1 hour), the sample is kept in water for about 4-5 hours to ensure complete dissolution of the PAA, as any residue remaining could affect the mechanical properties

of the elastomer. The sample is then dried at about 50°C for a period of 3-4 hours to evaporate all the water.

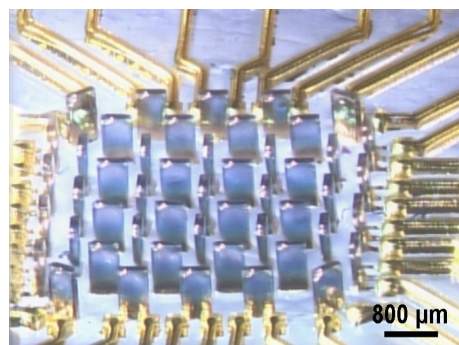
On completion of the process, the metal transfers to the PDMS. Figures 35(a),35(b) are photomicrographs of the final PDMS 186 device, while Figures 35(c),35(d) and 35(e) are the photomicrographs of PU (Smooth-Cast 310) devices, showing the applicability of the process to other materials as well.

Again, as with the PMMA dissolving molds, the final devices show excellent metal film quality with no damage to the structures.

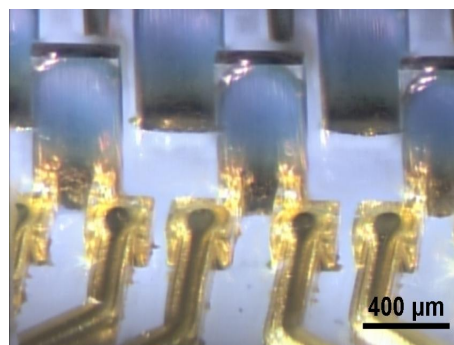
#### ***5.4 Testing: Static deflection and Wind tunnel***

The devices tested are those fabricated by the PMMA dissolving mold technique with PDMS 186. Before the devices can be tested, they have to be interconnected to an external printed circuit board (PCB). Conventional techniques such as wire bonding, flip-chip bonding or tape automated bonding cannot be used here, because of the elastomeric nature of the device. The interconnection scheme used for devices fabricated using conventional MTM was found to be extremely unstable, giving rise to very high contact resistances. This, along with the microcracking phenomena observed, can be used to explain the large differences in resistance of devices fabricated using MTM and the dissolving mold process (see Figures 21 (MTM), 37 (dissolving mold)). Thus, a different interconnection scheme is used here that is more stable and robust.

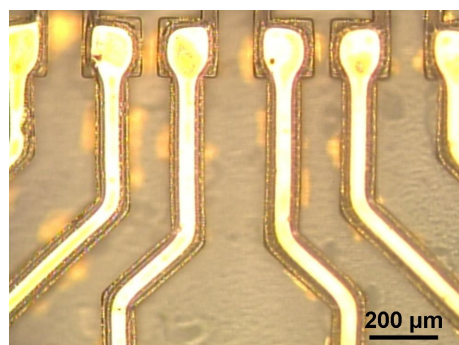
Firstly, the PCB is made by patterning the necessary features (electrodes and bond pads for soldering) onto a Copper/FR4 board, using a *inkjet printer toner transfer* technique. The technique is described in detail elsewhere [39]. Then the PDMS “chip” is placed on the board and glued down with quick set epoxy on all four sides. Conductive silver ink (Ekote Inc.) is then used to “draw” conductive lines joining the bond pads on the chip to corresponding pads on the PCB, as shown in



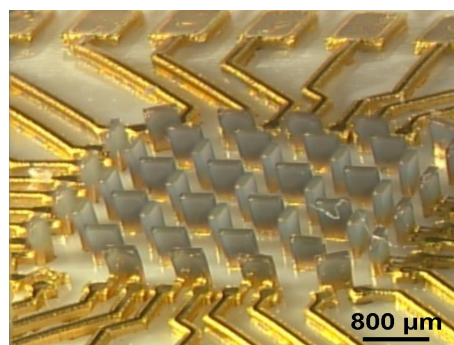
(a)



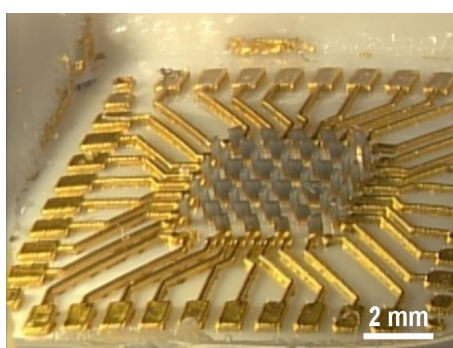
(b)



(c)



(d)



(e)

**Figure 35:** Final PDMS (Figures 35(a),35(b)) and PU (Figures 35(c),35(d),35(e)) devices after dissolving the PAA mold. The figures show good metal film quality and no structural damage



Figure 36. After the solvent in the ink dries off, quick set epoxy is used to encapsulate the connections. The bond pads on the PCB are then soldered onto, to complete the electrical connections and ready the device for testing.

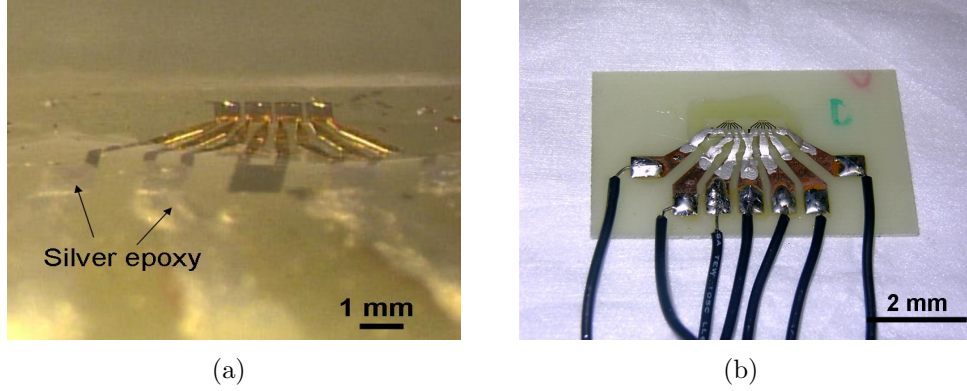


**Figure 36:** Interconnection scheme used to connect the chip to the PCB

The first tests to be conducted on the device are deflection tests using the probe station, similar to tests done with devices fabricated using MTM. A four point measurement is used to sense the change in output on applying a constant deflection of  $8.75 \mu\text{m}$  using a current of 4mA. The deflection is approximately estimated by capturing the movement of the pillar using the video camera attached to the probe station. The pillar width ( $70 \mu\text{m}$ ) is used as a reference to estimate the deflection. The change is then translated into a change of resistance as shown in Figure 37. The change of resistance gradually changes over the number of cycles, finally steadying at about  $10 \text{ m}\Omega$  at the end of 6 cycles. There is also a drift in the initial baseline resistance after deflection of the pillars, which also reduces with the number of cycles.

The next set of experiments are performed in a bench top wind tunnel (ST 180, Scantek 2000). The mean free stream velocity in the wind tunnel is measured using a *thermal anemometer* (Omega FMA-605-I) with a range of 0-5000 SFPM (0-25 m/s), operating between 4-20 mA, placed at a distance of about 6-7 inches from the floor of the wind tunnel. The fully packaged device is placed at a distance of about 3-4 inches from the floor of the wind tunnel. Data from both, the thermal flow sensor,



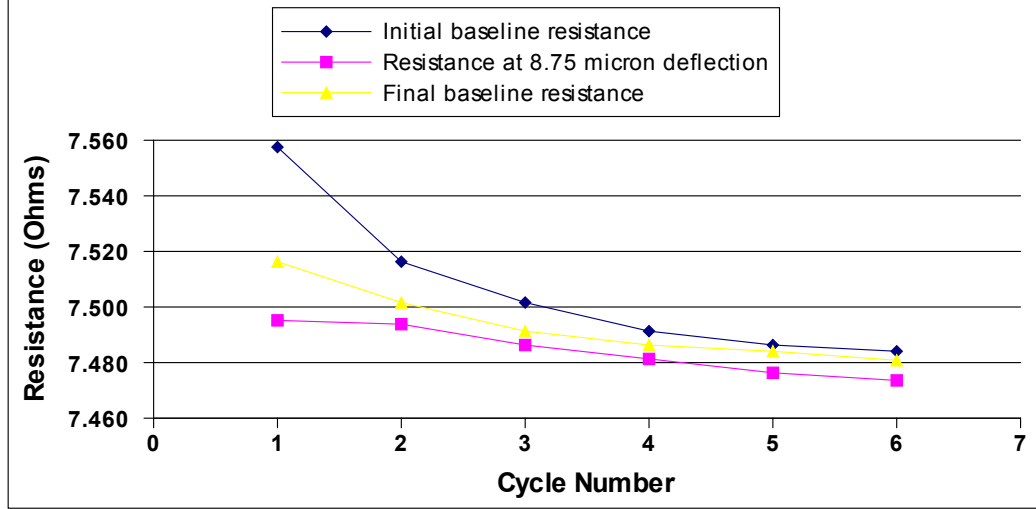


**Figure 37:** Static deflection tests with devices made using the dissolving mold process with PMMA molds

which is used as a reference sensor, as well as the device are recorded using a digital multimeter (Keithley 196 system DMM) and a data acquisition software (HP VEE).

Figure 38 is a screenshot of the data acquisition software used.

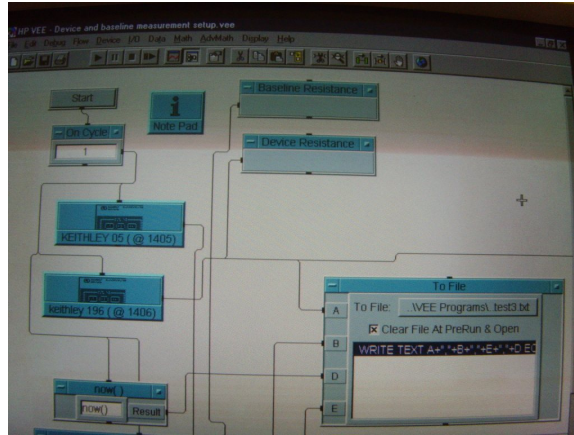


**Figure 38:** Screen shot of the HP-VEE data acquisition software used

Figure 39 shows the complete experimental setup used for the testing.

The main objective of the experiment is to detect the response of the fabricated sensor to a change in the external wind flow. The sensing element itself (the pillar and the piezoresistive thin film at its base) is *loaded in compression* as shown in Figure 40. The resistance of the device is directly tracked with time. Figure 41(a) shows the

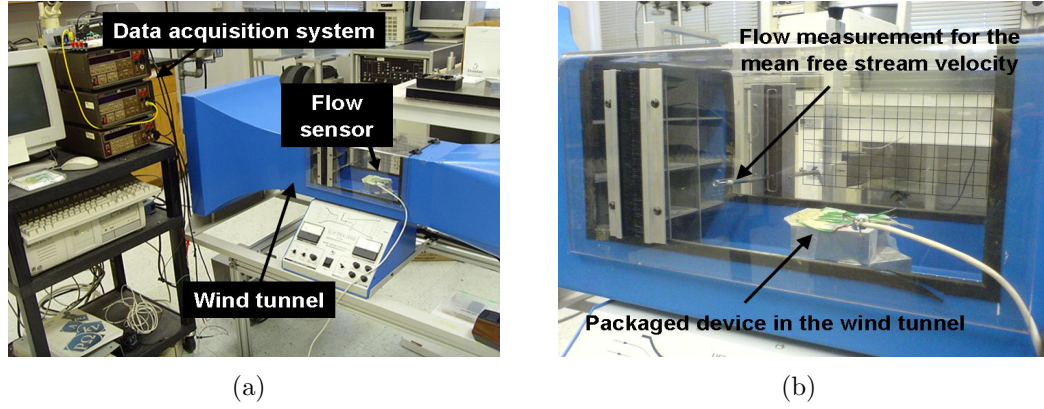


**Figure 39:** Wind tunnel experiment setup

result of the first experiment, where the velocity in the wind tunnel is increased from 0 to its maximum value and then immediately to a lower value (at this point a thermal flow sensor was not available to track the actual wind velocities). From the graph, the change in resistance corresponding to the maximum change in velocity (0-11 m/s) in the wind tunnel is approximately  $10.5 \text{ m}\Omega$ , which gives a device sensitivity of  $0.95 \text{ m}\Omega/\text{m/s}$ . Figure 41(b) shows a second experiment on the same device, showing a different response this time. The behavior of the device will be discussed in greater detail in the analysis section.

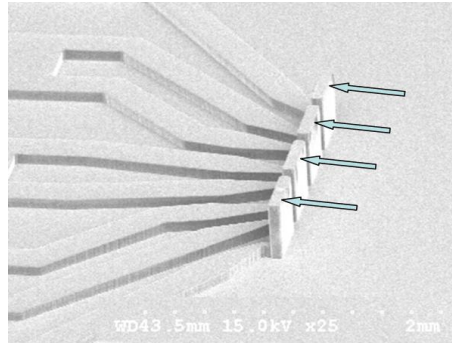
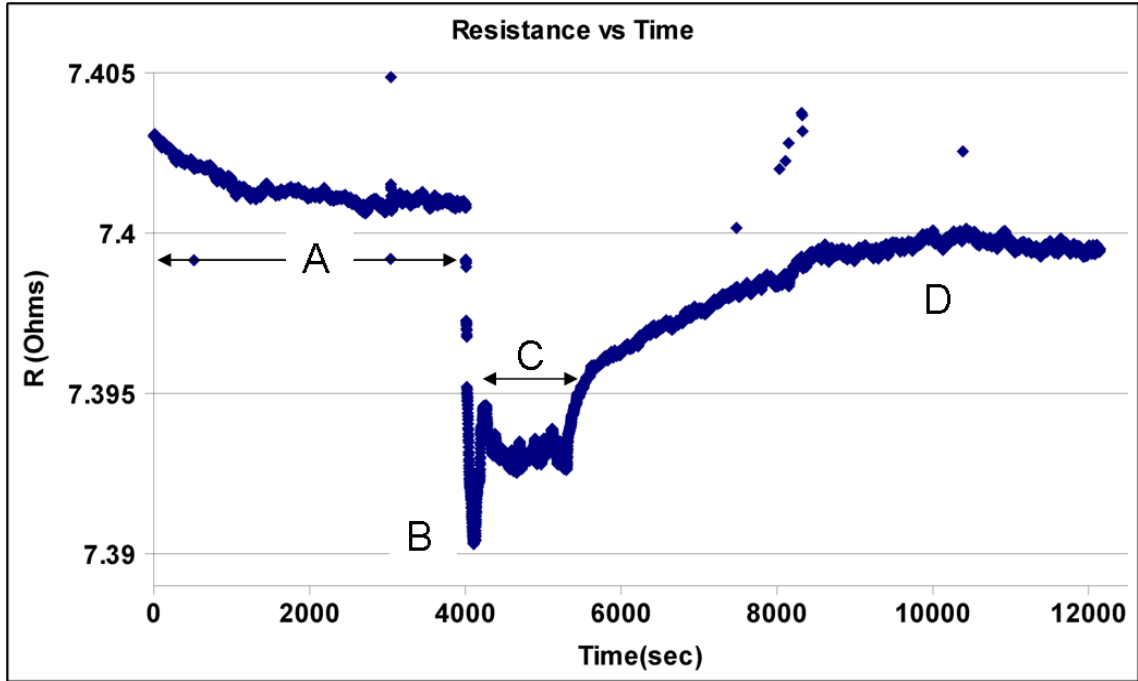
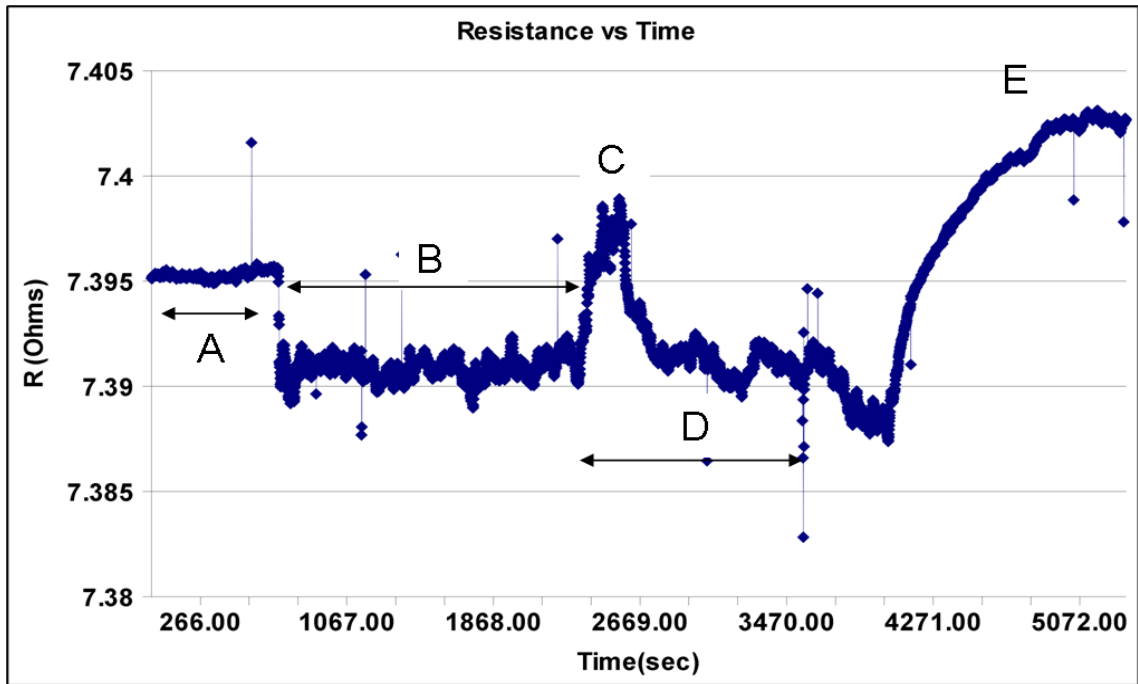


**Figure 40:** Direction of load for static as well wind tunnel tests

The experiment is also conducted on a different device, part of a separate batch of devices fabricated. This time, the wind velocity is also tracked as a function of time. Figure 42(a) shows a plot of the wind velocity profile and Figure 42(b) is the

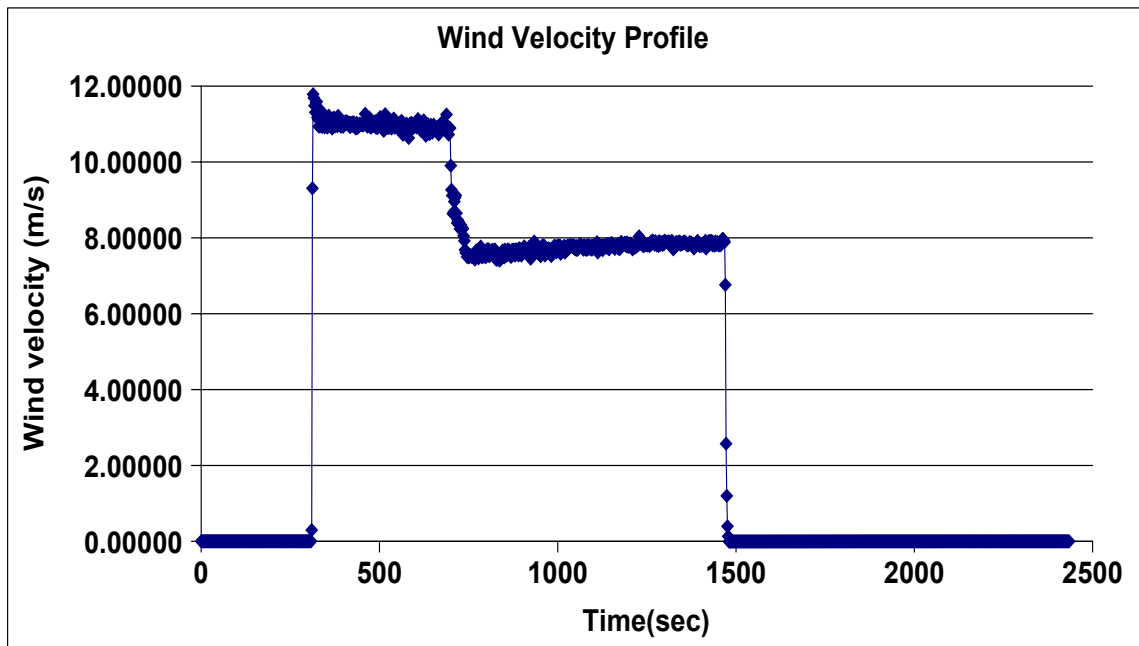


(a) Experiment # 1

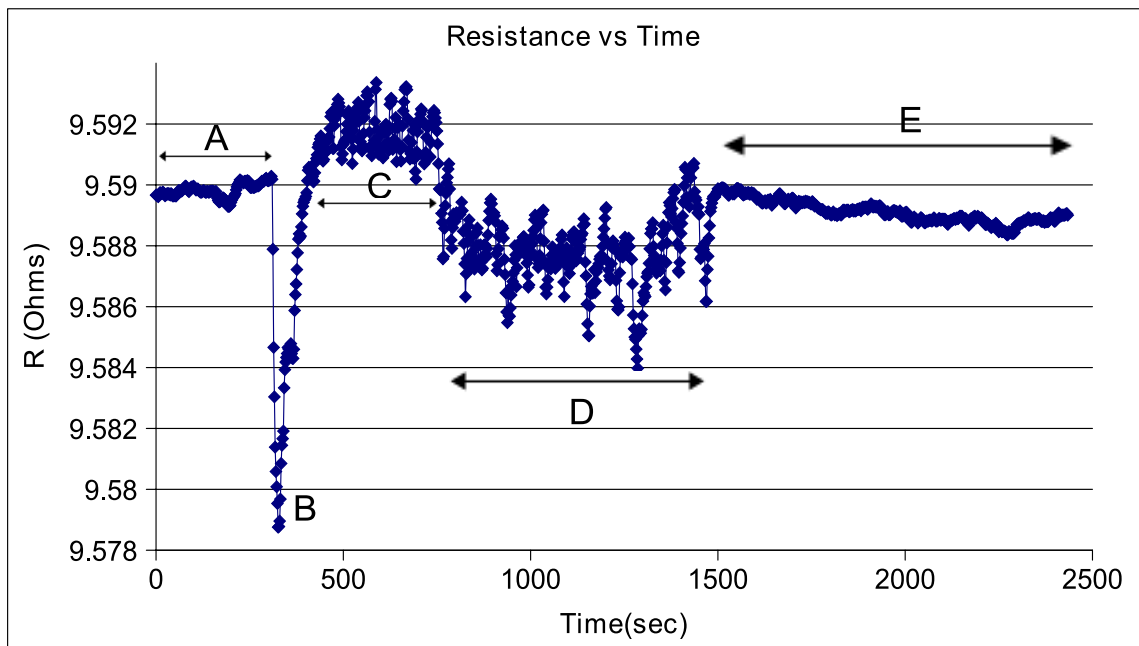


(b) Experiment # 2

**Figure 41:** Wind Tunnel testing of devices fabricated by the dissolving mold process. Both experiments are conducted on the *same* sample



(a) Wind velocity profile measured by the reference sensor



(b) Corresponding resistance profile of the device measured by the digital multimeter

**Figure 42:** Wind Tunnel testing - experiment # 3

**Table 8:** Device response “zones” - Experiments # 1 and 2

	Zone	Wind velocity profile	Device response
<b>Expt. #1</b>	A	0 wind velocity	stable resistance
	B	maximum velocity	decrease in R
	C	velocity $\sim 75\%$ of maximum	slight increase in R
	D	0 wind velocity	further increase in R
<b>Expt. #2</b>	A	0 wind velocity	stable resistance
	B	velocity close to $\sim 50\%$	decrease in R
	C	maximum velocity	increase in R
	D	velocity close to $\sim 50\%$	decrease in R
	E	0 wind velocity	increase in R

**Table 9:** Device response “zones” - Experiment # 3

	Zone	Wind velocity profile	Device response
<b>Expt. #3</b>	A	0 wind velocity	stable resistance
	B	maximum velocity - 11 m/s	decrease in R
	C	maximum velocity - 11 m/s	unexpected increase in R
	D	velocity - 7.5 m/s	decrease in R
	E	0 wind velocity	increase in R

corresponding device response.

A first glance at all the device responses recorded from the various experiments, reveals that the gold thin film piezoresistor at the base of the pillars is behaving as expected, showing a reduction in resistance due to a compressive stress acting on it. The devices are loaded such that the side with the electrodes is always under compression, so that they do not interfere with the flow (as shown in Figure 40). Gold has a positive piezoresistive gage factor of about 2, indicating that a decrease in resistance is expected, when loaded under compression.

In the very first experiment shown in Figure 37, an approximate change of  $10 \text{ m}\Omega$  is observed for a deflection of  $8.75 \text{ }\mu\text{m}$ , but the response also shows hysteresis of the baseline or starting resistance with an average value of about  $13 \text{ m}\Omega$ . For “fresh” devices, that have never been tested before, there is a strong dependence of *cycling* on the response, with a steady value being reached only after a certain number of

cycles (about 6-7 cycles in this case). The resistance at the end of the *static deflection experiment* is  $7.48 \Omega$ .

The *wind tunnel experiment* is performed *on the same device* and the baseline value before the start of the experiment is  $7.40 \Omega$ . The maximum change of resistance observed for Experiment #1 (Figure 41(a)) is about  $9.74 \text{ m}\Omega$ , while the baseline resistance between has drifted by  $78 \text{ m}\Omega$  in the period between the static deflection experiments and the wind tunnel experiment, which is far greater than the response of the device to wind flow. From Table 8, in Zone B, the device resistance immediately drops to its *minimum* value ( $7.39 \Omega$ ), when the wind tunnel velocity reaches its *maximum* velocity. On reducing the velocity to about  $8.25 \text{ m/s}$  in Zone C, the resistance increases to about  $7.39 \Omega$ , a change of  $2.70 \text{ m}\Omega$ . This increase is expected since, the compressive stresses and strains decrease with decreasing velocity. In Zone D, the wind tunnel is switched off and the the resistance starts rising again, but the device resistance takes about 1:30 hours to stabilize at a value of about  $7.39 \Omega$ , yielding an approximate hysteresis of  $4 \text{ m}\Omega$ .

In Experiment #2 (Figure 41(b)), which involves the same device again as the above two experiments, the behavior is somewhat different. In zones A and B, the device response is as expected but with different values of change in resistance for the same difference in wind velocities. The change in resistance for a maximum change in wind velocity is  $6.13 \text{ m}\Omega$ , as compared to  $9.74 \Omega$  in Experiment #1. A dramatic anomaly appears in Zone C, where the velocity is increased from an intermediate value to the maximum value, and the resistance instead of decreasing, increases to a value which is even higher than the baseline at the beginning of the experiment. But, in Zone D, when the velocity is again decreased to its previous value in Zone B, the resistance also decreases to its value in Zone B. In Zone E, the wind tunnel is switched off and the device resistance starts increasing, but it takes about 21 minutes for the value to stabilize at  $7.40 \Omega$ , yielding a hysteresis of about  $8 \text{ m}\Omega$ .

Experiment #3 (Figure 42(b)) shows similar behavior to the above experiments. It must be remembered that this experiment is performed on a completely different device, belonging to a different batch. The resistance profile does match the wind velocity profile, but there is an unexpected rise in the resistance in Zone B. The maximum change in resistance is about 10 m $\Omega$ . The baseline resistance hysteresis is 0.17 m $\Omega$  and also the time taken for the resistance to stabilize after switching the wind tunnel off is much shorter.

The results of all three experiments are summarized in Table 10.

**Table 10:** Summary of device performance.  $R_i$  is the resistance at the start of the expt.,  $R_m$  is the maximum change in resistance,  $R_h$  is the baseline resistance hysteresis before and after the experiment,  $T_s$  is the time taken for the resistance to stabilize after turning the wind tunnel off

Experiment #	$R_i(\Omega)$	$R_m$ (m $\Omega$ )	$R_h$ (m $\Omega$ )	$T_s$ (mins)
<b>1</b>	7.40	9.74	4	90
<b>2</b>	7.40	6.13	8	21
<b>3</b>	9.59	10	0.17	2-3

The hysteresis behavior coupled with the lack of repeatability of results makes prediction of a device failure mechanism very difficult. In terms of the final application, such devices are not suitable because of the above complications combined with the a low *device sensitivity* (less than 1 m $\Omega$ /m/s). Moreover, the device response in some cases is of the same magnitude as the order of fluctuations in the absence of any wind flow, giving an extremely low signal to noise ratio. In the next section, some of the failure mechanisms are briefly investigated and discussed.

## ***5.5 Analysis of performance of MTM and dissolving mold process based devices-Failure modes***

### **5.5.1 Low sensitivity**

One of the disadvantages of both MTM as well the dissolving mold process is the fact that it is near impossible to pattern the metal on the side walls. Side wall deposition

of the metal is a mere coincidence. This possibly has a severe impact on the sensitivity of the device. A circuit diagram of the sensing elements (pillar with metal on the side walls) is shown in Figure 43.

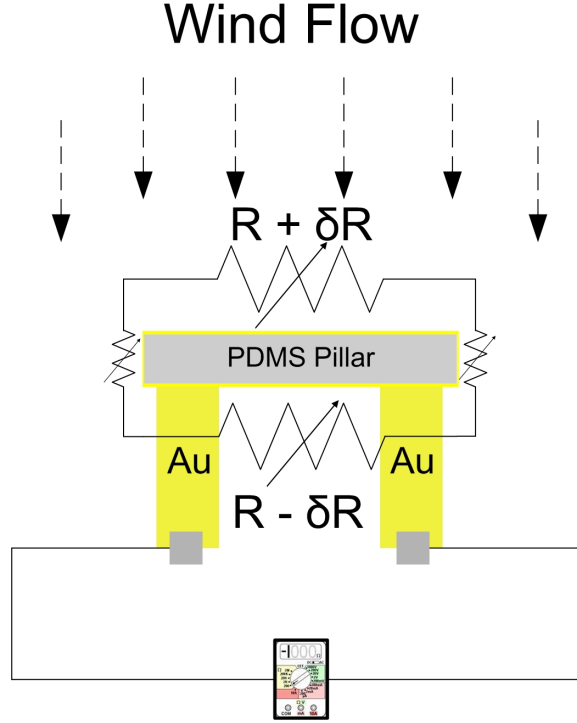


**Figure 43:** Circuit diagram of the device sensing element

As can be seen from the figure, there is a thin film of gold (of approximately equal thickness) on ALL four sides of the pillar. It can be assumed that the overall device resistance can be modeled as 2 equal resistors in parallel. Assuming that, on deflection in the wind tunnel, equal and opposite strains are produced along both major side walls, which in turn translates into a equal but *opposite* change in resistance. Thus, the net change in resistance of the device or response is given by the following equations (10).

$$R_{device} = \frac{(R + \delta R)(R - \delta R)}{2R} = \frac{((R^2 - (\delta R)^2))}{2R} = \frac{R}{2} \quad (10)$$

Now, this is the same as the initial resistance of the device, giving a change in



resistance of 0. This could possibly explain the low device response. The fact that a small change is observed may indicate that the 2 resistors differ by a small value. One of the other reasons that may explain the low sensitivity is obtained by a rigidity analysis of the structures. A high mechanical rigidity of the structures due to the geometry (the pillars are about 70-80  $\mu\text{m}$  thick) can also be responsible for a low device response. But, this problem is very difficult to overcome while using molding as the fabrication scheme, since it would lead to damage to the PDMS pillars, due to its low tear strength. But the differing metal quality from device to device is considered to be a major reason for the irreproducibility of results. This is discussed in more detail in the following section.

The choice of the piezoresistor is also critical in deciding the sensitivity. Most metals have a gage factor between 2-3, with Au having a value of 2, as compared to doped silicon, which has a gage factor of about 160. Thus, this low value of the gage factor could also be responsible for the low sensitivity and device output.

### **5.5.2 Effect of thin film metal quality on device performance**

Microcracking effects were first discussed in Chapter 4 and these were clearly observed in devices fabricated using the modified MTM process, as shown in Figure 22(a). These have a strong role to play in dictating the device performance. As reported by Lacour et.al. [59], these microcracks formed are strain dependent and thus would change with changing strain. It is thus quite possible, that the changing nature of these microcracks makes the device response change with time, resulting in the irreproducibility of the results. Even in devices fabricated using the dissolving mold process, *although microcracks are essentially absent, there is a warpage of the metal observed* on the elastomeric substrate. Figure 44 shows the comparison between the metal directly deposited on elastomeric substrates by evaporation and metal on PDMS fabricated by the dissolving mold technique. Both show warpage of the metal

film.

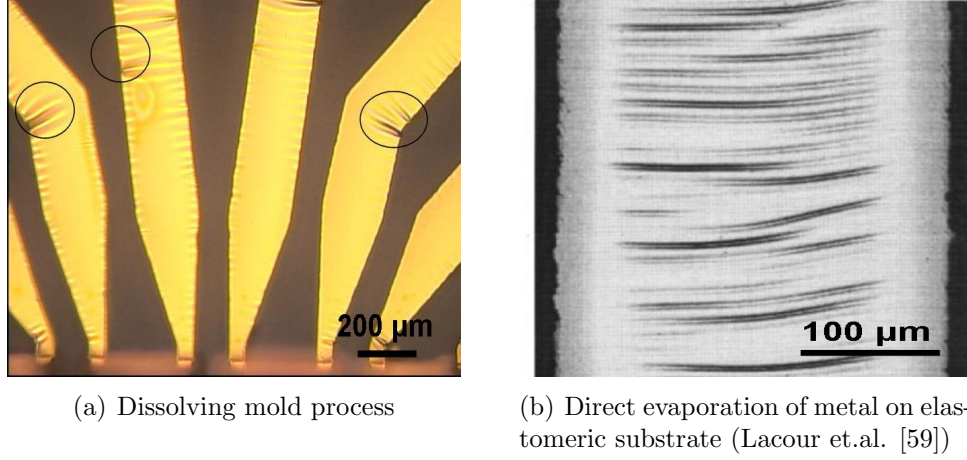


**Figure 44:** Warpage observed in thin metal films (Au) on elastomeric substrate

These warps or *wave patterns* have been reported widely [49, 54, 58, 59, 66]. For most of the cases reported, these waves or buckles are formed as a result of built-in strain and a strain due to a CTE mismatch between the Au and the PDMS. However, these reports do not compare the resistance of the film under loading and unloading conditions, which could reveal important information about hysteresis. Moreover, these also do not discuss the effect of cyclic loading and unloading on the properties of the film and its subsequent effect on the resistance. Such an investigation could possibly explain the performance of the devices reported here.

Overall, it is clear that the MTM process is unsuitable for fabrication of devices for applications requiring metal thin films on elastomeric substrates, since microcracking effectively reduces the device yield to zero. For devices that are electrically functional, the resistance is much higher than the theoretical resistance ( $\sim 107 \Omega$  observed resistance). In such a regime, the device resistance is now given by Equation 11 [57]

$$R_{device} = R_{metal} + R_{gaps} \quad (11)$$

It is supposed that  $R_{gaps}$  would dominate the device resistance and due to changing

strains, would be irreproducible. Even for a device fabricated using the dissolving mold process, handling of the device during interconnections, packaging etc., would lead to the same problems as with MTM, since metal on elastomer is highly susceptible to cracking/warpage, as shown in Figure 45.

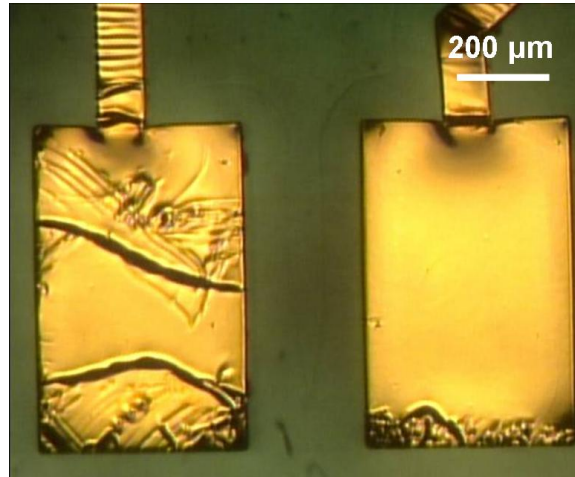


**Figure 45:** Bond pads of devices fabricated by the dissolving mold process. The pad on the left has been probed, while the pad on the right is untouched

Finally, a possible explanation for the hysteresis observed in some devices is the viscoelastic nature of all elastomers that causes a time-dependent strain. When the external force (either a point force applied by the probe tip or deformation caused by air flow in a wind tunnel) is switched off, the PDMS pillar continues to undergo marginal deformation and there is a relaxation period associated with it, which prevents the corresponding device resistance from immediately falling to zero. As explained before, the *relaxation* behavior of the *waves* formed on the metal film may not be a reversible phenomena, which could also be causing the hysteresis. But, a thorough investigation is not conducted in this research.

Overall, although both MTM as well as the dissolving mold process have shown excellent promise in the fabrication of flow sensors, there are technical issues that are inherent to the materials involved in the processes that affects both, the device yield, as well as the performance. Nevertheless, the dissolving mold process is a marked

improvement over the MTM process, as is evident from the metal film quality and the values of the initial baseline resistance ( $\sim 7\text{-}9\ \Omega$  vs  $\sim 105\text{-}107\ \Omega$  for MTM). For the current application, elastomers are ideal materials because of the large strains produced for a given deformation, compared to much stiffer materials like silicon or SU-8. But, electrical functionality on elastomeric materials becomes a major challenge. Thus, the choice of material is of utmost importance in deciding the performance and robustness of the final device. Chapter 6 discusses the final fabrication technique developed which completely eliminates the need for depositing thin metal films on PDMS, without compromising on the use of an elastomeric material for the sensing piezoresistor.

## CHAPTER VI

### LASER MICROFABRICATION AND CONDUCTIVE ELASTOMER COMPOSITES

Micromolding based techniques have been investigated for the fabrication of an all elastomer flow sensor. A modified metal transfer micromolding (MTM) and a dissolving mold MTM process have been developed and devices fabricated and tested. However, it was established that elastomeric devices with metal thin film resistors have an inherent flaw due to damage to the thin metal film during interconnections, testing and general handling. Moreover, the lack of any control over the piezoresistor pattern on the sidewalls of the structures, makes these fabrication schemes non-ideal for the current application.

Laser microfabrication in MEMS is briefly introduced here and conductive elastomers was already introduced in Section 2.1.3. This chapter introduces a new fabrication sequence which uses a combination of CO<sub>2</sub> and Excimer laser machining to fabricate *microtufts* that undergo displacement when placed in a wind tunnel. The displacements in turn are sensed by electrically conductive composite elastomers, which are inherently piezoresistive. The use of a composite conducting polymer eliminates the issue of microcracking observed when using MTM and the dissolving mold process-a major hurdle in device fabrication. An added advantage of using these composites is a much higher piezoresistive gage factor ( $GF \sim 7$ ) as compared to metal thin films ( $GF \sim 1-2$ ). This in turn translates into more robust devices with very high sensitivities.

The ability to process a wide range of materials and to produce truly three dimensional structures with tolerances in the micron to sub-micron levels, gives laser

micromachining some key advantages over other existing microfabrication techniques in MEMS [45]. The following are some of the major applications of lasers in MEMS:

1. Laser micromachining for direct fabrication of devices
2. Laser fabrication of polymer master structures for subsequent replication (Laser-LIGA)
3. Laser assisted deposition and etching
4. Laser-assisted manipulation and assembly of microparts

Of the applications shown above, *bulk micromachining* of polymers or direct fabrication is of utmost importance in MEMS and is what is used in the microfabrication of flow sensors. Schmitz et.al. have demonstrated the use of excimer laser machining in the fabrication of wax molds that can be used for the molding of high aspect ratio structures [90]. Moss et. al. have also used excimer laser machining of polyimides for the fabrication of multilayer polymeric microsystems [76]. Direct fabrication involves the etching of solids by pulsed laser radiation and it relies on the process of ablation [75], which depends on both the material and the laser parameters (wavelength, pulse duration, intensity etc.). In all cases, the absorption of the laser energy at the surface of the solid results in ejection of material from a thin surface layer. Some of the lasers typically used in MEMS micromachining are fluorine (157 nm wavelength), copper vapor (510, 578 nm wavelengths), excimer (ArF, KrF, XeCl, 193 nm, 248 nm, 308 nm wavelength respectively) and CO<sub>2</sub> (10  $\mu$ m wavelength) etc. Thus lasers span a wide spectrum of length scales of micromachining [45].

The following sections detail the device principles, characterization of the mechanical and electrical properties of the material and fabrication schemes for a microcantilever based flow sensor - a *microtuft*, as well the testing of the final devices fabricated using this technique.

Micro-cantilever based sensors have been widely reported [18, 71, 96, 103] for a variety of applications including humidity and flow sensing. These microcantilevers are usually fabricated by the bulk micromachining of silicon and are either silicon based microcantilevers [18] or silicon nitride based [103]. In fact, for most microcantilever based sensors, the range of materials is limited to Si, SiO<sub>2</sub> or Si<sub>3</sub>N<sub>4</sub>, leading to high costs and complicated fabrication processes.

Polymeric cantilevers have also been studied, but less extensively. Almost all polymeric microcantilevers are fabricated exclusively for bio-sensing applications and typically fabricated using SU-8, because of the ease of fabrication [2, 17]. Microcantilevers based on other polymeric materials like polystyrene have also been fabricated using injection molding techniques [74]. Laser fabrication of microcantilever structures have also been reported, using both polymeric materials [110] (polyethylene terephthalate (PET)) and metals [43], by using the Laser-LIGA process.

Conductive composite elastomers are also widely reported for a variety of applications. It has been used as a piezoresistor for flow sensing applications, but not that extensively. Section 2.1.3 talks about the applications of filled polymer composites in more detail, with emphasis on its piezoresistive properties.

## ***6.1 Device design and sensing principle***

The sensing principle used for the microtuft is quite similar to the one described in Section 3.2.1.

The microtuft itself is fabricated using an ultra-thin film of Kapton<sup>®</sup> (7.62 microns, Kapton<sup>®</sup> 30 HN, Dupont), a polyimide that is introduced in detail in Section 6.2.1. The sensing element is a conductive carbon-black elastomer with a high piezoresistive gage factor ( $\sim 7$ ), as is shown in Section 6.2.2. When air flows across the microtufts, it causes deformation of the beam structure and this in turn induces a strain in the piezoresistor causing a change in its resistance. The resistance can be

calibrated with the external wind flow.

Figure 46 shows the sensing principle.

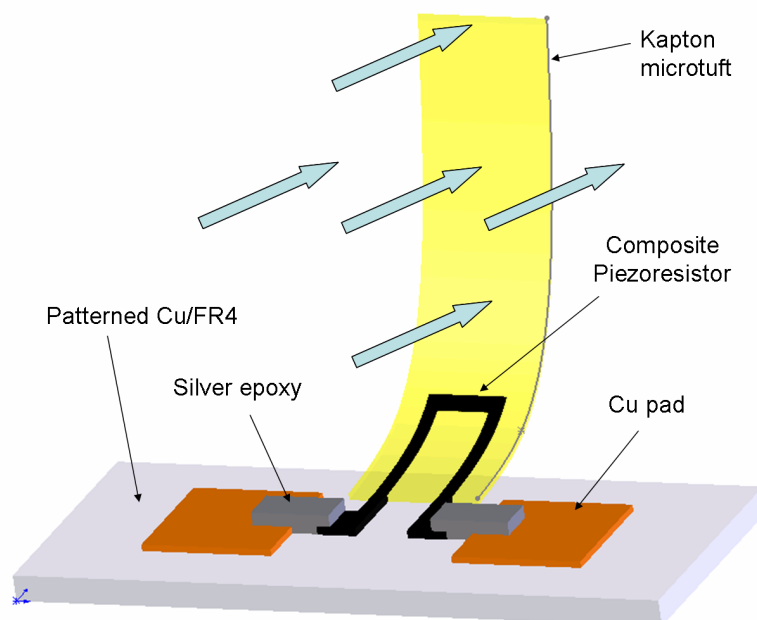


**Figure 46:** Sensing principle for the microtuff based flow sensor

## 6.2 Materials

### 6.2.1 Kapton®

The microtuff is entirely based on Kapton®, a polyimide film developed by Dupont. Kapton® polyimide film possesses a unique combination of properties that make it an ideal choice for this and many other applications. The ability of Kapton® to maintain its excellent physical and mechanical properties over a wide range of temperatures makes it an ideal choice.

Kapton® is synthesized by polymerizing an aromatic dianhydride and an aromatic diamine. It has excellent chemical and solvent resistance, and thus used widely as substrates for fabrication of flexible MEMS sensors, which include electrode arrays for recording surface potentials [44], flexible shear stress sensors [51], RF MEMS switches [88] etc. Laser micromachining of Kapton® has also been used for the



fabrication of multilayer polymeric microsystems [76], hollow microneedles [25] and polymer microfluidic devices [55].

A summary of the essential mechanical properties of Kapton<sup>®</sup> are shown in Table 11.

**Table 11:** Physical properties of Kapton films (data obtained from Dupont)

Physical Property	Typical Value at 23 <sup>0</sup> C
Tensile Modulus (GPa)	2.5
Poisson's ratio	0.34
Ultimate tensile strength (MPa)	231
Ultimate elongation (%)	72
Density (g/cc)	1.42

### 6.2.2 Carbon black-elastomer composite - characterization of the material properties

The carbon black elastomer composite is used as the sensing piezoresistor for the flow sensing application. It was already explained in Section 2.1.3, how electrically conducting composite polymers can be used as piezoresistors. The composite used in the process is commercially available from Wacker Chemie AG under the trade name Elastosil<sup>®</sup> LR3162. It is a silicone based elastomer loaded with carbon black particles, with a reported volume resistivity of 9  $\Omega$ -cm. Minimal details of the materials properties itself are provided in the material data sheets, which are summarized in Table 12.

This material combines two extremely critical properties that are required for the application-

- Low value of Young's modulus. It is a soft elastomeric material and hence will experience high values of strain for a given stress.
- Electrical conductivity. This ensures that thin metal films are not required as piezoresistors as in the case of MTM and the dissolving mold process described

**Table 12:** Properties of Elastosil<sup>®</sup> LR3162 (measured on sheets that are vulcanized for 5 min at 165<sup>o</sup>C)[8]

Property	Units	Typical Value
Appearance	-	Black
Specific gravity	g/cm <sup>3</sup>	1.12
Viscosity	mPa-s	7,000,000
Tensile strength	%	5.2
Elongation at break	N/mm <sup>2</sup>	440
Tear resistance	N/mm	12
<b>Volume resistivity</b>	$\Omega$ -cm	9

in Sections 4, 5. This solves the issues that are encountered with microcracking of thin metal films.

The material properties that are associated with each of the above characteristics are not provided by Wacker. More importantly, the piezoresistive gage factor of the material is unknown. Thus, in this section, the Young's modulus of the material as well as its piezoresistive gage factor are characterized.

#### 6.2.2.1 Characterization of Young's modulus

The characterization of the mechanical properties of the conductive composite elastomer (Young's modulus) is done using an Instron (Instron Engineering Corporation) material testing machine.

In order to prepare samples for the tensile testing, a stencil mask is patterned out of 0.5 mil thick Kapton<sup>®</sup>, using the CO<sub>2</sub> laser (Gravograph Newhermes), in the form of a rectangular strip of 5mm width. The stencil is then adhered onto a 5 mil thick sheet of FEP Kapton<sup>®</sup> (FEP is Fluorinated ethylene propylene), using a spray adhesive (3M Corp.). The composite material itself, supplied as a two part system, is mixed in a 1:1 ratio of Part A and Part B and cured at a temperature of about 120-130 <sup>o</sup>C for 2 hours. Although the recommended curing time is not so high, the curing time used here ensures that the material is sufficiently cross-linked and its

mechanical properties are stabilized. The FEP Kapton<sup>®</sup> ensures the easy release of the composite elastomer. The two ends of the 5mm wide strip are then placed on two small pieces of FR4 boards and secured in place using a quick cure 2 part epoxy (Loctite Inc.). The FR4 boards are used to prevent any damage to the sample itself by metal clamps in the Instron tool. Two different samples are made and tested, having unstretched initial lengths of 21 mm and 19 mm respectively.

Once the samples are mounted between the two clamps of the Instron, the tool is programmed to apply a constant strain rate of 0.21 mm/min. A typical stress-strain curve extracted from the load-deflection data obtained from the Instron is shown in Figure 47. The graph indicates that the stress-strain behavior of the composite elastomer is non-linear in nature. The line of best fit has an estimated slope of about 1.88 MPa and it is the approximate Young's modulus of the material. A total of 4 experiments are conducted on the 2 samples made. The results are summarized in Table 13.

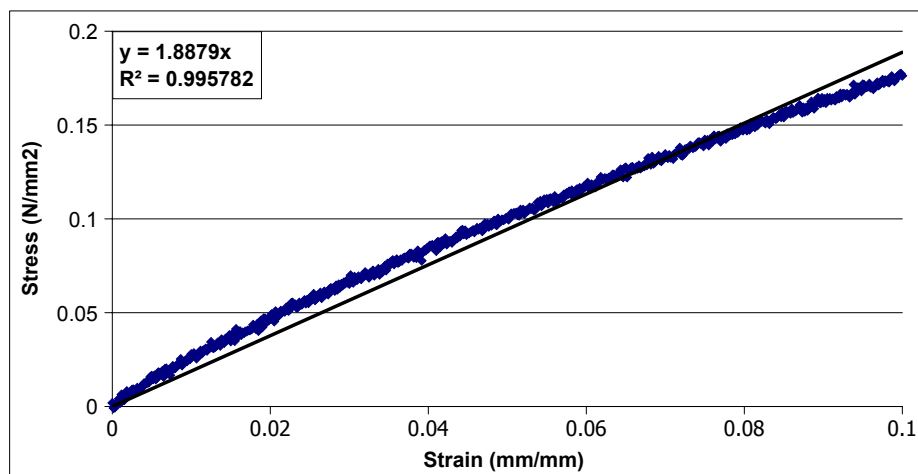


**Figure 47:** Stress-strain curve for a 5mm wide composite elastomer sample. The thickness of the material is about 97  $\mu\text{m}$  and the unstrained length is 21 mm. The applied strain is 10%

The differences in the modulus predicted from the different experiments are attributed to errors in thickness measurements of the samples. Cycling also has a strong effect on the mechanical properties, but it is not investigated in this research. Since

**Table 13:** Young’s Modulus of the composite elastomer extracted from different samples.  $\epsilon$  is the strain and  $E$  is the Young’s modulus.  $L$ ,  $W$ ,  $t$  are the unstrained length, width and thickness of the sample respectively

Expt. #	Sample	Maximum $\epsilon$ (%)	$E$ (MPa)	$R^2$ fit
1	$L=21\text{mm}$ ; $W=5\text{mm}$ $t=97.5\ \mu\text{m}$	10	1.89	0.995
2	$L=21\text{mm}$ ; $W=5\text{mm}$ $t=97.5\ \mu\text{m}$	20	1.49	0.991
3	$L=19\text{mm}$ ; $W=5\text{mm}$ $t=105\ \mu\text{m}$	20	1.77	0.973
4	$L=19\text{mm}$ ; $W=5\text{mm}$ $t=105\ \mu\text{m}$	20	1.76	0.977

the sample in experiment 2 is the same as in experiment 1, the difference in the results could be attributed to cycling of the material. This also applies to the material in experiment 4. The average Young’s modulus predicted by the basic experiments conducted is about 1.72 MPa. This compares well with other popular non-conducting elastomers such as PDMS, which have a reported Young’s modulus of 1-2.5 MPa.

The following section explains the characterization of the electrical properties, particularly the piezoresistive gage factor of the material.

#### 6.2.2.2 Characterization of piezoresistive gage factor

The characterization of the electrical properties of the composite elastomer is much more challenging as compared to the mechanical properties. The electrical conduction mechanism in composite materials (not only elastomers) is not fully understood and complications arise in the characterization due to hysteresis effects during loading and unloading. The large difference in CTE of the carbon black particles and the polymer adds more complexity. In this section, the piezoresistive gage factor of the carbon-black elastomer composite used is characterized. It should be kept in mind that this is a very basic and preliminary experiment that does not take into account factors such as extensive strain cycling and strain rate dependence of the electrical

properties.

The sample making procedure is the same as described in the previous section, except that connection between the material strip and the Cu-FR4 PCB is made using 2 part conductive silver epoxy (Epotek, Ted Pella Inc.). Wires are then soldered onto the PCB to connect the sample to an external resistance measurement unit, which consists of a multimeter (Keithely 196 system DMM) interfaced with a computer that records the resistance real-time, using a data acquisition software (HP-VEE). The setup is quite similar to the one described in Section 5.4. The testing itself is conducted using a *poor man's Instron* - a microscope (Nikon MM-40 microscope) used in conjunction with a multi-axis dimensional measurement instrument (Quadra-Chek 200) connected to the microscope. The sample is taped onto the side of the microscope such that strains in the elastomer can be applied by rotating the z-axis knob. The corresponding elongation of the sample can be measured using the Quadra-Chek 200. The measurement setup is shown in Figure 48.

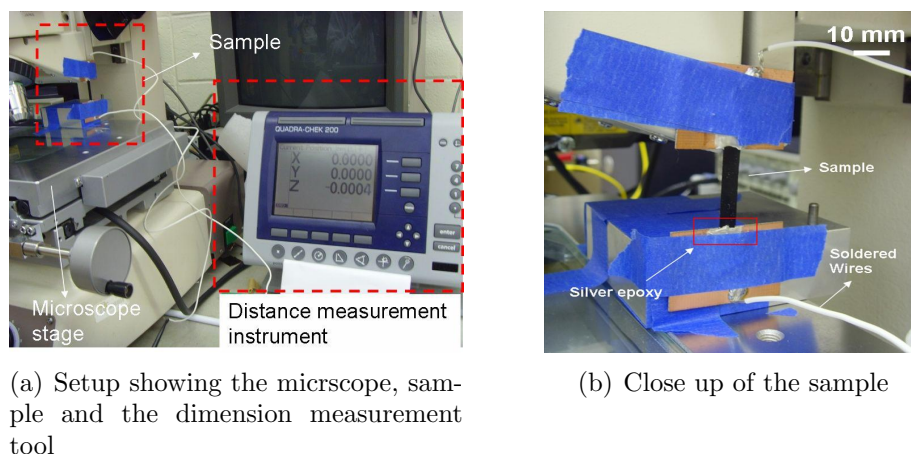
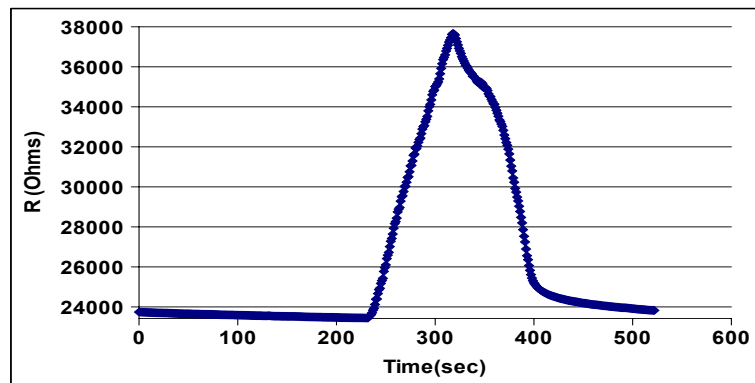


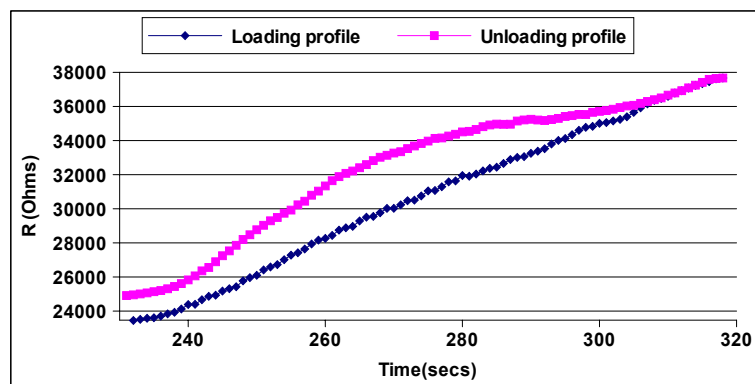
**Figure 48:** The *poor man's Instron* - experimental setup for gage factor characterization

Testing was conducted on a *virgin* sample strip that has never seen strain. The experiment is started by first ensuring that the sample strip was *just taut*. This is estimated by adjusting the x,y and z positions of the sample and checking to see if

there is any significant change recorded by the multimeter. Once the *just taut* position of the sample is determined, data recording is started. Substantial time is allowed for the resistance to stabilize before any strain is applied to the sample. The sample is then continuously strained from 0% to the maximum strain, using the z-focus knob of the microscope. The strain rate is maintained as constant as possible and at a relatively low value. But since the entire procedure is done manually, it is difficult to maintain a constant strain rate. Tests are conducted at 1%, 5% and 10% strains and the corresponding gage factors calculated. A typical tensile test conducted on a 23mm x 5mm x 0.08mm (LxWxt) is shown in Figure 49. Sufficient time is allowed between experiments for the resistance values to stabilize.



(a) Loading and unloading profile 1



(b) Loading and unloading profile 2

**Figure 49:** Resistance vs Time graph for strain loading and unloading with 10% maximum strain in a 23mm length composite elastomer sample. Both loading profiles are one and the same, but represented in different ways to demonstrate the drift of resistance with time and the hysteresis respectively

The gage factor is calculated from the loading profile graph for the elastomer. The gage factor is calculated from Equation 9 as shown below.

$$\frac{\Delta R}{R} = G\epsilon \quad (12)$$

The exact procedure for calculating the gage factor from the tensile testing experiments is as follows:

1. Plot the loading profile of the material starting with 0% strain going upto the maximum strain.
2. Add a linear trendline to the graph and extract the slope. The slope gives the value of the rate of change of resistance  $dR/dt$ .
3. Calculate the average elongation rate by dividing the maximum strain with the time taken to reach the maximum resistance from the initial resistance. This is  $dl/dt$ . The maximum resistance corresponds to the maximum strain.
4. Since gage factor is given by Equation 9, it can be re-written as

$$\frac{\frac{dR}{dt}}{R} = G \frac{\frac{dl}{dt}}{l} \quad (13)$$

$$G(\text{gage factor}) = \frac{\frac{dR}{dt}}{\frac{dl}{dt}} \frac{l}{R} \quad (14)$$

where  $l$  and  $R$  are the unstrained length and initial resistance before strain, respectively.

Figure 50 shows the plot of the loading profile for the sample. The fitted trendline has a slope of  $172.93 \text{ } \Omega/\text{s}$ . The average elongation rate is  $0.027 \text{ mm/s}$ . With an initial unstrained length of  $23\text{mm}$  and resistance of  $23478.58 \text{ } \Omega$ , the gage factor is calculated using Equation 14 to be **6.33**. Table 14 summarizes the gage factors

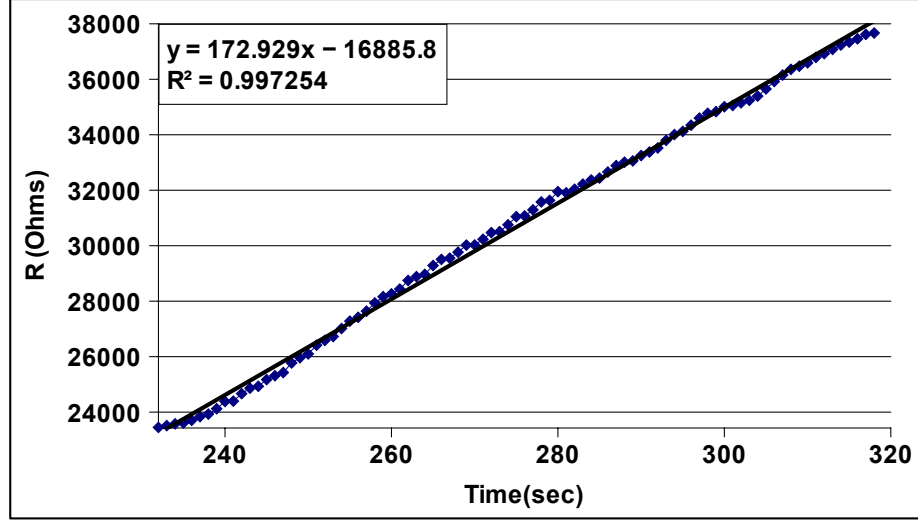


**Figure 50:** Loading profile for a maximum strain of 10%

calculated for a variety of different strains on the *same sample*. The experiments are listed in the order in which they are conducted. Two experiments are performed at each strain level to investigate the effect of strain cycling on the electrical response of the material. These experiments predict extremely high gage factors of the material, that are much higher than metal thin film piezoresistors, which have reported values of 1-2. This would greatly increase the device response for a particular strain.

**Table 14:** Gage factors calculated at different strains using the same sample

#	Maximum strain(%)	Elongation Rate ( $\mu\text{m/s}$ )	Gage factor	$R^2$ fit
1	1	6.77	6.66	0.989
2	1	6.39	5.66	0.976
3	5	8.39	10.27	0.992
4	5	14.56	6.4	0.991
5	10	18.25	8.22	0.991
6	10	26.74	6.33	0.972
		<b>Average Gage factor</b>	<b>7.26</b>	

At this point, it must also be mentioned that potential errors could arise in the calculated gage factor of the piezoresistive composite elastomer, since the strains corresponding to each resistance value recorded are unknown (because of the lack of



instrumentation, the strain values are not recorded simultaneously with the resistance), coupled with the fact that the strain rate being used is the average strain rate over the extension of the material.

As can be seen from Table 14, the gage factor estimated in the first experiment at a particular strain is always higher than that estimated in the second experiment at the same strain. At this point, it is very difficult to assume that as a natural tendency of the material, but it is apparent that the material behaves differently at strains it has never seen before as compared to strains that it has. Hysteresis of the sample resistance is another commonly observed phenomenon in this material. From the graph in Figure 49(b), it can be seen that the hysteresis of resistance just before the start of loading and just after the end of unloading is about  $1462.25\ \Omega$ , but the final hysteresis after the device resistance is allowed to settle down, is about  $425.54\ \Omega$ . As will be seen later, in Section 6.4, a *resistance drift* is almost inherently present in all devices that are fabricated using this material, which can be a cause for concern, since it would severely affect repeatability of results.

But the above reported phenomena are not unknown. Conductive carbon black-polymer composites have been widely investigated, as was reported in Section 2.1.3. Such a system presents a complicated problem due to viscoelastic effects present in the polymer. When the polymer is an elastomer, as is the case here, viscoelasticity is found to control both *strain creep* and thus *resistance creep* [80]. Two of the main issues that are commonly observed in elastomer-carbon black composites are

- Time dependence of resistivity and thus piezoresistance under constant stress
- Effect of strain and strain cycling on the electrical behavior of these composites

Both effects are observed here and a brief discussion is presented.

Peng et.al. [80] have investigated the time dependence of resistivity of carbon-black rubber composites under uniaxial pressures. They reason that molecular motion

of the polymer matrix under uniaxial pressures exists, which results in *strain creep* behavior in the composite. Strain creep, in turn, may gradually change the distance between filler particles and the orientation of the conductive paths present in the composite, thus changing the resistivity and piezoresistance of the material, a phenomenon known as *resistivity creep*. With changing strain, either increasing or decreasing, the distance between conductive fillers is also continuously changing and thus a change in the resistivity is produced. But, when the strains reach a stable value, the movement of the conductive particles continues for sometime. This, in part, also explains a constant decrease of resistance observed in Figure 49(a), after the strip has been fully unloaded. Thus, a drift in the resistance of such materials is commonly observed, primarily due to the viscoelasticity of the elastomer matrix.

Yamaguchi et.al.[108] have conducted a detailed study on the effect of strain and strain cycling on the properties of filled elastomers, mainly Natural rubber (NR) and Styrene-Butadiene rubber (SBR). They investigate ultra high strains in the range of 200-250%, whereas the maximum strains that are used in this research are limited to about 15-20%. Yamaguchi and co-workers claim that when a previously unstrained filled elastomer is stretched to moderate extensions, the electrical resistivity increases due to a breakdown of the carbon black network structure. They also report a phenomena that has been observed in this work - that of a hysteresis in the electrical resistivity before and after unloading. They suggest that the behavior of filled elastomer composites at *large strains* are attributed to the following factors:

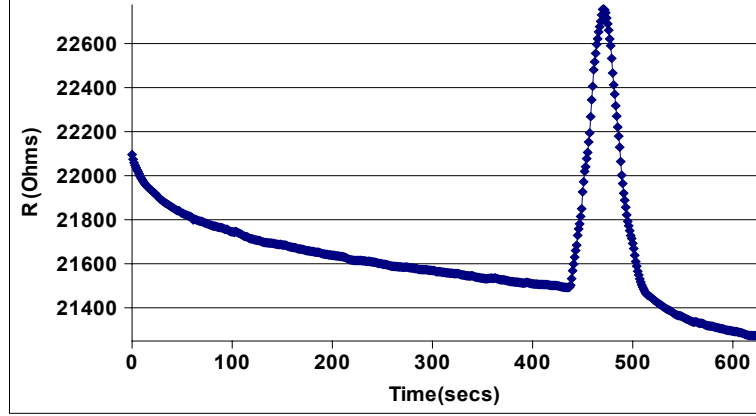
- A bound rubber layer at the interface of the reinforcing particles, resulting in reduced chain mobility of the polymer
- Sliding at the interface of the elastomer and the particle
- Occluded elastomer, in which some of the elastomer is completely encapsulated within carbon black aggregates and thus cannot be extended under loads.

In addition, elastomers are also well known to exhibit cyclic stress softening effects, which leads to reduced modulus in subsequent cycles of experiments. Voet and Cook have also suggested that there are both weak and strong bonds within the carbon black network. The weak bonds are caused by Van der Waals forces and the strong bonds are due to covalent bonding. Thus, a progressive breakdown the carbon-black network occurs with applied strain [101].

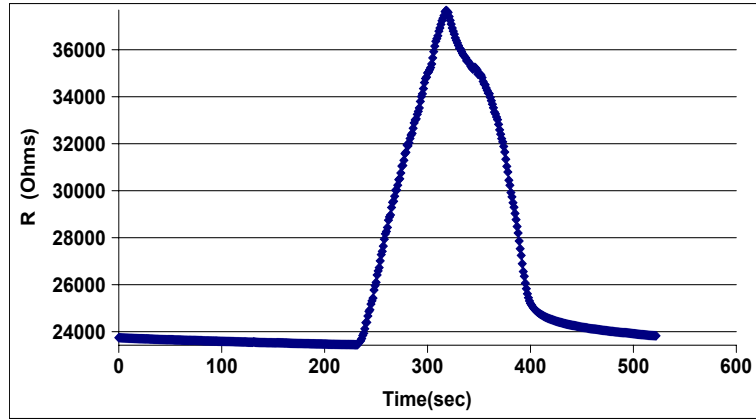
Data presented by Yamaguchi et.al.[108], show that bulk of the breakdown occurs in the first cycle of loading. During subsequent loading cycles, the changes in both mechanical and electrical hysteresis are stabilized. This is also observed, to a certain extent in the experiments presented here, where the very first experiment on a *virgin sample*, shows significant variation of resistance with time under no-load conditions and after the load has been removed. The time taken for stabilization of the resistance is also very high compared with subsequent cycles. This is clearly indicated in the typical resistance-strain experiment conducted, as shown in Figure 51. Although the strains in the two cases are different, the fact remains that the behavior of the elastomer when it *first sees any strain* is significantly different from subsequent cycles. In fact, the only other research group known to use this material, also report the time dependent behavior of the resistance of the material [69].

In conclusion, the above experiments conducted indicate that material used as the sensing piezoresistor for the piezoresistive flow sensor has a low Young's modulus of about 1.72 MPa and high gage factor of 7.26, indicating that it has excellent properties that make it suitable for the application.

The experiments conducted are very basic and they do not take into account other complicated factors like strain-rate etc., when estimating the mechanical and electrical properties of the composite. But repetition of experiments using low strain rates as described above yield reproducible values of the gage factor.



(a) Loading and unloading profile of a virgin device at 1% strain



(b) Loading and unloading profile of the same device at 10% strain

**Figure 51:** Resistance vs Time graph for strain loading and unloading. the sample is untested and unstrained when it is subjected to 1% strain. The 10% strain experiment is performed immediately after that Figure (a) shows that the sample resistance is not stabilized even after a long time, both before and after loading. But during the second strain cycle, the resistance stabilization is almost immediate

### 6.3 *Fabrication process*

Two fabrication processes are discussed here: one for fabrication of “test devices” and the second for mass fabrication of arrays of devices. The latter, in the form of a 5x5 array, demonstrates the feasibility of fabricating large arrays using the process. The first process, shown in Figure 52, is used to fabricate 1x3 array devices. The second process, shown in condensed form in Figure 53, is used to fabricate 5x5 arrays. The difference between the two lies in the interconnection of the device to the package,

which is explained in detail in Section 6.3.4. Each step of the process is explained in the following sections.

### 6.3.1 CO<sub>2</sub> laser machining of the base

The fabrication process starts with fabrication of the base or the substrate structure, as shown in Figures 52(a) and 53(a).

3 mil thick Kapton<sup>®</sup> (300 FN021 consisting of 2 mil thickness of Kapton<sup>®</sup> HN and 1 mil of FEP Teflon as the adhesive) is used as the material for the base. It consists of a layer of fluorinated ethylene propylene, which acts as an adhesive during the lamination process. For fabrication of the 1x3 array test devices however, 5 mil thick Kapton<sup>®</sup> HN is used, which is “laminated” to the ultra-thin Kapton<sup>®</sup> 30HN using a spray adhesive (3M Corp.).

The first step involves machining of square cavities in the base Kapton<sup>®</sup>, which act as *release holes*, for release of the microtufts in the final step. This is achieved by ablating the Kapton<sup>®</sup> using the CO<sub>2</sub> laser. The LS500XL series CO<sub>2</sub> laser (Gravograph Newhermes) operates at a wavelength of 10.6  $\mu\text{m}$ . The laser beam on this system cannot be projected through a mask, and therefore this system is typically used to ablate features greater than or equal to the beam spot size of 160  $\mu\text{m}$ . The two parameters on the CO<sub>2</sub> laser system that can be controlled are the power level (10 - 100% of 60 W) and the speed of the moving laser beam (1 - 100% of 200 mm/s). Figure 54 shows the picture of the Hermes CO<sub>2</sub> laser used for the process. The cutting conditions used in the laser are shown in Table 15. To minimize the charring caused by the cutting process, the Kapton<sup>®</sup> is covered on both sides with thin blue tape. A low level of energy as well as cutting speed are also required to prevent charring.

**Table 15:** CO<sub>2</sub> laser parameters used for through ablation of Kapton<sup>®</sup>

Type of Kapton <sup>®</sup>	Energy (%)	Cutting speed (%)	# of cycles
Kapton <sup>®</sup> HN (5 mils)	1	3	7-8

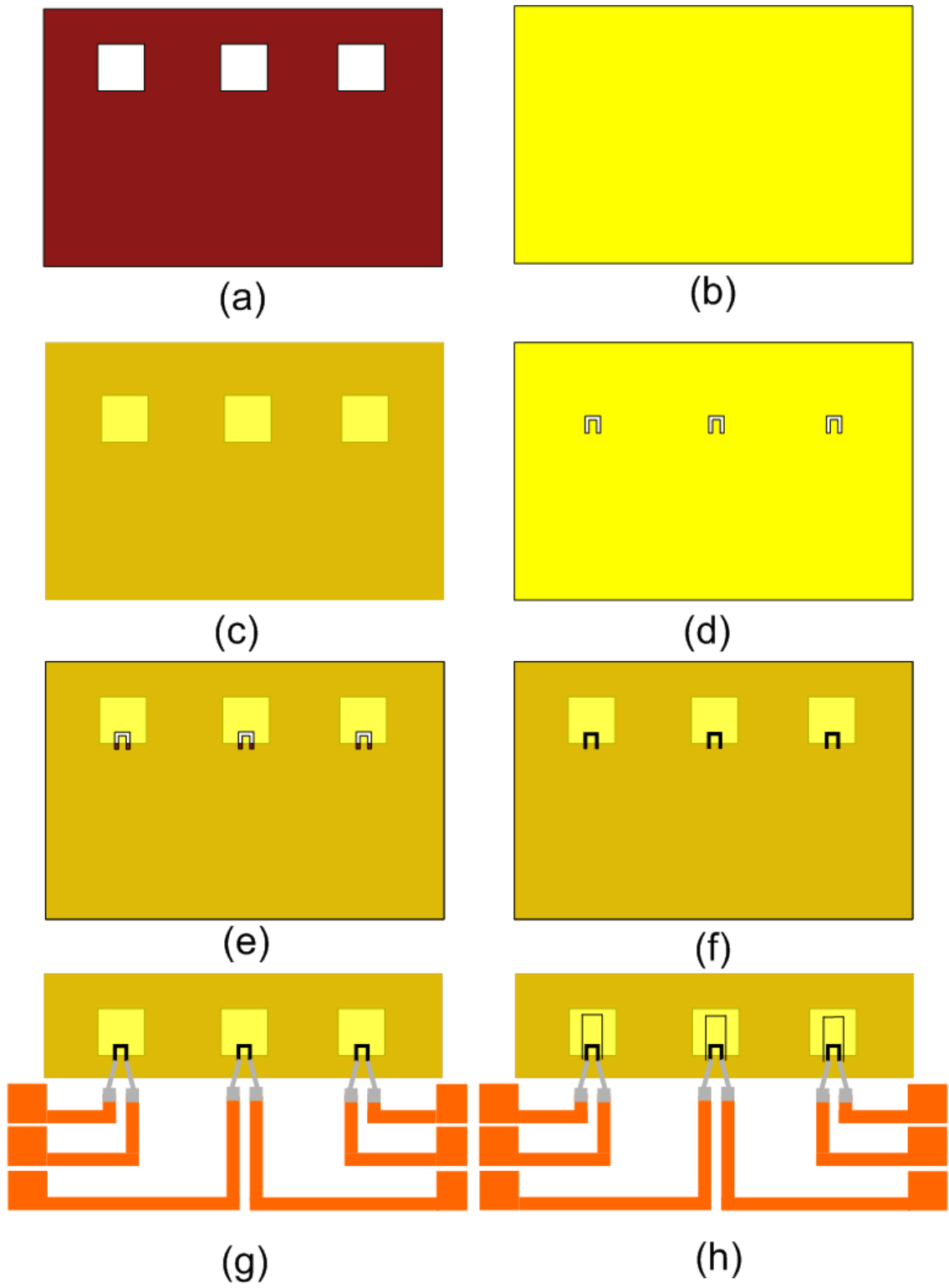
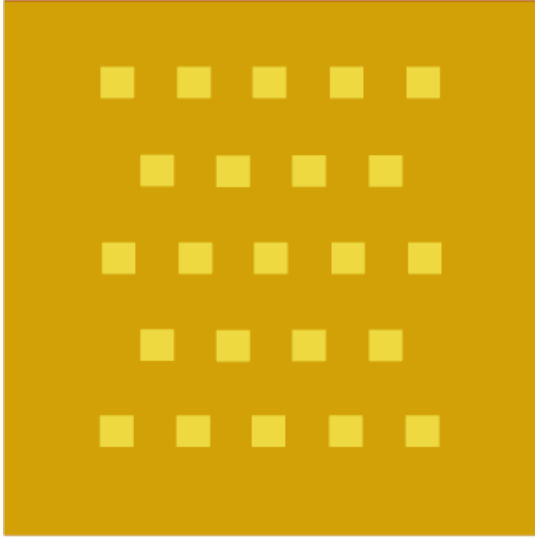
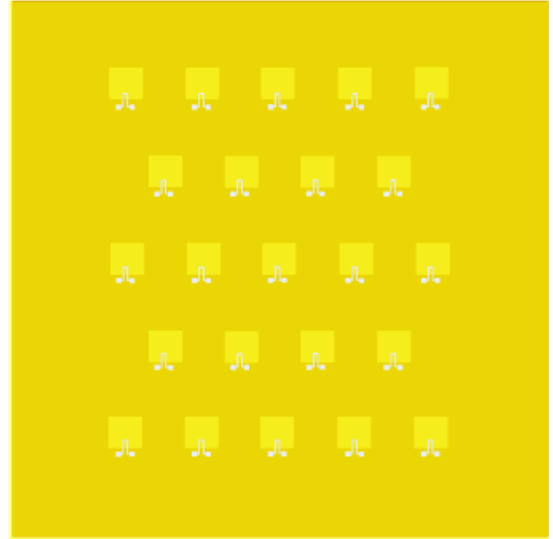


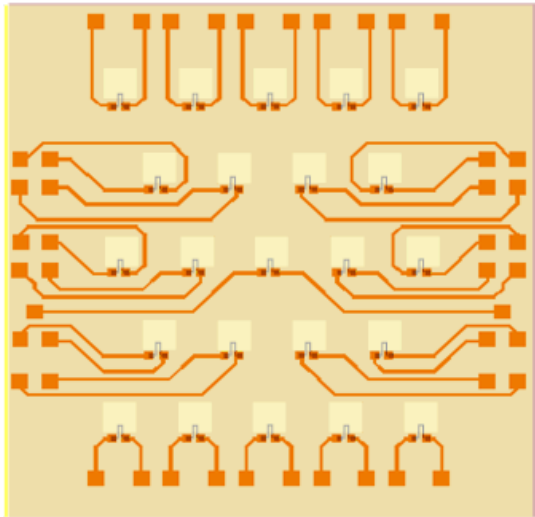
**Figure 52:** Fabrication process flow for 1x3 arrays of test devices



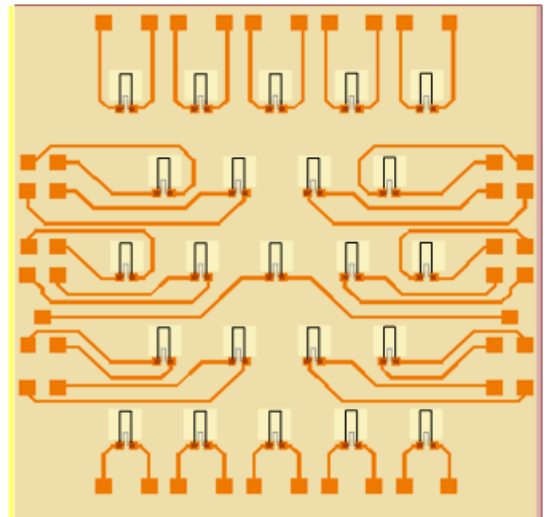
(a)



(b)



(c)



(d)

**Figure 53:** Fabrication process for a 5x5 array with backside interconnections



**Figure 54:** The LS500XL series CO<sub>2</sub> laser

### 6.3.2 Lamination of Kapton®

As mentioned before, lamination is only used for fabrication of the 5x5 arrays (Figure 53(a)). Lamination is an important process in the fabrication of the flexible sensors, since it ensures strong adhesion between the microtufts and the substrate at the point of attachment. It is also necessary since the sample undergoes photoresist processing steps which involve solvents that would attack ordinary spray adhesives.

The Kapton® sheets laminated together are 300 FN021, which is a corona treated FEP Kapton® and the ultra thin 30 HN. A bench top lamination press (Carver Inc.) is used for the process. The schematic of the lamination process is shown in Figure 55(a) and the lamination press used is shown in Figure 55(b).

The lamination process is carried out at a pressure of 200 psi and a temperature of about 280°C (at which temperature the Teflon FEP melts), with a dwell time of about 30 minutes at that temperature. After 30 mins, the heating of the platens is stopped and the system allowed to cool to about 150°C, before the sample is removed. Care must be taken to ensure that the temperature does not exceed 290°C, since at very high temperatures, the FEP starts flowing into the square cavities machined into the Kapton®, and this would modify the mechanical properties of the microtufts. The lamination ensures that the bonding between the 2 sheets is strong. The sample is



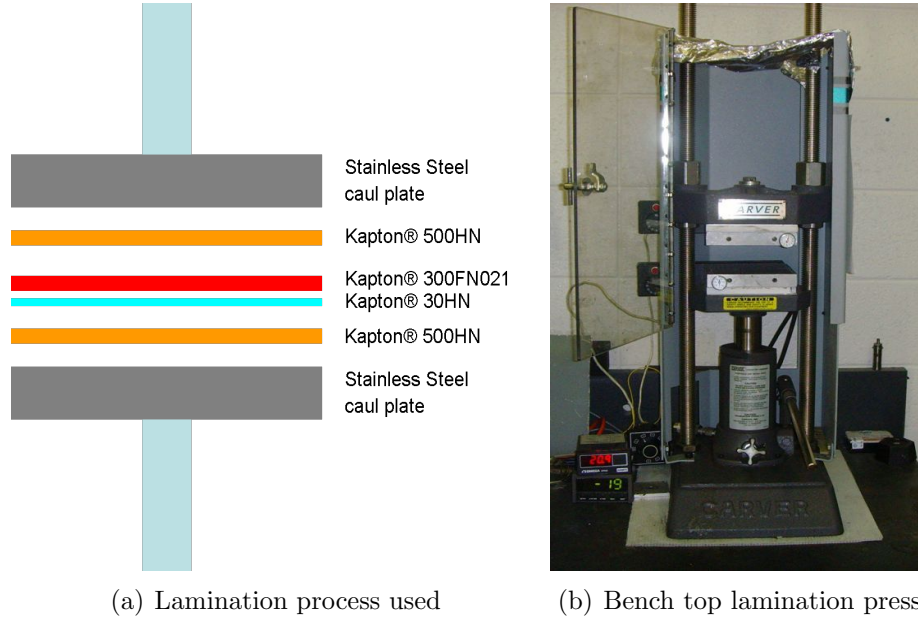


**Figure 55:** Lamination of Kapton®

now ready for further processing.

### 6.3.3 Microstenciling of the conductive composite

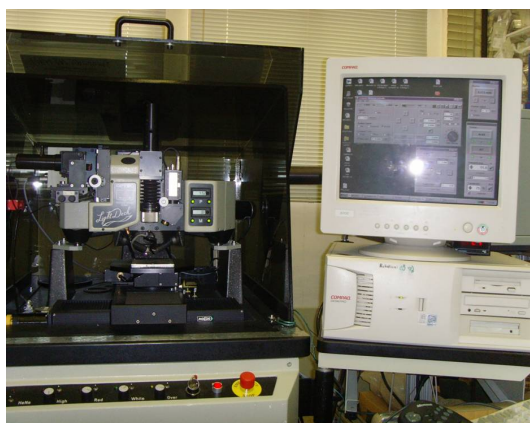
The next step in the process is patterning the piezoresistive composite material on the laminated substrate (Figures 52(d), 53(b)). This is achieved by a microstenciling process, whereby the elastomer material is *doctor-bladed* through a stencil mask onto the substrate. Prior to this the laminated sample is thoroughly cleaned using acetone, methanol and IPA in a sonicator and treated for 1 minute in an oxygen plasma, using the parameters shown in Table 16. This helps in the adhesion of the stencil printed composite material.

**Table 16:** Oxygen plasma treatment parameters used in the RIE

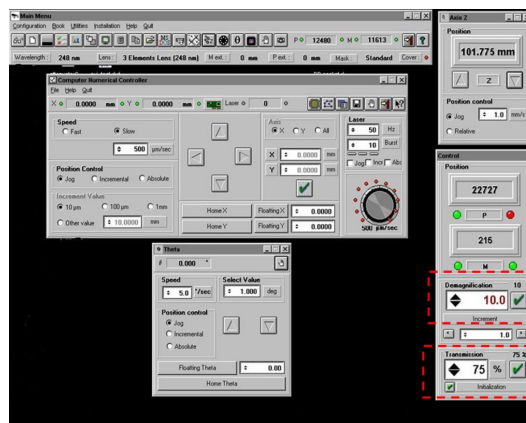
Gases	Power (W)	Pressure (mTorr)
O <sub>2</sub> (40 sccm)	200	200

The microstencil itself is fabricated using the excimer laser. The LPX2000 series excimer laser (Lambda Physik) operates at a wavelength of 248 nm. This system uses

krypton (Kr)/fluorine (F) as the rare/halide gas mixture and neon (Ne) as the buffer gas. The laser provides 20 ns pulse-lengths, operates up to 100 Hz, and produces up to 600 mJ of energy per pulse. The laser, with an initial beam spot size of 4mm x 15 mm, is interfaced with a Resonetics micromaster large excimer laser workstation. In the workstation, the laser beam first travels through an attenuator, which scales the energy from 5% to 98% of the original value. The beam is then projected through a metal mask with openings of varying diameters depending on the feature to be ablated. The final stage of the workstation focuses the beam down to 4-11 times the projected size through demagnification optics. A computer controls the energy and pulse rate of the original laser beam as well as the attenuation, demagnification, and focus of the beam. The computer also controls the xy position and rotation of a stage that holds the material to be ablated. The projection mask is positioned into the path of the laser by hand. Figure 56(a) shows the LPX2000 series excimer laser and Figure 56(b) shows a screen shot of the laser control software.



(a) The LPX2000 series excimer laser



(b) Screen shot the laser control software

**Figure 56:** Excimer laser for micromachining of Kapton®

For fabrication of the microstencil, an AutoCAD (Autodesk Inc.) drawing is developed. This file is used as the input to the computer that controls the laser. An OMS file is generated based on the designs in the AutoCAD file and the required laser parameters (bursts, mask diameter etc.). The parameters used for cutting the

microstencil are given in Table 17. The stencil is made using Kapton<sup>®</sup> 50HN ( $\sim 12.7 \mu\text{m}$  thick) using a laser beam spot size of  $10 \mu\text{m}$ . The mask for the laser is made using an IR laser (Resonetics 1048/523nm Nd:YLF Laser) by micromachining of brass. A  $110 \mu\text{m}$  mask is used for the current application.

**Table 17:** Excimer laser parameters used for cutting the microstencil

Demag	Energy (mJ)	Attenuation(%)	Bursts	Frequency(Hz)	Passes
11	200	75	30	90	1

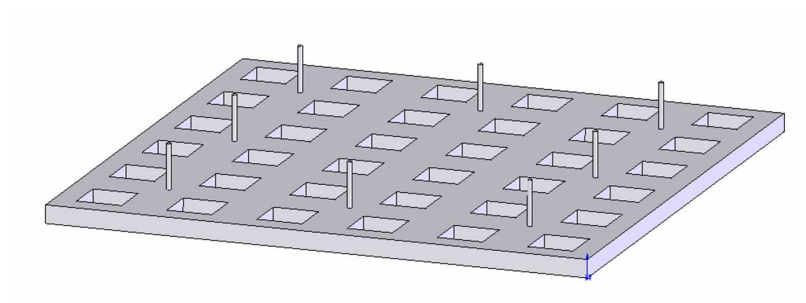
A variety of sizes of the microtufts and the corresponding piezoresistors are tried and hence different stencil mask designs are used. The dimensions are specified in Section 6.3.7.

Once the microstencil is fabricated by excimer laser micromachining, it is aligned with the laminated Kapton<sup>®</sup> substrate and adhered to it using a thin coating of spray adhesive (3M Corp.) (Figures 52(e),53(b)). The alignment itself is achieved by using an *alignment jig*, fabricated using stereolithography. The alignment jigs used are shown in Figure 57.

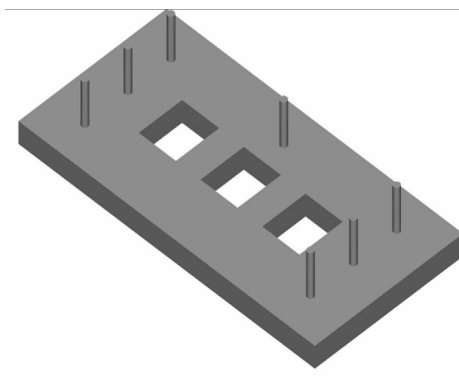
A alignment error of  $50\text{-}100 \mu\text{m}$  is typically obtained while using this process, but the designs are accordingly adjusted to compensate for this error.

The conductive carbon black elastomer composite Elastosil<sup>®</sup> LR3162 is a two part mixture with a mixed viscosity of  $7,000,000 \text{ mPa}\cdot\text{sec}$  and thus very difficult to process using conventional techniques like spin coating etc.

In order to fabricate the piezoresistors, equal amounts of Part A and Part B (roughly) are thoroughly mixed and *doctor-bladed* across the aligned stencil mask (Figures 52(f),53(c)). Care is taken to apply the pressure in a uniform fashion, holding the blade at an angle of  $45^\circ$  to the substrate. The process is depicted in Figure 58. After stencil printing of the conductive elastomer, the stencil is carefully removed, leaving the patterned elastomer on the substrate, as shown in Figures 52(f),53(c).



(a) for a 5x5 device array



(b) for a 1x3 device array

**Figure 57:** SLA alignment jigs for stencil printing of the conductive elastomer

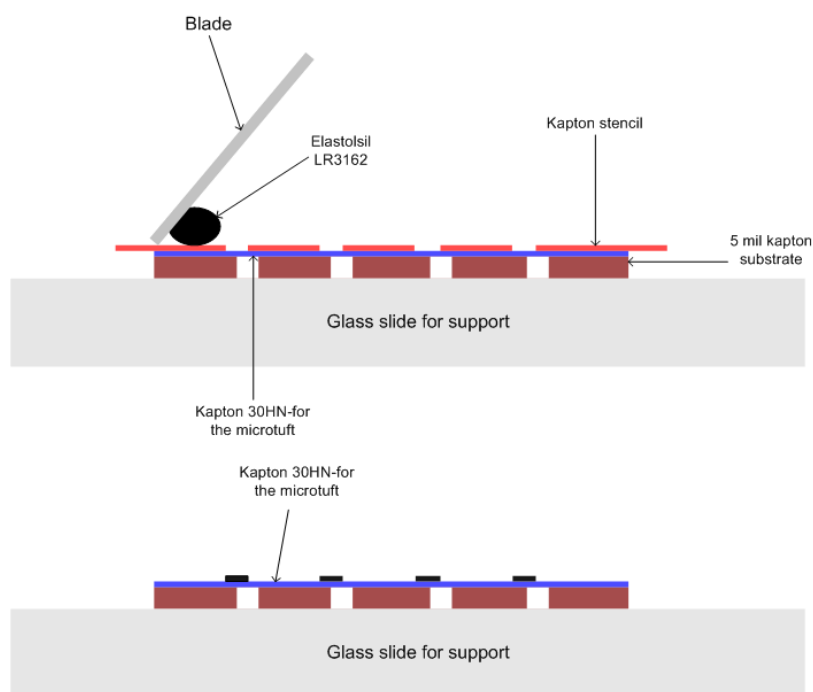


**Figure 58:** Microstenciling of Elastosil<sup>®</sup> LR3162

After printing the elastomer onto the substrate, the sample is placed in a convection oven at 130°C for about 2 hours to ensure that the elastomer cures completely. Figure 59 shows some designs of the elastomer after curing. One of the drawbacks of the process is that the thickness of the elastomer is difficult to control. Ideally, it should be the same as the thickness of the stencil used, but it usually is much thicker than that. Typically thicknesses of the piezoresistor obtained vary anywhere between 20-50  $\mu\text{m}$ .

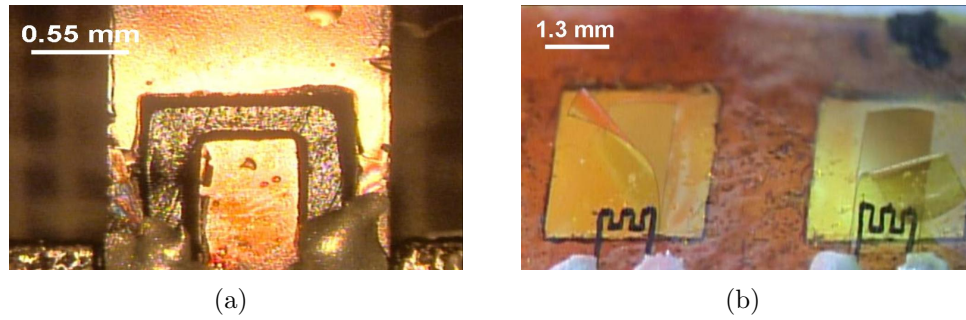


**Figure 59:** Piezoresistor designs after curing of the conductive elastomer

Once cured, the elastomer is supposed to have a volume resistivity of 9  $\Omega\text{-cm}$ . Once the piezoresistors are patterned, they must be connected to an external circuit for data acquisition. The patterning of the electrodes is described in the next section.

#### 6.3.4 Patterning of electrodes

Upto now, all the steps described above are common to both the 1x3 array test devices as well the 5x5 array devices. But, the methodology of interconnection to an external circuit is different for the two cases.

##### 6.3.4.1 1x3 array test devices

For the 1x3 test array, which is fabricated to demonstrate proof-of-concept, the interconnection is elementary and achieved by using conductive silver epoxy (Ted-Pella Inc.) (Figure 52(g)). The external PCB is fabricated using the previously used *inkjet printer toner transfer technique* [39]. The processed 1x3 array samples are attached

to the PCB using spray adhesive (3M Corp.). The assembly is then viewed under a stereo-microscope with a video camera and the piezoresistors are connected to corresponding pads on the PCB using the silver epoxy. The silver epoxy is then cured at a temperature of about  $100^{\circ}\text{C}$  for a period of 2 hours to ensure that a stable connection is achieved. Figure 60 shows the interconnection scheme.

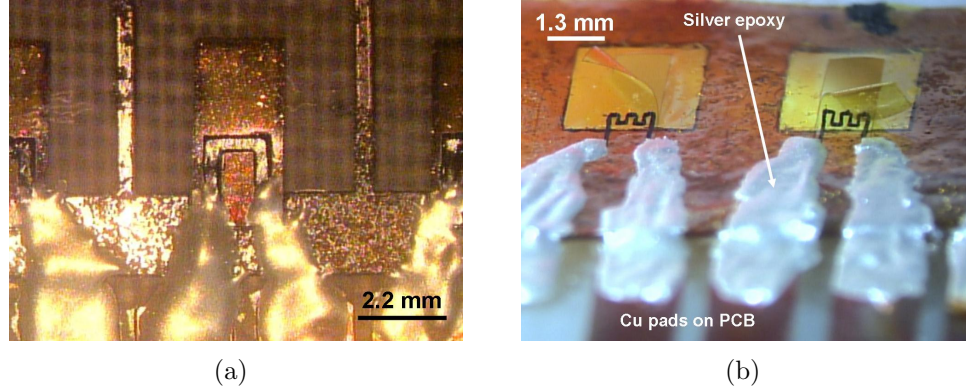


**Figure 60:** Interconnection of the piezoresistors to an external PCB using silver epoxy

This technique is however impractical for large area devices. Thus, a photolithography based process is proposed and demonstrated for the 5x5 array.

#### 6.3.4.2 Interconnection for large area arrays

For the large 5x5 arrays, electrical interconnection is achieved using standard photolithography and electroplating.

Upto this point, the piezoresistors have been stencil printed and patterned. The sample is cleaned very carefully in acetone to remove residues of the spray coated adhesive from the microstencil. Silicone elastomers usually absorb most solvents, hence the exposure time to solvents must be minimal. After drying the sample, it is then cleaned in an oxygen plasma for 2 minutes in a reactive ion etching system (RIE, Plasma Therm Inc.), using the recipe shown in Table 16.

A seed layer of titanium (Ti)/copper (Cu)/titanium (Ti) (300Å/3000Å/300Å thickness) is deposited using a DC sputtering system (CVC Inc.). The titanium

layers are used as both, an adhesion layer for the copper, as well as for prevention of oxidation of copper. The sample is then mounted onto a glass slide using Kapton<sup>®</sup> tape, which acts as a rigid support for the subsequent wet processing steps.

After the cleaning steps discussed above, a negative tone photoresist, NR9-8000 (Futurrex Inc.), is spun coat onto the sample and patterned using the conditions described in Table 18. The thickness of the resist is approximately  $20\mu\text{m}$ . The soft baked resist is exposed in a Karl Suss MA6 (Karl Suss Inc.) mask aligner, using Channel I, which has peak intensity at a wavelength of 365 nm. All the baking steps are done on a contact hot plate.

**Table 18:** Processing conditions for NR9-8000 patterning

Spin speed	Soft Bake	Exposure dose ( $\text{mJ}/\text{cm}^2$ )	PEB
500/100/10; 800/300/40	70 <sup>0</sup> C for 5 mins; 150 <sup>0</sup> C for 2 mins	650	85 <sup>0</sup> C for 5 mins

After exposure and post-exposure bake (PEB), the sample is allowed to rest for a period of 1 hour to prevent any thermal stress related delamination of the resist. The development of the patterns is done using RD6 (Futurrex Inc.) developer, with a development time of about 3-4 minutes. An optional short descum step is also used to remove any photoresist residues post-development, using the RIE. The descum recipe used in the RIE is shown in Table 19.

**Table 19:** NR9-8000 descum recipe used after development

Gases	Power	Pressure (mTorr)
O <sub>2</sub> (50 sccm)	200 W	300

Once the electrode patterns are defined using NR9-8000 lithography, the sample is ready for electroplating. Firstly, the top layer of Ti is etched in dilute hydrofluoric acid (HF) solution (HF (33-40%, J.T. Baker):DI water 1:50). The sample is then dipped in dilute hydrochloric acid (HCl) solution (HCl (33-40%, J.T. Baker):DI water 1:50) to

clean the copper surface. All the residual etchants are removed by a thorough DI water wash. Copper is then electroplated using a standard plating bath ( $\text{CuSO}_4 \cdot 5\text{H}_2\text{O}$ -250 gms/litre,  $\text{H}_2\text{SO}_4$ -25 ml/litre), with a pure copper plate as the anode and the sample to be plated as the cathode. The current density is set to  $10 \text{ mA/cm}^2$ , and the sample is plated for about 1:30 hours, leading to a plated copper thickness of 12-15  $\mu\text{m}$ . After plating the sample, the patterned NR9-8000 resist is stripped completely in acetone, followed by etching of the remaining seed layer of Cu/Ti. In some cases, a post plating/stripping descum is used before the seed layer is etched using the RIE with the parameters shown in Table 20. The copper is etched using *blue etch* (an ammoniacal Cu etchant), which is a very slow etchant for the copper. This prevents excessive etching of the plated copper along with the seed copper. Titanium is etched as before in dilute HF.

**Table 20:** NR9-8000 descum recipe used after copper plating and stripping of the resist

Gases	Power	Pressure (mTorr)
O <sub>2</sub> (50 sccm) CHF <sub>3</sub> (5 sccm)	300 W	250

Figure 61 shows the plated copper on the Kapton<sup>®</sup> substrate with the patterned piezoresistors. As can be seen from Figure 61(c), adhesion of the plated copper on the Kapton<sup>®</sup> 30HN is a major issue that needs to be solved. Typically, Dupont does supply surface treated films suited for processing of flexible PCBs. Kapton<sup>®</sup> 500HN is one such surface treated Kapton<sup>®</sup> film, which has much stronger adhesion with Cu. Thus, a custom process to improve adhesion of Cu on the Kapton<sup>®</sup> 30HN, which is critical for the process, must be developed, since surface treated Kapton<sup>®</sup> 30HN films are currently unavailable.



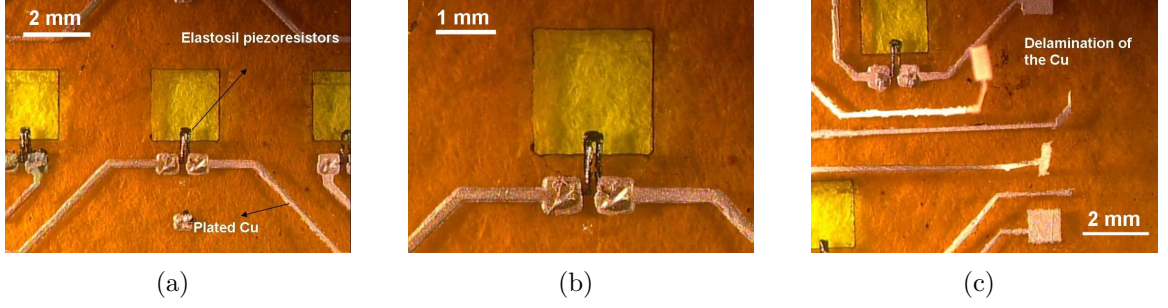


**Figure 61:** Plating of Copper electrodes on the Kapton<sup>®</sup> substrate. Figure (c) shows the delamination of the copper because of the poor adhesion with Kapton<sup>®</sup>

### 6.3.5 Improving the flow-structure interaction-deposition of stress inducing layers

The microtufts that are released by excimer laser ablation in the final step of the process, show little or no curvature, due to absence of a stress-gradient in the Kapton<sup>®</sup> film. Curvature is important for the flow sensing application, since deflection of the microtuft is caused by its interaction with the wind flow. A microtuft with no inherent curvature will not be responsive to the imposed wind flow. Thus, improving the *flow-structure interaction* is of great importance in increasing the device sensitivity and response.

Bimorph cantilevers based on two layers of materials having different coefficients of thermal expansion (CTE) have been widely investigated. Wang et.al. [102, 103] have fabricated a microcantilever based flow sensor where the curvature of the silicon nitride beam is caused by the thermal stress induced by heating and cooling steps in the process. However, it is not clear if such a curvature is produced by a CTE mismatch or due to intrinsic stresses present in the material. Stresses present in silicon dioxide films deposited by chemical vapor deposition (CVD) or plasma enhanced CVD (PECVD) have also been reported [1, 72]. A more detailed analysis of the source of this stress is undertaken in Section 6.5.

For the case of the Kapton<sup>®</sup> microtufts, the curvature is induced by depositing a

layer of silicon dioxide just before releasing the structures. Figure 62(a) is a photomicrograph of microtufts with no stress inducing layer and thus no curvature. Figure 62(b) shows a similar microtuft with silicon dioxide deposited on one side, showing a pronounced curvature. The silicon dioxide itself is deposited using the plasma enhanced chemical vapor deposition system (PECVD, Plasma Therm Inc.), using the conditions given in Table 21. Silicon nitride is also deposited on one occasion, but was abandoned due to irreproducibility of curvatures. The deposition parameters for PECVD  $\text{Si}_3\text{N}_4$  is given in Table 22. A low temperature of deposition of  $150^\circ\text{C}$  is used to prevent any decomposition of the spray adhesive used in the case of the 1x3 test devices.

**Table 21:** Conditions used for PECVD deposition of silicon dioxide

Gases	Flow rate (sccm)	Pressure (mTorr)	Power (W)
$\text{SiH}_4$	400	900	25
$\text{N}_2\text{O}$	900		

**Table 22:** Conditions used for PECVD deposition of silicon nitride

Gases	Flow rate (sccm)	Pressure (mTorr)	Power (W)
$\text{SiH}_4$	200	900	25
$\text{N}_2\text{O}$	900		
$\text{NH}_3$	5		

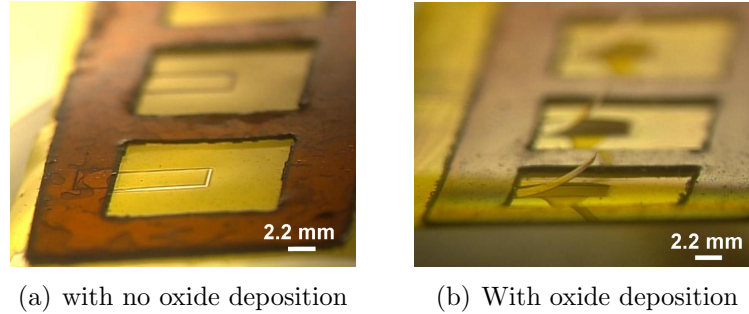


**Figure 62:** Stress induced curvature of Kapton<sup>®</sup> 65E ( $16.51 \mu\text{m}$ ) microtuft

The amount of curvature produced is found to depend on the following factors:

1. Thickness and geometry of the material of the microtuft. Rigid structures will have a smaller curvature for the same thickness of the oxide film, as shown in Figure 63.
2. The thickness of the curvature inducing layer ( $\text{SiO}_2$ ). Figure 64, where the 3 microtufts shown have progressively lower thickness of oxide from right to left, seems to indicate that thicker oxide films generate greater curvatures, but more experiments must be conducted to verify this, especially since Chen et.al. have reported that thinner oxide films on silicon have greater compressive residual stress compared to thicker oxide films [22].

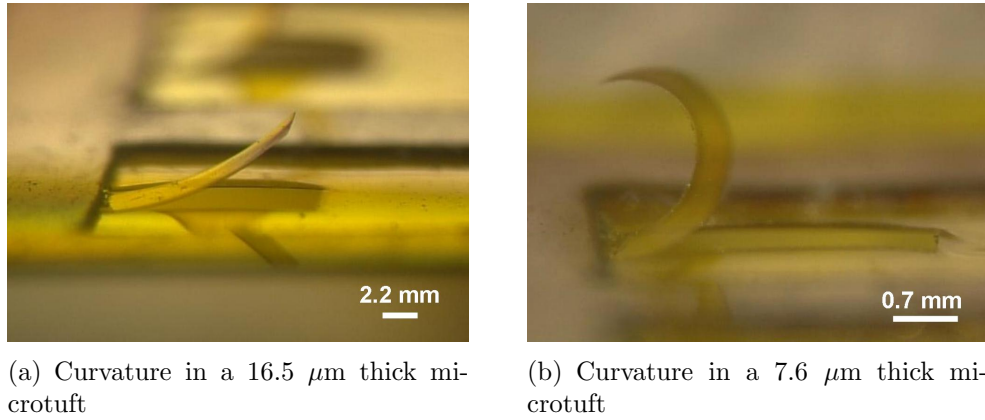


**Figure 63:** Dependence of curvature of microtuft on thickness of Kapton<sup>®</sup>. The oxide thickness and the geometry are the same

It is important to note that the silicon dioxide deposited has a *compressive stress*, because of which the curvature of the microtufts is always in the direction of the deposition. In other words, a deposition on the top surface of the Kapton<sup>®</sup> will cause a curvature that is into the plane of the paper, as shown in Figure 65.

The other important thing to note is that, for the 1x3 test devices, the deposition of the oxide takes place after the *packaging* onto the external PCB and is achieved by flipping it over and depositing on the backside of the sample. This is done because

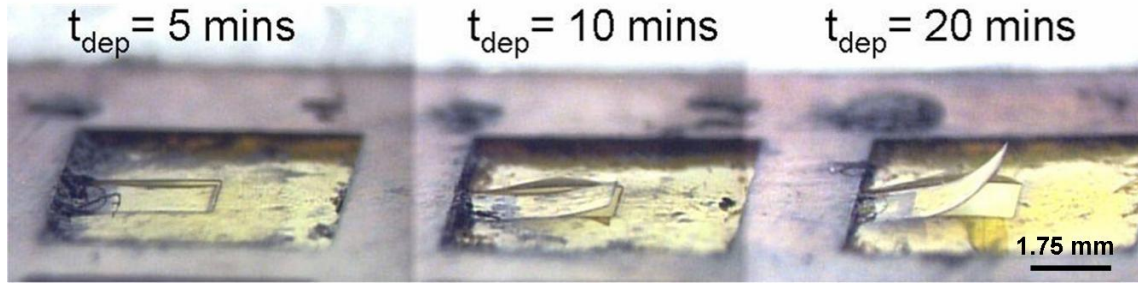


**Figure 64:** Dependence of curvature on thickness of oxide film deposited. The material of the microtufts are Kapton® 50 FPC ( $12.7 \mu\text{m}$  thick). The curvature is not as pronounced because of the increased stiffness due to the presence of the piezoresistors. 20 mins of deposition corresponds to an oxide thickness of  $1 \mu\text{m}$

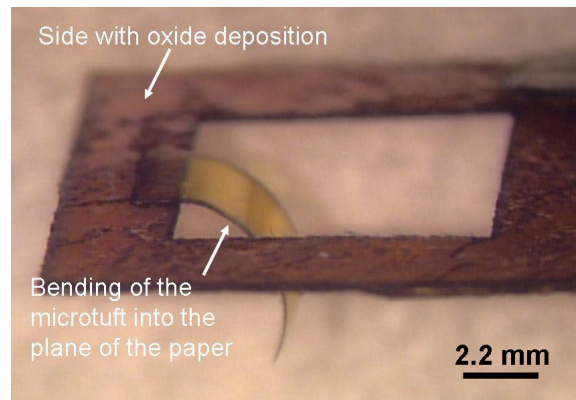


**Figure 65:** Bending of the microtuft into the plane of the paper. The material of the microtuft is Kapton® 50HN ( $12.7 \mu\text{m}$  thick)

the curvature produced in the Kapton® microtuft is much smaller than the thickness of the PCB and this in turn would prevent any interaction of the tuft with the flow. Thus, the oxide and the piezoresistors are on opposite sides of the microtuft.

But in the case of the 5x5 array, since the whole package consists of 5 mil Kapton®, there is no interference with the flow-structure interaction. Thus, the oxide is deposited after patterning of the piezoresistors and electroplating of the electrodes. This eventually leads to *backside interconnects* using a flexible substrate, achieving the ultimate goal for the application. The backside interconnects are demonstrated in the illustration shown in Figure 68.

### 6.3.6 Release of the microtuft structures

After deposition of the stress inducing layer of silicon dioxide, the final step in the process is to release the microtufts. The release is achieved by cutting the Kapton® 30HN film in the shape of the rectangular microtuft in the excimer laser described in Section 6.3.3. Once again a  $10\text{ }\mu\text{m}$  laser beam spot size is used. The laser parameters used for the process are shown in Table 17 and are same as the set used for cutting the microstencil. The difference between cutting the microtufts and fabrication of the microstencil lies in the extra alignment step that is required in the former's case. It must be remembered that the substrate at this point contains the conductive elastomer piezoresistor patterns along with the interconnections (silver epoxy to the board in the case of the 1x3 test array and copper plated electrodes for the 5x5 arrays). Thus alignment of the final cut with the structures already on the substrate is critical. The excimer laser setup shown in Figure 56(a) comes with a stage whose movement in the x, y and  $\theta$  (angle) directions can be controlled accurately. Figure 66 shows the software that controls the movement of the stage.

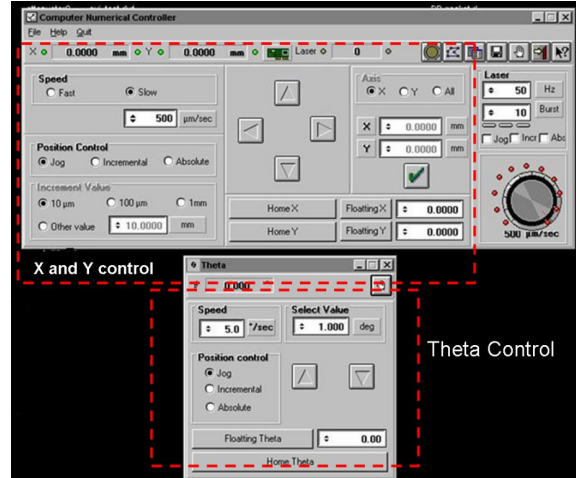


**Figure 66:** Alignment control in the Excimer laser

The features on the substrate are used as alignment marks for the alignment process. A typical alignment scheme involves x, y translation at one end of the

sample and a theta movement at the other end. This is continued until both ends of the sample (horizontal or vertical) lie along the path of a vertical or horizontal travel of the laser beam. Upon satisfactory alignment of the laser beam to the features on the substrate, the microtuft pattern is cut using a  $10\mu\text{m}$  spot size to get maximum alignment tolerance. A single pass is required to cut through the  $7\mu\text{m}$  thick Kapton<sup>®</sup> and upon release, the microtuft structure curls in the direction of deposition.

The next section discusses the final device.

### 6.3.7 Final device

From a structural rigidity point of view, different geometries would give rise to different rigidities and hence a different curvature of the microtufts. The final goal is to push the limits of the fabrication process used to make microtufts that are the smallest in size and have least rigidity. Different geometries are tried and final devices fabricated using these geometries are shown in Figure 67. For the final testing, however, the results of only two different geometries are shown, since the other geometries don't fall into the microscale regime.

Table 23 gives details of the dimensions of all 4 devices shown in Figure 67.

**Table 23:** Device and piezoresistor dimensions for the devices fabricated. L and W are the length and width respectively. T is the thickness of the Kapton<sup>®</sup> used for the tuft fabrication. Subscript t is for the tuft and subscript p is for the piezoresistor

Device #	$L_t$ (mm)	$W_t$ (mm)	$T_t$ ( $\mu\text{m}$ )	$L_p$ (mm)	$W_p$ (mm)	Rigidity (N/m)
1 (Figure 67(a))	10	7	16.5	1	19.5	-
	10	15	16.5			
2 (Figure 67)(b)	20	7	16.5	19.5	1	-
3 (Figure 67)(c)	3.5	2.2	16.5	4.15	0.3	0.1441
4 (Figure 67)(d)	1.5	0.4	7.6	2.89	0.06	0.0325

The rigidity is calculated using Equation 15. The Young's modulus of Kapton<sup>®</sup> is 2.5 GPa (obtained from Dupont). The dimensions are defined in Figure 12 in Section 3.2.1.



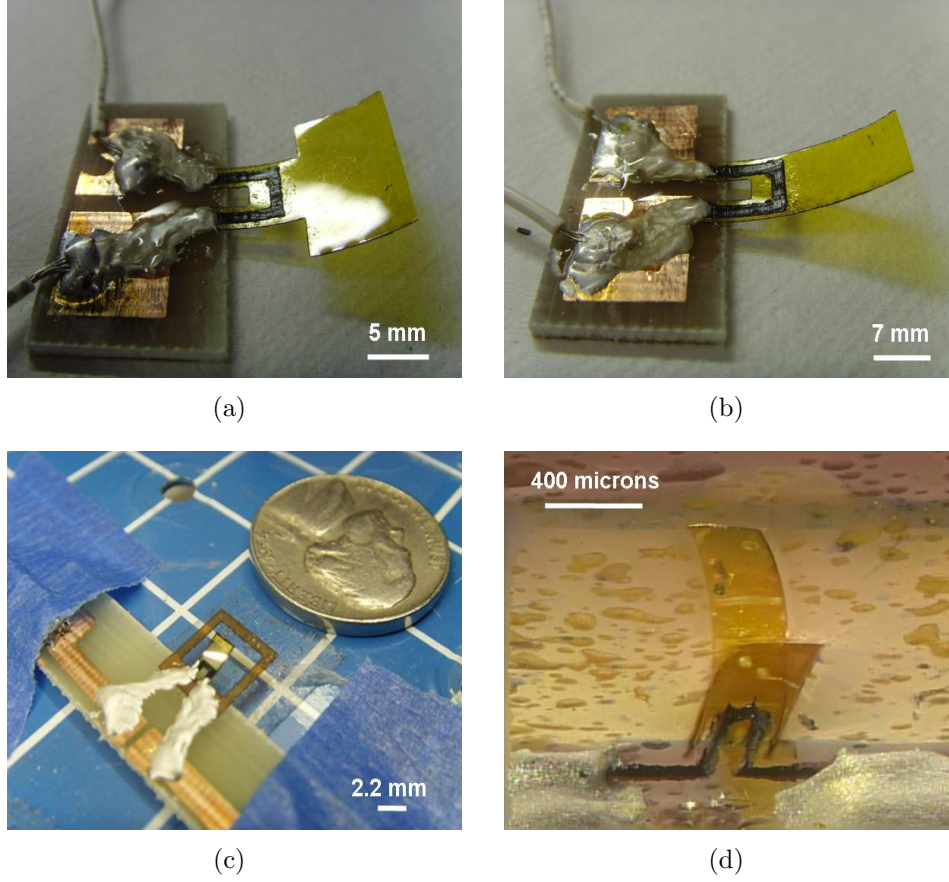


**Figure 67:** Scaling of the microtuft dimensions. Figures (a) and (b) are macroscale tufts that are fabricated using the CO<sub>2</sub> laser alone. Figures (c) and (d) are for scaled down tufts. Devices (a) and (b) have no stress inducing films. Device (c) has 5000Å of silicon nitride and device (d) has 1 micron of silicon dioxide deposited on the backside. The testing results shown in Section 6.4 are for the devices shown in Figures (c) and (d)

$$Rigidity = \frac{EWH^3}{4L^3} \quad (15)$$

For the smallest dimensions of the microtuft used (Figure 67(d)), the choice of Kapton® 30HN, which has a thickness of 7.6  $\mu\text{m}$ , as the device material is obvious, as is apparent from the rigidity analysis in Table 24. Figure 63 shows the thickness dependent curvature of the Kapton® microtuft. The rigidities calculated in Tables 23 and 24 are without the stress inducing films.

Figure 61 has already shown how the Cu electrodes were fabricated for backside

**Table 24:** Rigidity analysis for 1.5mm x 0.4 mm microtufts for different thicknesses of Kapton<sup>®</sup>. L and W are the length and width respectively

Kapton <sup>®</sup> thickness ( $\mu\text{m}$ )	L (mm)	W (mm)	Rigidity (N/m)
Kapton <sup>®</sup> 30HN-7.6	1.5	0.4	0.0325
Kapton <sup>®</sup> 50FPC-12.7			0.1517
Kapton <sup>®</sup> 65E-16.5			0.33275

interconnection purposes. Figure 68 shows the *backside interconnection* concept.

## 6.4 Wind tunnel testing

### 6.4.1 Results

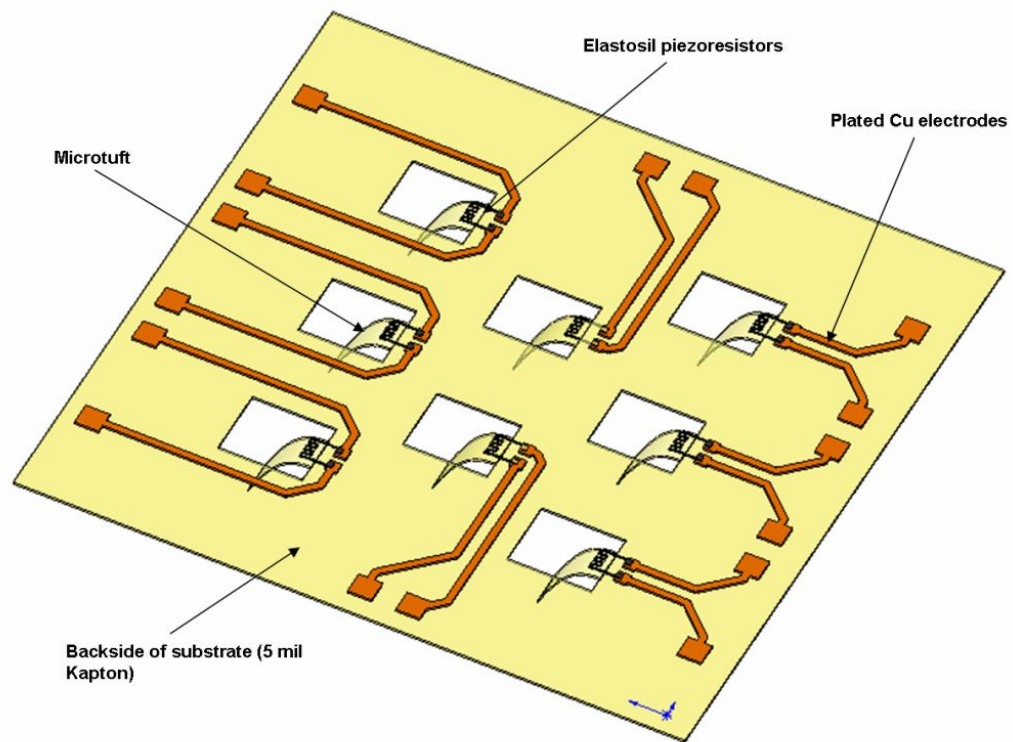
The wind tunnel experimental setup is the same one that is used for testing devices fabricated by the dissolving mold MTM process in Section 5 as shown in Figure 69(a). The placement of the device with respect to the direction of airflow is shown in Figure 68(b).

The first testing data shown are for the 3.5mm x 2.2 mm device (Figure 67(c)). All the dimensions as well the rigidity are shown in Table 23. The curvature in this case is induced by the deposition of 5000Å of PECVD nitride. Figure 69(b) shows the curvature induced in the tuft. The test conducted on the device is the same as the one conducted for the PDMS devices. The wind tunnel velocity is varied and the device response is tracked in the form of a resistance change. All resistance measurements are made using a digital multimeter (Keithley 196 DMM system). Figure 70 shows the response of the device to a varying wind flow. Table 25 shows the resistance hysteresis at the end of the experiment.

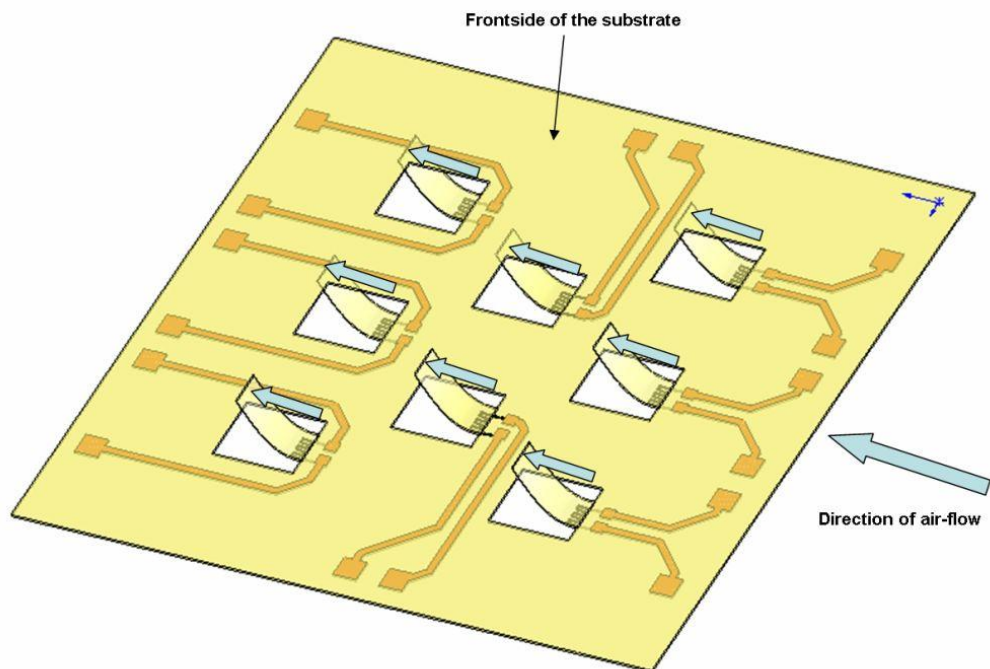
**Table 25:** Resistance variations with experiments.  $R_i$ ,  $R_f$  are the device resistances before and after the wind tunnel experiment. Hysteresis is defined as  $R_i - R_f$ . The % hysteresis is calculated with respect to the initial resistance

Expt. #	$R_i$ ( $\Omega$ )	$R_f$ ( $\Omega$ )	Hysteresis ( $\Omega$ )	% Hysteresis
1 (Type I)	10464.11	10393.96	-70.15	0.67



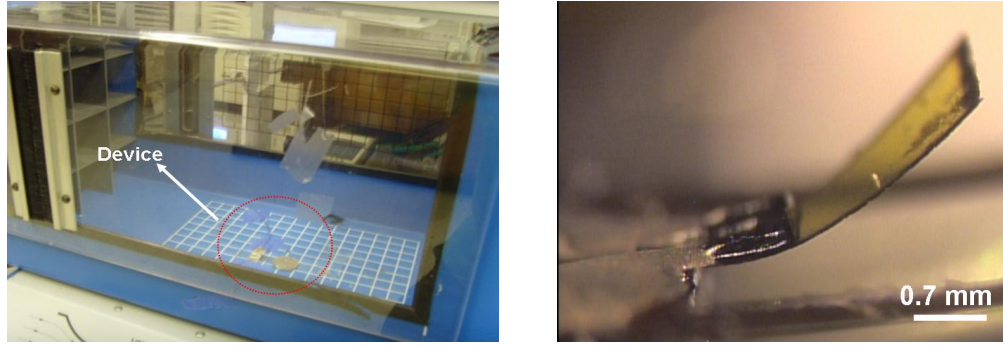


(a)



(b)

**Figure 68:** Backside interconnects on a large area array



(a) The wind tunnel setup for testing of the microtufts

(b) Curvature in the first device tested. The curvature is induced by silicon nitride deposition

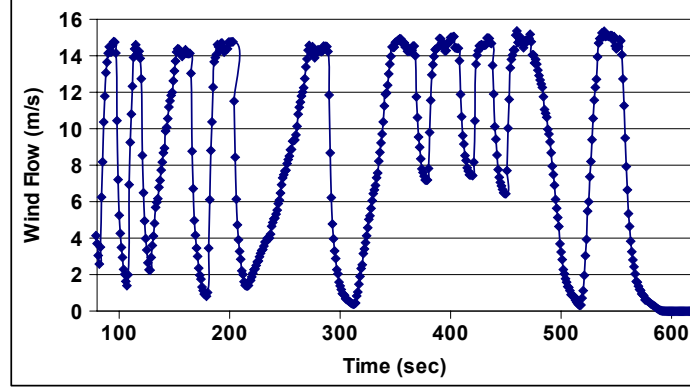
**Figure 69:** (a) Experimental setup for the wind tunnel experiments of the microtuft based flow sensors (b) Kapton<sup>®</sup> 65E (16.5  $\mu\text{m}$  tuft )

The results presented here on are for the smallest devices fabricated so far with a microtuft length of 1.5mm and a width of 400  $\mu\text{m}$ . The curvature of the devices tested is shown in Figure 71. Two types of experiments are performed on these devices:

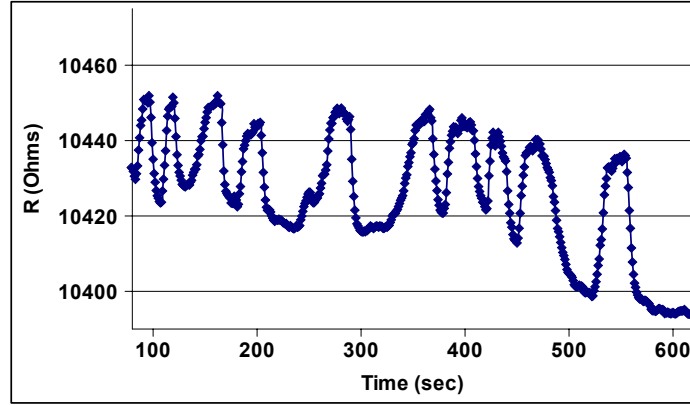
- Type I - where the wind velocity is varied continuously, usually going from minimum to maximum and back.
- Type II- where the wind velocity is *gradually* increased from the minimum (0) to the maximum velocity and then gradually reduced back to zero.

The results of both sets of the experiments are shown in this section, followed by a detailed analysis of the performance of both types of devices described here, in the next section. The focus in this section is more on the 1.5mm x 0.4 mm device, rather than the 3.5mm x 2.2 mm device since the former has a much higher sensitivity and because the application requires miniaturized microtufts.

Multiple experiments are performed, both for Type I and Type II experiment types. The results of four representative experiments are shown in Figures 72, 73, 74, 75, of which 2 are Type I and 2 are Type II experiments. All experiments are conducted with the device described in Figure 71. All the tests are conducted on the



(a) Wind flow profile in the wind tunnel



(b) Resistance profile of the device corresponding to the wind flow

**Figure 70:** 3.5mm x 2.2 mm tufts with silicon nitride-device response

same device and one of the main reasons for that lies in the fact that the electrical behavior of the composite elastomer depends on cycling of strain. This effect was discussed in much greater detail in Section 6.2.2. Four different experiments are shown to demonstrate the effect cycling has on the device response. Table 27 summarizes the effect of cycling on the resistance of the device.

As was observed in Section 6.2.2, the piezoresistive gage factor does depend on cycling to a certain extent.

The performance of the device is analyzed in more detail in the following section.

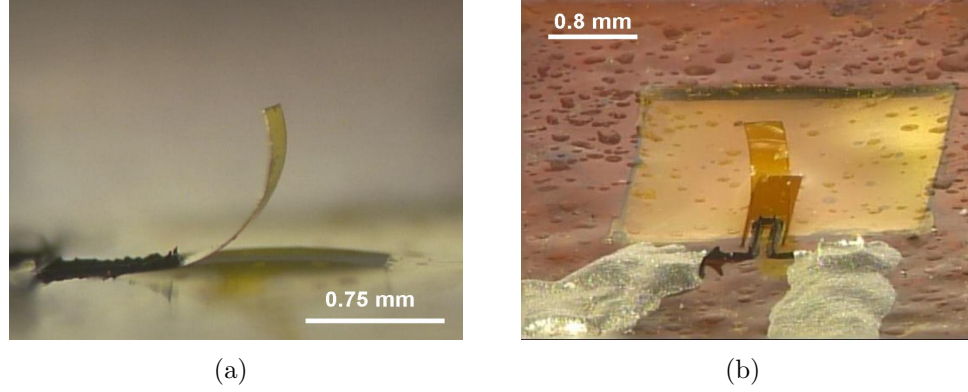


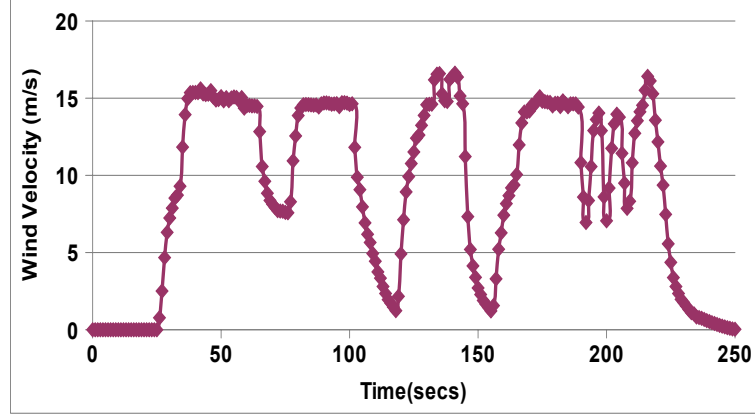
**Figure 71:** Final device pictures of the 1.5 x 0.4 mm test devices showing the pronounced curvature. The devices are fabricated using Kapton<sup>®</sup> 30HN (7.6  $\mu\text{m}$ )

#### 6.4.2 Analysis of device performance

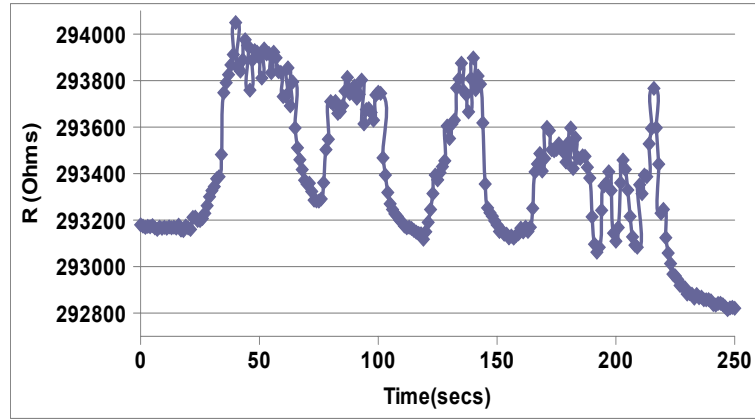
Both devices tested, the 3.5mm x 2.2mm device, as well as the miniaturized 1.5mm x 0.4 mm microtuft, show similar behavior, as far as following the wind velocity profiles are concerned. The only experiment done on the larger device is a Type I experiment as described above, whereas the miniaturized tufts have been subjected to both Type I and Type II tests. In this section, an analysis of the device sensitivity to wind flow and the hysteresis behavior is analyzed.

##### 6.4.2.1 Device sensitivity

Table 26 summarizes the sensitivity of all the devices (nitride and oxide based) tested for both Type I and Type II experiments. Sensitivity here is defined as the ratio of the change in the measured device resistance to the corresponding change in airflow velocity. As is apparent from the data shown in Table 26, the 3.5mm x 2.2 mm devices that are fabricated using 16.5  $\mu\text{m}$  thick Kapton<sup>®</sup> have a very low sensitivity. This is because of a combination of high rigidity of the structure (due to both the geometry as well the thickness) and due to a low flow-structure interaction/curvature, as shown in Figure 69(b). Since the ultimate goal is to fabricate sensors with high flow sensitivity and ultra-miniaturized size, this device is not an ideal choice.



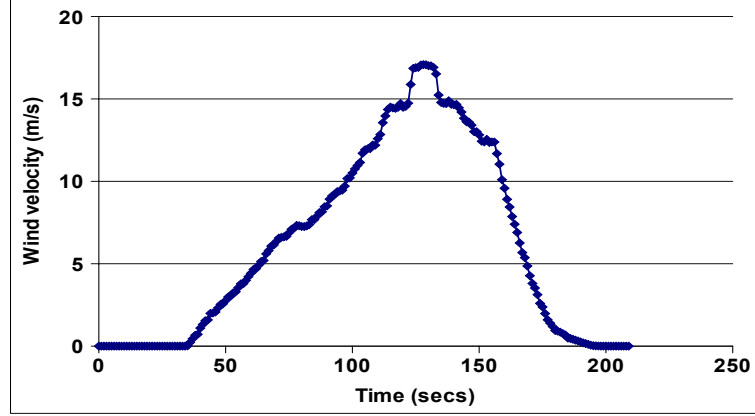
(a) Wind velocity profile measured by the reference sensor



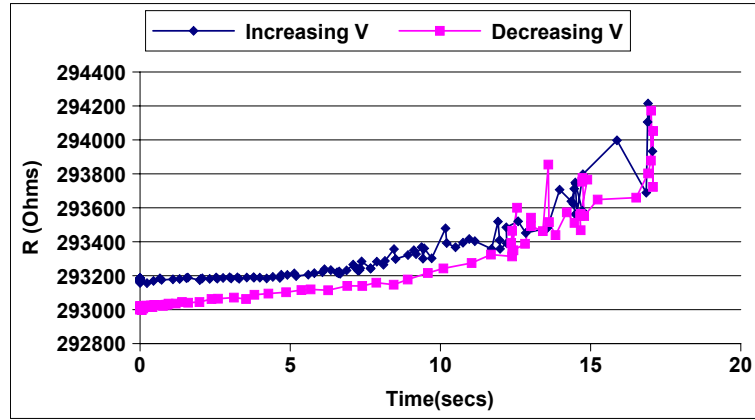
(b) Corresponding resistance profile of the device measured by the digital multimeter

**Figure 72:** Experiment # 1 - 1.5mm x 0.4 mm microtufts-device response to Type I experiment

The 1.5mm x 0.4mm microtuft fabricated using 7.6  $\mu\text{m}$  Kapton<sup>®</sup>, provides a significant improvement in device performance with an average sensitivity of 59  $\Omega/\text{m/s}$  (based on Type II experiments). This high sensitivity is due to a structure with low rigidity (because of geometry as well as thickness of the Kapton<sup>®</sup>) and high curvature due to the deposition of high compressive stress oxide, as shown in Figure 67(d). The high sensitivity is also attributed to the high gage factor of the carbon-black elastomer reported in Section 6.2.2. The extremely high sensitivity compares favorably with similar microcantilever based flow sensors reported in literature. Wang



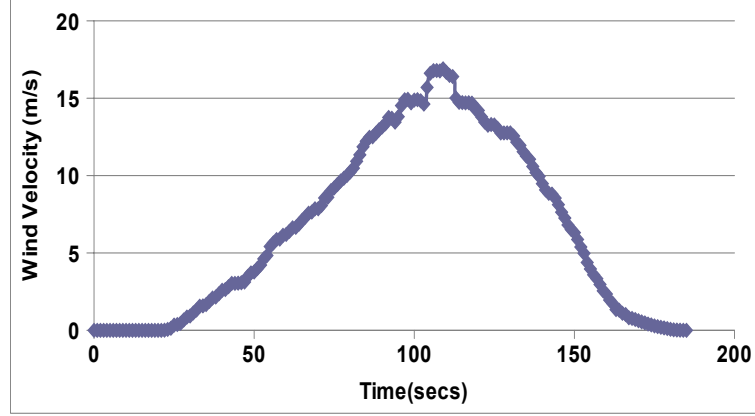
(a) Wind velocity profile measured by the reference sensor



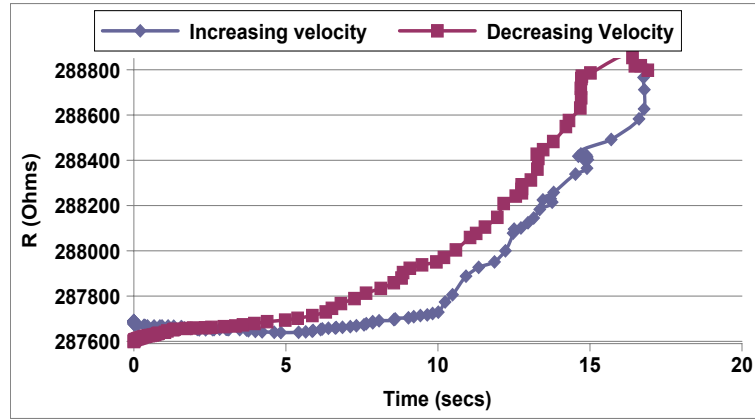
(b) Corresponding resistance profile of the device measured by the digital multimeter

**Figure 73:** Experiment # 2-1.5mm x 0.4 mm microtufts-device response to Type II experiment. (the same device as in experiment # 1 is used)

et.al. report the fabrication of a  $\text{Si}_3\text{N}_4$  microcantilever based flow sensor using platinum piezoresistors with a maximum sensitivity of  $0.0284 \Omega/\text{m/s}$  [103], which is much lower than sensitivities for reported in this section. This again, is probably due to the fact that focus has always been on fabrication of silicon based MEMS flow sensors with little attention being paid to polymer MEMS based flow sensors. Although Kapton<sup>®</sup> is a widely used material, it has mainly been utilized for the fabrication of flexible substrates and PCBs, with relatively small amount of work involving Kapton<sup>®</sup> as a structural material.



(a) Wind velocity profile measured by the reference sensor

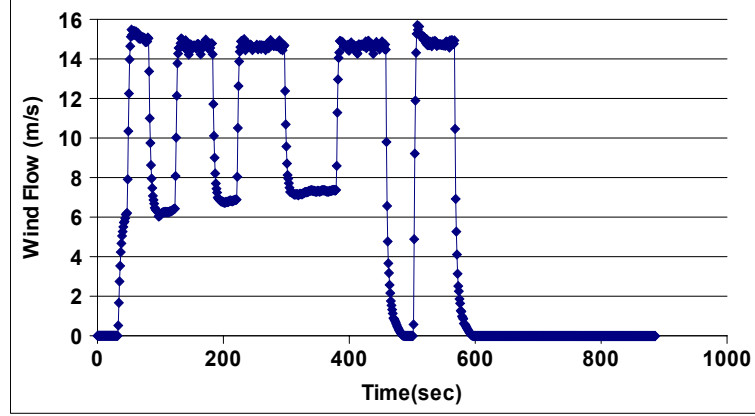


(b) Corresponding resistance profile of the device measured by the digital multimeter

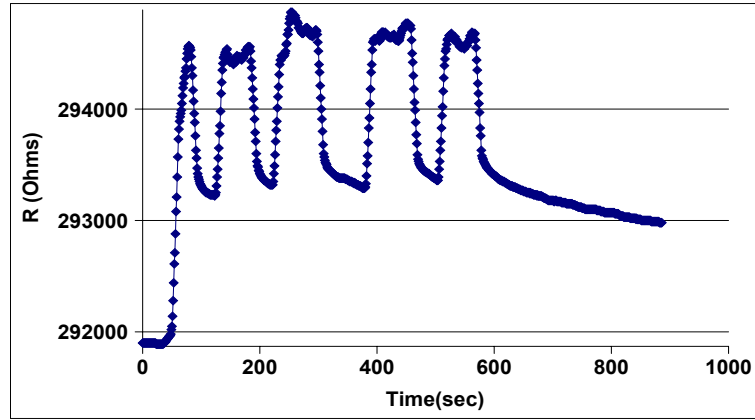
**Figure 74:** Experiment # 3-1.5mm x 0.4 mm microtufts-device response to Type II experiment. (the same device as in experiment # 1 is used)

#### 6.4.2.2 Hysteresis and resistance drift

At first glance, it seems that the hysteresis seems to depend on the type of experiment being conducted. The % hysteresis for Type I and Type II experiments conducted on the 1.5mm x 0.4mm device are summarized in Table 27. The results seem to indicate that cycling does have an effect on the behavior of the device, though it is not clearly understood. Section 6.2.2.2 talks about hysteresis in filled elastomer composites in more detail. Nevertheless, the drift and hysteresis observed are undesirable from the point of view of the sensing application. During the testing, the hysteresis is observed not only between values at the beginning and end of a single experiment, but also



(a) Wind velocity profile measured by the reference sensor



(b) Corresponding resistance profile of the device measured by the digital multimeter

**Figure 75:** Experiment # 4-1.5mm x 0.4 mm microtufts-device response to Type I experiment. (the same device as in experiment # 1 is used)

between experiments that are conducted days apart as indicated by the data in Table 27. Apart from an inherent piezoresistance, filled elastomers also exhibit an intensive positive temperature coefficient of resistance (PTC) [111], in which an abrupt increase in the resistivity results from temperature increases. Although, PTC and piezoresistance are two completely different properties, they can both be attributed to the changes in the microstructure of the carbon-black in the elastomer. This could be one of the reasons why the resistance at the start of every experiment is different. Since the experiments are spanned across several days, changes in temperature could cause such variations in the resistance.



**Table 26:** Sensitivity analysis for Type I and II experiments

#	Expt. Type	Device (mm x mm )	Maximum $\Delta$ in R ( $\Omega$ )	Maximum $\Delta$ in flow (m/s)	Sensitivity ( $\Omega/\text{m/s}$ )
1	I	3.5x2.2	34.95	14.733	2.37
2	I	1.5x0.4	761.9	14.72	52.26
3	II	1.5x0.4	881	17.08	51.58
4	II	1.5x0.4	1115	16.9	65.96
5	I	1.5x0.4	2580	15.70	164.28

**Table 27:** Resistance variations with experiments, for 1.5mm x 0.4mm microtufts.  $R_i$ ,  $R_f$  are the device resistances before and after the wind tunnel experiment. Hysteresis is defined as  $R_i - R_f$ . The % hysteresis is calculated with respect to the initial resistance

Expt. #	$R_i$ ( $\Omega$ )	$R_f$ ( $\Omega$ )	Hysteresis ( $\Omega$ )	% Hysteresis
1 (Type I) Day 1	293179.7	292795.1	384.6	0.131
2 (Type II) Day 2	293171.5	293002	169.5	0.05
3 (Type II) Day 6	287683	287599	84	0.029
4 (Type I) Day 9	291900	292980	-1080	-0.367

Drifts in resistance are also observed while using metal thin film piezoresistors and doped silicon piezoresistors. But in most cases, the drift in such piezoresistors is essentially due to a high temperature coefficient of resistance (TCR) of the piezoresistor material, because of which the device resistance drifts with slight changes in the ambient temperature. Drifts, such as this and to due to some other reasons are easily compensated for by using a *differential measurement* that cancels out all the common mode effects. The **Wheatstone bridge** is a very popular technique for drift compensation. But, one of the basic requirements of a Wheatstone bridge is that all the elements in the bridge must be subjected to “cause of the drift”. But in the case of the filled elastomer piezoresistors, such *common mode effects elimination* is meaningless, since the effects seen are highly dependent on the strains applied and

on strain cycling. Thus, drift compensation is an important avenue that must be addressed to improve the performance and make the device more robust.

However, the relatively high piezoresistive gage factor of the piezoresistor ensures that the output response (change of resistance) is so high ( $\sim 60 \text{ } \Omega/\text{m/s}$ ), that no external circuit is required to modify or amplify the signal. This is a big advantage over other flow sensors, especially metal thin film and silicon based flow sensors that require complex circuitry for signal amplification or drift compensation purposes.

### ***6.5 Stress induced curvature - Intrinsic or thermomechanical stress?***

PECVD silane based oxides have been widely applied in fabrication of MEMS devices and components for both electrical and mechanical functions [22]. In a lot of the applications involving PECVD oxide, a stress-induced bowing of the substrate or stress-induced degradation of the device occurs, suggesting the presence of residual stresses whenever silicon dioxide is deposited.

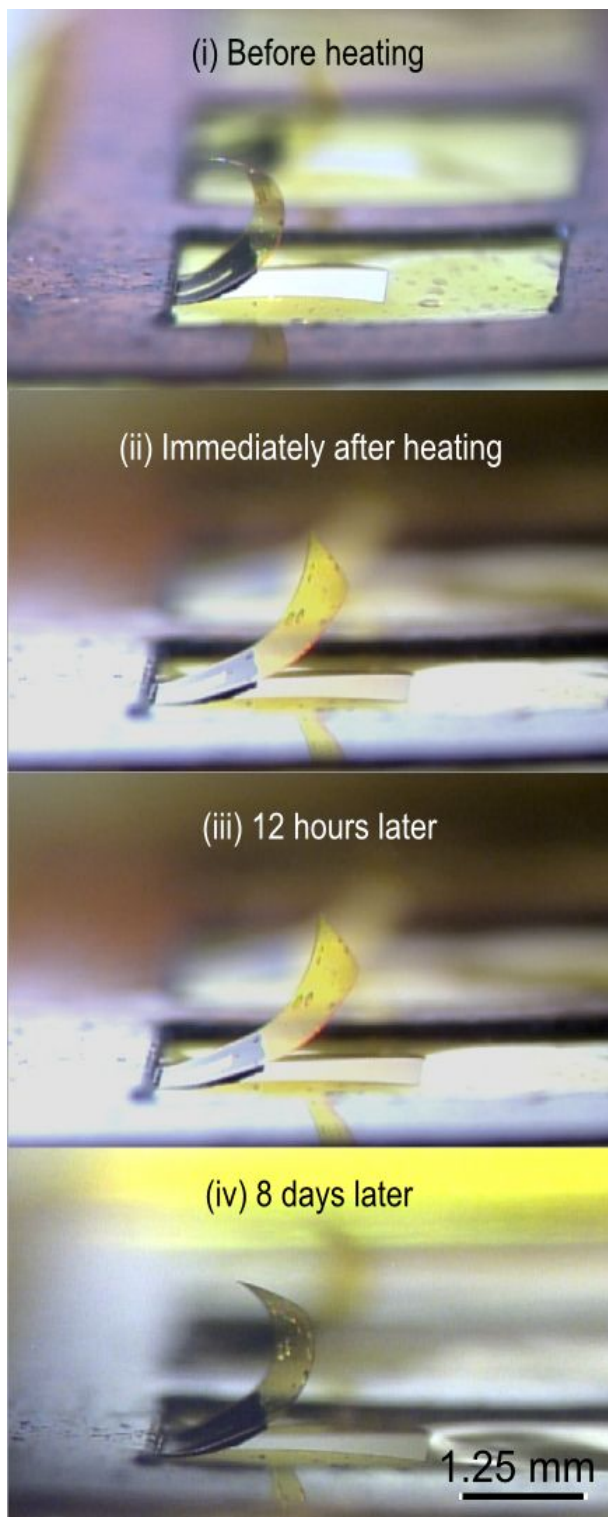
While in majority of the cases, the stress-induced by the oxide is undesirable, in cases like this research and others [102], this stress is a necessary phenomenon for increasing the device sensitivity. In general, the residual stresses can be decomposed into thermal and non-thermal stresses. The non-thermal component is known as the *intrinsic stress*. The thermal stresses arise due to a CTE mismatch between the oxide and the substrate. When the bimorph structure (oxide and Kapton<sup>®</sup>) is cooled from the temperature of deposition to room temperature, both materials contract, but at different rates. This difference in contraction rates creates residual stresses. Intrinsic stresses in the oxide film could also contribute to the residual stress, but little is known about it, except that it is closely related to the deposition parameters [72] and is intimately linked to the nucleation and growth of the film [1]. After a complete thermal cycle, the net change in the thermal stresses should be zero, if there has been no change in the thermomechanical properties of the materials. Therefore, any

hysteresis in the residual stresses in the structure, indicate a change in the intrinsic stresses in the film. Thermal cycling experiments are thus very useful in determining the contributions of thermal and non-thermal stresses to the total residual stress in the structure [22].

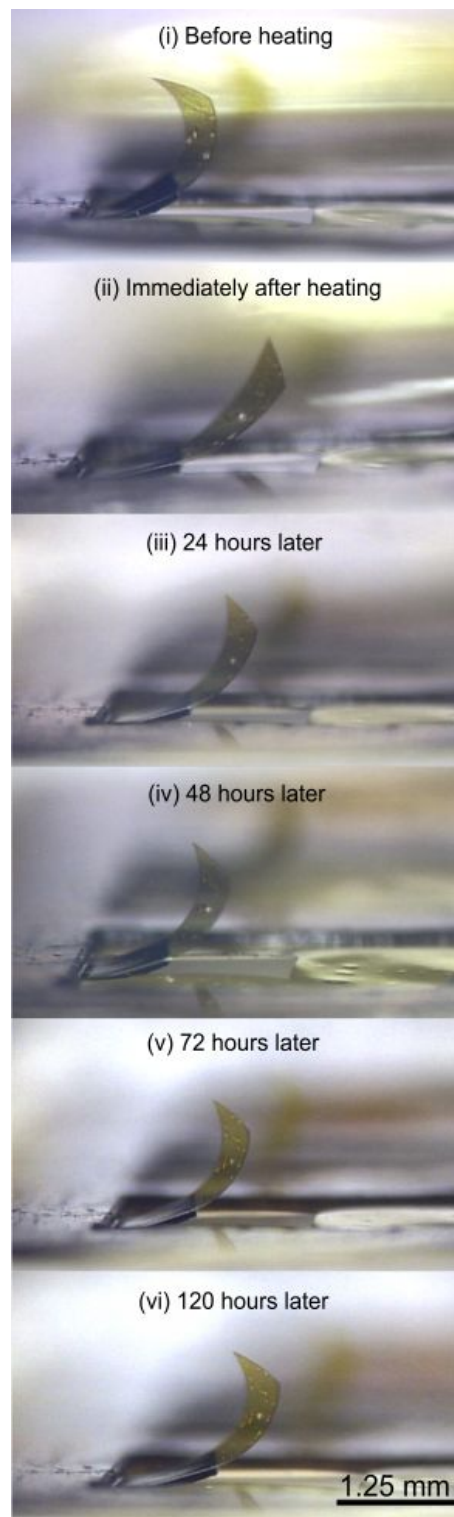
In this section, the results of a set of thermal treatment experiments are presented. Possible causes of the residual stress induced curvature are merely speculated and further experiments need to be performed to build on the speculations presented and that is left as an exercise for the future.

The thin oxide film on the Kapton<sup>®</sup> system can be considered as a bimorph cantilever. It is important to understand that any curvature in the structure is due to a bending moment caused by a stress gradient across the thickness of the two films in the bimorph cantilever. This stress gradient created is due to the residual stresses in the films, as explained before. If it is assumed that the entire residual stress is caused by CTE mismatch alone, then thermal cycling should have no effect on the final curvature of the structure. This assumption, of course, is only valid if the CTE of the materials do not change with thermal cycling and if the effects of polymer creep are neglected. In order to investigate if the above assumption is valid, the sample with the original (as obtained after release) curvature is placed on a 160<sup>0</sup>C hotplate for about 20 minutes. The substrate temperature during the PECVD deposition of the oxide was 150<sup>0</sup> C and the deposition time was 20 minutes. A slightly higher temperature is used to account for heat losses due to convection and radiation while using a hotplate in an open atmosphere. Figure 76(a) shows the photomicrographs of a 2.5mm x 1.2 mm sample of Kapton<sup>®</sup> 30HN (7.6  $\mu$ m thick) that has undergone the above thermal treatment. A second experiment is performed on the *same sample* at a later date (about 12 days later), but this time, using a 150<sup>0</sup>C convection oven. Figure 76(b) shows the results of this experiment.

The observations from the two experiments are summarized as follows:



(a) Experiment #1 performed on a 160°C hotplate



(b) Experiment #2 performed in a 150°C convection oven

**Figure 76:** Heat treatment experiments of Kapton® with oxide. Both experiments were performed on the same sample with a thickness of 7.6  $\mu\text{m}$ . The test in Figure (b) was conducted after the one in Figure (a))

**Experiment #1:** First thermal treatment of the sample conducted on a hotplate

- Figure 76(a)(ii) shows the picture of the sample taken immediately after removing from the hotplate. The curvature is reduced and much lower than what it was originally before the heat treatment.
- Figure 76(a)(iii) shows a picture taken after 12 hours and the curvatures seem unchanged.
- Figure 76(a)(iv) shows a picture taken after 8 days. The curvature has increased dramatically compared to Figure 76(a)(iii), but is still less than the original curvature.

**Experiment #2:** Second thermal treatment of the same sample conducted in a convection oven.

- Figure 76(b)(ii) shows the picture of the sample taken 30 minutes after removing from the oven. The curvature is reduced and much lower than what it was originally before the heat treatment, as in Experiment # 1.
- Figure 76(b)(iii) shows a picture taken after 24 hours and the curvature has slightly increased.
- Figures 76(b)(iv),(v) and (vi), taken 48 hours, 72 hours, 120 hours after the heat treatment respectively, all show almost the same curvature. Differences in curvature, if any, could not be discerned using the stereoscope.

There is not much information to be gathered from experiment # 1 since pictures were not taken at regular intervals because the above described behavior in Experiment # 2 was not expected. Hence the *saturation* of the curvature could not be captured. But curvatures in Figure 76(a)(iv) and Figure 76(b)(i) seem almost the

same, indicating that a saturation of the curvature does occur after a certain period of time. Experiment # 2 suggests that after a period of 48 hours, the curvature does not increase any longer. At least, there does not seem to be a dramatic change in the curvature. Some of the conclusions that can be drawn are as follows:

- In both experiments, the final curvature at the end of the experiment is always less than the original curvature before the experiment, for the period of time over which the pictures are taken (8 days and 120 hours respectively). Thus, the curvature of the structure at end of experiment # 2 is less than at the beginning and this curvature in turn, is less than the original curvature before experiment # 1 was conducted. But, these inferences are drawn, based on an observation of the optical images alone and are not a qualitative analysis.
- Irrespective of the original curvature, the curvature immediately after heating for 20 mins seems the same for both experiments. Again, an accurate confirmation can be drawn only after a more detailed inspection.
- In both cases (although this cannot be confirmed from Experiment #1), sufficient time is required for the curvature to rise after heating.
- The curvature never drops to zero on heating, in either case.

From these basic experiments, it can almost certainly be concluded that there is a decrease in the net residual stresses in the structure that causes a corresponding decrease in the bending moment induced curvature. It can also be concluded that CTE mismatch induced stress alone is not responsible for the curvature. If it were so, the curvature should have dropped to zero on heating to the temperature of deposition (150 °C) and recovered back to its original form on cooling to room temperature. Neither of these two phenomena are observed. What cannot be identified is the source of the stress reduction and thus the source of the curvature produced in a sample

which has not seem any thermal treatments. It is probable that the curvature could be produced by a combination of the intrinsic and the thermal stress, especially given the fairly large CTE mismatch (CTE of Kapton<sup>®</sup> is 16-20 ppm/<sup>0</sup>C vs 0.5 ppm/<sup>0</sup>C for silicon dioxide). But the reduction of the residual stress even after bringing the sample back to room temperature and the hysteresis in the residual stress with thermal cycling (indicated by different curvatures each time), seems to indicate a change in the intrinsic stress of the oxide alone. Thus, the three important questions that arise at this point are:

1. Why does the curvature decrease at the end of a thermal cycle (heating to 150<sup>0</sup>C and then cooling to room temperature)?
2. Why does the recovery of the curvature to its final equilibrium state take such a long time?
3. Why is the curvature in the final equilibrium state always lesser than what it was before that thermal cycling experiment and progressively lesser for further thermal cycling experiments? Or do the curvatures recorded correspond to the final equilibrium state at all?
4. Is the hysteresis (if any at all) caused due to changes in the oxide film or the polymer?

Chen et.al. [22] have investigated the intrinsic stress generation and relaxation of PECVD oxides based on a silane-nitrous oxide chemistry (same as what is used in this research) and the effects of thermal cycling. The films they have investigated are deposited at a temperature of 400 <sup>0</sup>C, with thicknesses of 3, 10 and 40  $\mu$ m. Their thermal cycling experiments indicate that the original residual stress in the oxide films are compressive and higher for the 3  $\mu$ m films than the 10  $\mu$ m films (-225 MPa vs -125 MPa) and even lower for 40  $\mu$ m films. Their experimental results are summarized in Figure 77.

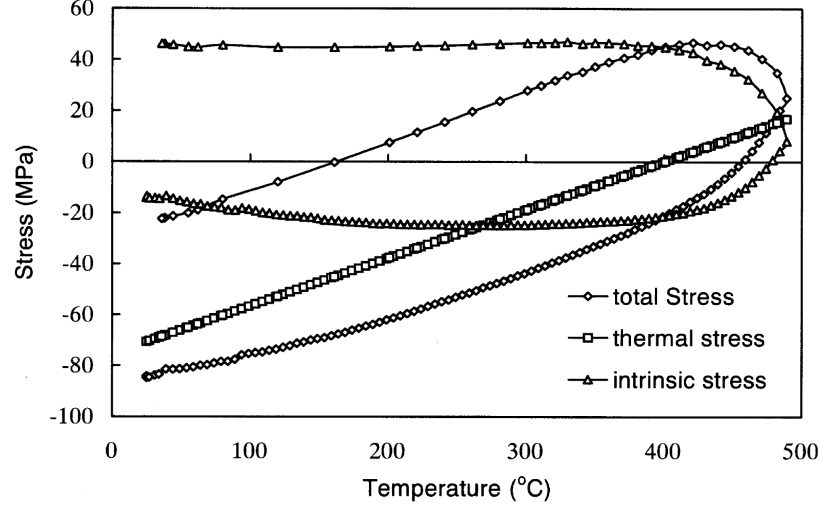


**Figure 77:** Decomposition of stress into its components for 40  $\mu\text{m}$  oxide films. Intrinsic stress is obtained by subtracting the thermal stress from the measured stress. (Chen et.al. [22])

According to the graph plotted by Chen et.al., shown in Figure 77, during thermal cycling at lower temperatures the intrinsic stress is essentially unchanged. However, as temperature increases nearly to the deposition temperature (400  $^{\circ}\text{C}$ ), the compressive stresses start reducing rapidly and it ultimately becomes tensile beyond a certain temperature. There is a profound hysteresis in the intrinsic stress even after bringing the sample back to room temperature. The thermal stress on the other hand behaves as expected with no hysteresis at all. This experiment is a clear indication that the changes in the residual stresses after thermal cycling are solely due to changes in the intrinsic stress of the oxide film, for films heated to 400  $^{\circ}\text{C}$ . It has also been suggested that the intrinsic stress in the films depends to a large extent on the thickness of the films and the deposition conditions. The reasons behind the behavior of the intrinsic stress will not be discussed in this analysis.

Given the observations of Chen et.al., a rough analogy can be drawn with the observations made in the case of the thermal treatments of oxide on Kapton<sup>®</sup>. However, Chen et.al. deposit their films on silicon and it is not known at this point how



the CTE of Kapton<sup>®</sup> changes with temperature and thermal cycling. But the assumption of zero net changes in the CTE mismatch stress is assumed. A very critical observation from Figure 77 is the fact that the intrinsic stress starts decreasing when the temperature *nears the temperature of deposition*. This could possibly suggest that the same mechanisms that cause a decrease in the compressive stress and thus the intrinsic stress in the case of Chen et.al., could also be causing a decrease of the compressive intrinsic stress of the oxide on Kapton<sup>®</sup>, since the thermal treatment here is also done at the deposition temperature (150 °C). And this is possibly manifested as a corresponding decrease in the curvature of the cantilever. The hysteresis of the oxide stress reported also correspond with the results that are reported here and this is manifested by a reduced curvature of the cantilever compared to the original curvature, at the end of *every* thermal cycling experiment. However, the large irreversible changes seen at 400 °C may or may not be seen at 150 °C, given the differing deposition temperatures of the two films. Thus, confirmation of the exact phenomena causing this behavior would require more experiments that are pertinent to the system that we are dealing with (oxide on Kapton<sup>®</sup> vs oxide on silicon). Chen et.al. have also reported the effects of thermal cycling on the residual stresses in the oxide films. They claim that a large hysteresis in the residual stress is observed at the end of the very first thermal cycle and this hysteresis is significantly reduced for subsequent cycles. However, the thermal cycling experiments performed for the case of oxide on Kapton<sup>®</sup> are not conclusive enough at this point in time, to draw any analogies with the thermal cycling behavior reported by Chen et.al.

The time dependent behavior of the curvature after thermal cycling is another conundrum. Haque et.al. have reported the residual stress behavior of thin PECVD oxide films as a function of storage time [41]. They report that the stresses in oxide films gradually change with time, with the compressive stress first increasing and then ultimately decreasing and saturating at a certain value (Figure 78). The increasing

compressive stress with time is in correspondence with the fact that the curvature recovery phenomena of the Kapton<sup>®</sup> cantilever is also time dependent, but there seems to be a slight difference in the time scales over which this increase takes place. But, the increase in the tensile stress of the oxide film, as reported by the authors, is not clearly understood. Haque et.al. however have not conducted thermal treatment experiments in conjunction with the storage time analysis of the oxide films and thus it is very difficult to draw any concrete conclusions about the phenomena observed in this research.

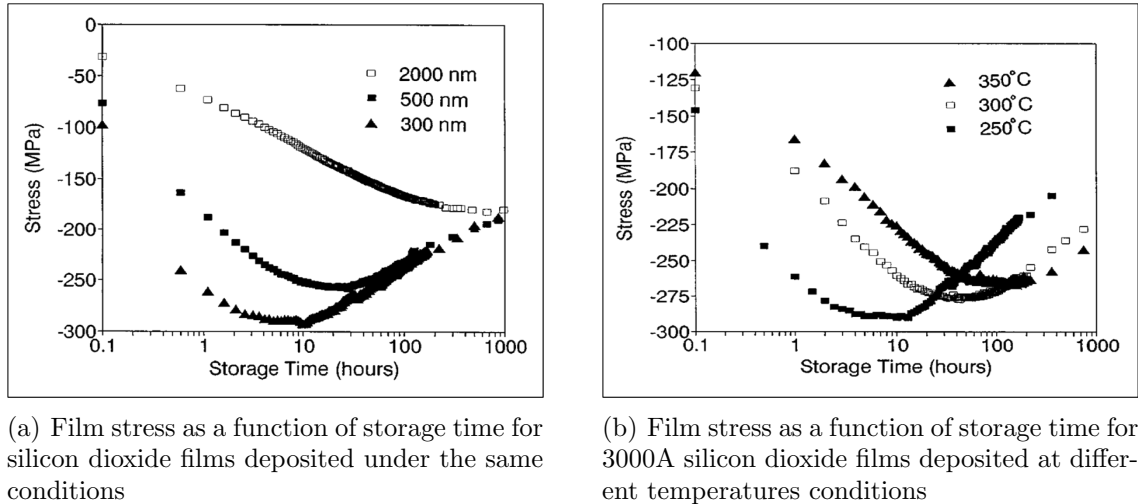


**Figure 78:** Film stress in silicon dioxide as a function of storage time (Haque et.al. [41])

The other explanation for the time dependent curvature recovery behavior might lie in the material properties of the Kapton<sup>®</sup> itself. Most polymers are known to be viscoelastic and thus exhibit *creep*, which is the continuous change in the strain under a constant load. It also happens to be a temperature dependent property, as shown in Figure 79. Hence, it is possible that the thermal treatment affects the polymer as well, causing it to creep. This in turn could have a bearing on the rate of change of the residual stress. It is unknown, however, exactly how the creep behavior of the Kapton<sup>®</sup> impacts the residual stress. In order to verify this, the time scales over

which the pictures are taken must be increased. If polymer creep is the only reason for the hysteresis and it is a reversible effect, after a finite period of time (unknown at this point), the final equilibrium curvature and the curvature before the thermal treatment experiment, must be the same.

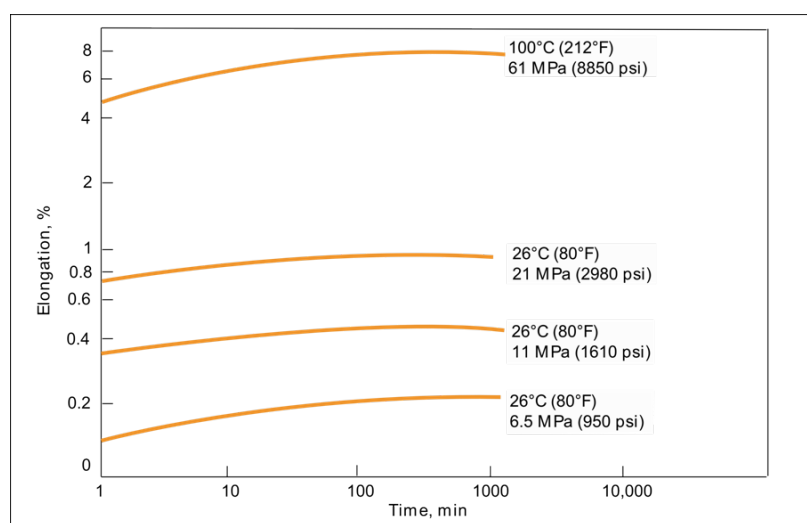
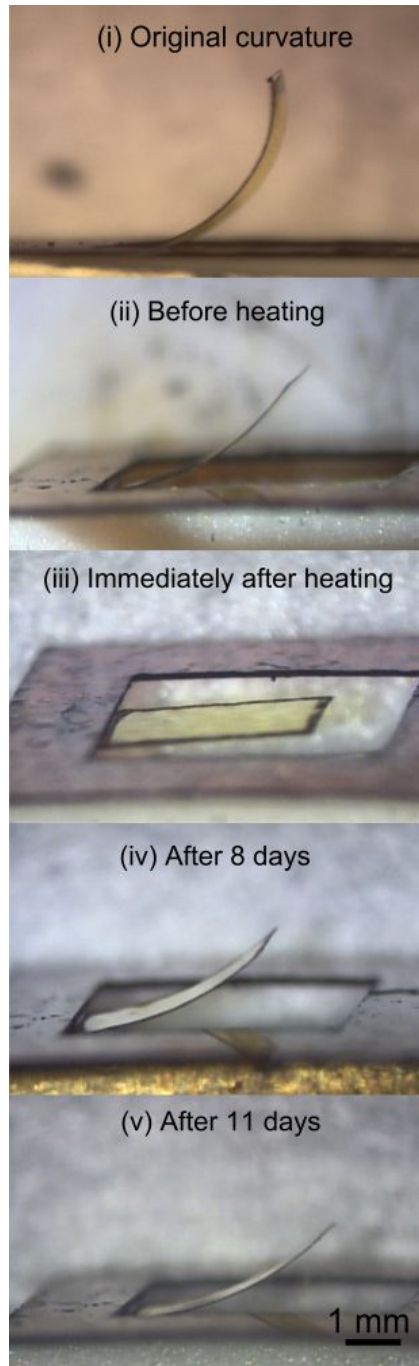


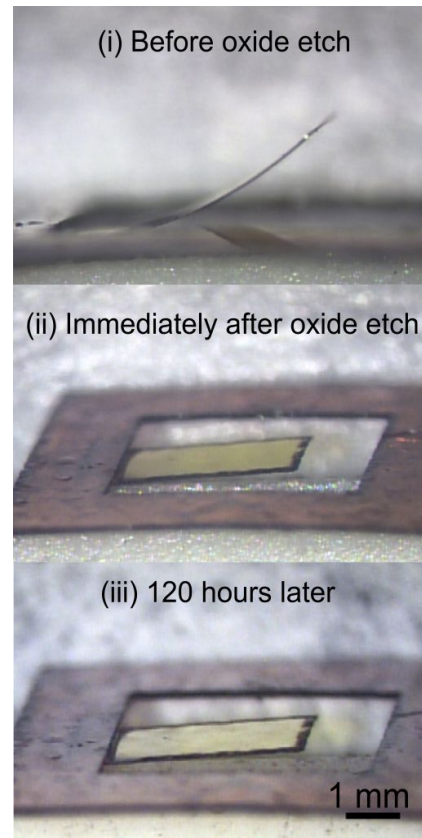
**Figure 79:** Tensile creep properties of Kapton® Type HN films (obtained from Dupont)

A similar study is performed on 3.5mm x 2.2mm Kapton® 65E sample (16.5  $\mu\text{m}$  thick), the results of which are shown in Figure 80(a).

Figure 80(a) shows the usual thermal treatment experiment as in the case of Kapton® 30HN. A similar behavior is observed in this case too, only this time, the curvature drops to zero. This is possibly due to a significant difference in the rigidity of the structures described in this section. The Kapton® 65E sample has rigidity of 0.1441 N/m, while the Kapton® 30HN sample has a rigidity of 0.0211 N/m. The net reduction in the residual stresses in both cases should theoretically be the same, but it corresponds to different curvatures, because of this difference in rigidities. The net residual stress in the case of the Kapton® 65E sample, immediately after heating, is probably not enough to create an appreciable bending moment and thus the structure remains flat. In Figure 80(b), the oxide film on the same Kapton® 65E sample is



(a) Thermal treatment experiment on a hot plate at 160°C for 20 mins



(b) Effect of etching the oxide film in BOE for the same sample as in Figure(a)

**Figure 80:** Investigation of residual stresses in a 3.5mm x 2.2 mm Kapton® 65E (16.5  $\mu\text{m}$  thick) with 1  $\mu\text{m}$  thick oxide layer. Figure 80(a)(i) is the original curvature of the structure before any thermal treatment. Figure 80(a)(ii) is the final curvature at the end of the first thermal treatment

etched away using a 6:1 buffered oxide etch (BOE) solution in water (J.T. Baker) for about 10 minutes. On etching the oxide away, the Kapton<sup>®</sup> 65E cantilever never recovers its curvature. It must be mentioned here, that the results shown here are for a *second annealing treatment*. In other words, the sample has already seen a thermal treatment step once before and Figure 80(a)(i) is the curvature of the original bimorph cantilever, before any thermal treatment.

In conclusion, the preliminary study of the source of the residual stresses that cause the curvature of the Kapton<sup>®</sup> cantilever seems to indicate that the intrinsic stress in the oxide has an important role to play. The time dependent curvature recovery after thermal treatment could be due to the storage time effect on the residual stresses reported by Haque et.al [41]. There is small possibility that creep of the Kapton<sup>®</sup> might also be responsible for this behavior, especially if heat treatment causes an irreversible change in the viscoelasticity of Kapton<sup>®</sup>. The hysteresis in the curvature, if it is confirmed to exist, could possibly be due to a suspected hysteresis in the oxide intrinsic stress after every thermal treatment or due to polymer creep or both. This can be confirmed by increasing the time scales over which the recovery of curvature is studied. Further experiments must however be conducted to investigate any special effects that could possibly occur because of the unique oxide-polymer system involved. A detailed analysis of how the intrinsic stress varies with thermal cycling would involve curvature tests of silicon dioxide on silicon as well as Kapton<sup>®</sup>. One more important point to consider is the fact that the comparison of the curvatures of the Kapton<sup>®</sup> cantilevers at various points in time is a visual process and not quantitative in nature. This could lead to significant errors in interpretation of the phenomena observed. Thus future experiments must be conducted such that a quantitative measure of the curvature can be obtained. At the very least, if quantitative measurements of the curvature cannot be made, care must be taken to ensure that all photomicrographs (of different curvatures) are taken under the same conditions of tilt, zoom and focus

to avoid misinterpretation of the phenomena observed.

Because of the above mentioned complications observed, the oxide is always deposited *after* processing and curing the conductive elastomer, which is cured at a temperature of about 130°C, which, in turn, is close to the deposition temperature of the PECVD oxide. Thus, the oxide, once deposited, does not see any thermal treatments which could potentially cause any thermal cycling or temperature dependent curvature.

## CHAPTER VII

### CONCLUSION

#### *7.1 Summary and contributions*

The research objective of this thesis was to develop a mass fabrication technique capable of fabricating arrays of piezoresistive MEMS flow sensors with high sensitivities and on a flexible substrate. In this work, existing processes were modified and explored and other fabrication techniques were developed to demonstrate the feasibility of using polymer MEMS technology for achieving the above.

The first portion of the thesis was dedicated to the development of the existing metal transfer micromolding (MTM) process to suit the needs of the application. A PDMS to PDMS MTM process was used to fabricate arrays of all-elastomer sensor with thin film gold piezoresistors. A “substrate SU-8” process was developed involving three layers of spun coat SU-8, of which the bottommost layer also functioned as a “substrate”, to address the common problem of delamination of the SU-8 from the glass substrate due to thermomechanical stresses. Static deflection tests were conducted to study the response of individual sensors that yielded an average change of resistance of about  $0.8\ \Omega$  for a deflection of about  $8.75\ \mu\text{m}$ . But there was also a fairly large hysteresis in the device response and the results could not be repeated with the other devices that were part of the same fabrication batch. It was concluded that the microcracking of the metal thin film during the fabrication process lead to poor response of the devices.

The next section of the thesis was dedicated to the development of a fabrication technique that addressed the problem of microcracking of thin metal films on elastomeric substrates. The source of the microcracking was identified as the final

demolding step in the MTM process and this step was thus eliminated by using a sacrificial dissolving mold in place of the conventional PDMS one. Two types of dissolving molds were investigated, one of which was an organic solvent based PMMA mold and the other was a water based PAA mold. The incorporation of the dissolving mold required very small modifications of the existing MTM process, with a dramatic increase in device yields. The lower device resistances obtained from the process (7-9  $\Omega$  vs 106-108  $\Omega$ ), was a clear indication of the metal quality. The devices fabricated were tested in a benchtop wind tunnel and yielded a sensitivity of about 1m $\Omega$ /m/s. But, a similar hysteresis was observed for these devices, as with the MTM devices, that lead to the conclusion that microcracking and especially warpage of the metal films was almost inherent to thin metal films on elastomeric substrates. The “waves” formed due to the warpage, possibly undergo extension and relaxation during device testing, and this process may have induced a hysteresis in the response. It is believed that, although the dissolving mold process is marked improvement over the MTM process for the current application, the irreproducibility of results is due to phenomena that are inherent to thin film metal-elastomer systems.

In the final experimental section of the thesis, a laser based technique is developed that uses a conductive composite carbon-black elastomer piezoresistor. The use of the conductive composite, eliminates the need for metal thin film based piezoresistors and avoids the complications associated with microcracking etc., as discussed above. The material itself is tested for its mechanical and electrical properties and it is estimated that it has a low Young’s modulus of about 1.7 MPa and a very high piezoresistive gage factor of about 7. The flow sensor itself, consist of *microtufts* that undergo deflection in the presence of airflow and this deflection (and thus the airflow) is sensed piezoresistively, due to the carbon black to carbon black inter-particle distance changing with applied strain. The flow-structure interaction is increased by the deposition of PECVD silicon dioxide that produces a stress-gradient induced curvature. The



devices fabricated using this technique show a high sensitivity of about  $60 \text{ } \Omega/\text{m/s}$ . The results are fairly reproducible, but the response is characterized by a resistance hysteresis and drift, which could possibly be due to the viscoelastic properties of the elastomer leading to “resistance creep”. An array fabrication is also proposed and partially demonstrated that would enable the sensing of device response using *backside interconnects*, causing minimum intrusion with the flow.

The overall contribution of this thesis is summarized below:

- Development of a modified metal transfer molding approach using PDMS to PDMS metal transfer for the fabrication of an all elastomer device.
- Development of a dissolving mold process with PMMA and PAA as sacrificial dissolving molds. This process could possibly open up avenues for the fabrication of all elastomeric devices with electrical functionality, where minor device resistance variations (as was observed in the flow sensors) are not critical to the application. One such application could be in the area of locomotion sensing of biological organisms, using a similar transduction scheme demonstrated by Klejwa et.al. [56].
- Successful integration of laser fabrication and MEMS technology for the fabrication of a microtuft based flow sensor, using piezoresistive materials with high gage factor. This technique extends the range of Polymer MEMS by increasing the obtainable device sensitivities. The use of elastomers greatly enhances the mechanical capabilities of polymer MEMS, achieving rigidities that are difficult to obtain with silicon.

## 7.2 *Future work*

The metal transfer molding related techniques (both MTM and the dissolving mold) are believed to be useful in the fabrication of all elastomeric devices with electrical functionality, where hysteresis and drift of resistance are not too critical to the application.

The laser based fabrication of microtufts has multiple avenues along which the work can progress. And these are summarized as follows:

- The drift and resistance hysteresis behavior have been reported by other groups [69], who have tried to develop algorithms to minimize these phenomena. These algorithms or its modifications can be implemented here for signal conditioning purposes.

Bulk of the work has to be done towards the development of array based sensors.

- Initial results have shown that photolithography on Kapton<sup>®</sup> can be successfully used to pattern resist and subsequently plate copper electrodes to sense the response of the piezoresistors. However, the metal adhesion, at this point, is weak and severe delamination occurs after processing. Thus, improvement of metal adhesion on Kapton<sup>®</sup> is an important area of study.
- Better alignment schemes have to be developed to reduce alignment errors during both, the microstenciling step, as well as the final step involving the release of the microtuft structures by excimer laser ablation.
- To convert the fabrication scheme developed into a batch process for simultaneous release of all the microtufts, a plasma based reactive ion etching (RIE) approach for the etching of the Kapton<sup>®</sup> polyimide must be investigated [99].
- Further miniaturization of the microtufts must be investigated. The smallest microtufts fabricated in this research have a length of 1.5mm and a width of 0.4

mm, with  $70\mu\text{m}$  wide piezoresistive lines, which do not necessarily correspond to the limit of the laser process. Further miniaturization of the laser process would depend heavily of the accuracy of alignment of the stencil and the laser beam in the final release step. However, photolithography, followed by RIE of the polyimide could make miniaturization less challenging.

- Testing of the fabricated array of devices with the integrated electronics in the benchtop wind-tunnel and on the airfoil. The associated electronics would enable the simultaneous read-out from all the devices, which would give important information about the flow characteristics, including location of the stagnation point on the airfoil. This information would eventually be useful in flight-control experiments.
- A small, but important contribution could also result from a thorough analysis of the source of the stress-induced bending moments, which were briefly discussed in Section 6.5. The effect of temperature, humidity, deposition conditions etc., on the intrinsic stress could explain the behavior of the net residual stresses to a large extent.

In conclusion, the major objectives of this thesis are achieved through the laser based fabrication process developed. From a materials point of view, it has shown promise for the fabrication of a sensitive and robust flow sensor that could satisfy the requirements of the application.

## REFERENCES

- [1] ABOAF, J. A., “Stresses in SiO<sub>2</sub> films obtained from the thermal decomposition of tetraethylorthosilicate—effect of heat-treatment and humidity,” *Journal of The Electrochemical Society*, vol. 116, no. 12, pp. 1732–1736, 1969.
- [2] ALICIA, J., GABRIELA, B., and ANJA, B., “Polymeric cantilever-based biosensors with integrated readout,” *Applied Physics Letters*, vol. 89, no. 17, p. 173505, 2006.
- [3] ANHOJ, T. A., JORGENSEN, A. M., ZAUNER, D. A., and HUBNER, J., “The effect of soft bake temperature on the polymerization of SU-8 photoresist,” *Journal of Micromechanics and Microengineering*, vol. 16, no. 9, pp. 1819–1824, 2006.
- [4] ARNOLD, D. P., HERRAULT, F., ZANA, I., GALLE, P., PARK, J.-W., DAS, S., LANG, J. H., and ALLEN, M. G., “Design optimization of an 8 W, microscale, axial-flux, permanent-magnet generator,” *Journal of Micromechanics and Microengineering*, vol. 16, no. 9, pp. 290–296, 2006.
- [5] ASHAUER, M., GLOSCH, H., HEDRICH, F., HEY, N., SANDMAIER, H., and LANG, W., “Thermal flow sensor for liquids and gases based on combinations of two principles,” *Sensors and Actuators: A. Physical*, vol. 73, no. 1-2, pp. 7–13, 1999.
- [6] AUTHOR NOT SPECIFIED, “Biomimicry,” <http://www.wikipedia.org>, May 2008.
- [7] AUTHOR NOT SPECIFIED, “Bionics,” <http://www.wikipedia.org>, May 2008.
- [8] AUTHOR NOT SPECIFIED, “Electrically conducting liquid silicone rubber,” <http://www.wacker.com>, May 2008.
- [9] AUTHOR NOT SPECIFIED, “Interferometric modulator display,” <http://www.wikipedia.org>, May 2008.
- [10] AUTHOR NOT SPECIFIED, “mirasol<sup>TM</sup> display technology,” <http://www.qualcomm.com/technology/imod/>, May 2008.
- [11] AUTHOR NOT SPECIFIED, “Strain gauge,” <http://www.wikipedia.org>, 2008.
- [12] AUTHOR NOT SPECIFIED, “Unmanned aerial vehicle,” <http://www.wikipedia.org>, May 2008.
- [13] BACHMANN, D., SCHOBERLE, B., KUHNE, S., LEINER, Y., and HIEROLD, C., “Fabrication and characterization of folded SU-8 suspensions for mems applications,” *Sensors and Actuators: A. Physical*, vol. 130, pp. 379–386, 2006.

- [14] BLECKMANN, H., SCHMITZ, H., and VON DER EMDE, G., "Nature as a model for technical sensors," *Journal of Comparative Physiology A: Sensory, Neural, and Behavioral Physiology*, vol. 190, no. 12, pp. 971–981, 2004.
- [15] BRYZEK, J., "Impact of MEMS technology on society," *Sensors and Actuators: A. Physical*, vol. 56, no. 1-2, pp. 1–9, 1996.
- [16] BUSTILLO, J. M., HOWE, R. T., and MULLER, R. S., "Surface micromachining for microelectromechanical systems," *Proceedings of the IEEE*, vol. 86, no. 8, pp. 1552–1574, 1998.
- [17] CALLEJA, M., TAMAYO, J., NORDSTRM, M., and BOISEN, A., "Low-noise polymeric nanomechanical biosensors," *Applied Physics Letters*, vol. 88, p. 113901, 2006.
- [18] CHATZANDROULIS, S., TSEREPI, A., GOUSTOURIDIS, D., NORMAND, P., and TSOUKALAS, D., "Fabrication of single crystal Si cantilevers using a dry release process and application in a capacitive-type humidity sensor," *Microelectronic Engineering*, vol. 61, pp. 955–961, 2002.
- [19] CHEN, J., ENGEL, J., CHANG, M., and LIU, C., "3d out-of-plane flow sensor array with integrated circuits," *Proceedings of the 18th European Conference on Solid-State Transducers (Euroensors XVI)*, 2002.
- [20] CHEN, J., FAN, Z., ZOU, J., ENGEL, J., and LIU, C., "Two-dimensional micromachined flow sensor array for fluid mechanics studies," *Journal of Aerospace Engineering*, vol. 16, p. 85, 2003.
- [21] CHEN, J. E. and LIU, J. C., "Development of polymer-based artificial haircell using surface micromachining and 3d assembly," *TRANSDUCERS, Solid-State Sensors, Actuators and Microsystems, 12th International Conference on, 2003*, vol. 2, 2003.
- [22] CHEN, K. S., ZHANG, X., and LIN, S. Y., "Intrinsic stress generation and relaxation of plasma-enhanced chemical vapor deposited oxide during deposition and subsequent thermal cycling," *Thin Solid Films*, vol. 434, no. 1-2, pp. 190–202, 2003.
- [23] CHOI, S. O., RAJARAMAN, S., YOON, Y. K., WU, X., and ALLEN, M. G., "3-D patterned microstructures using inclined UV exposure and metal transfer micromolding," *Proc. Solid State Sensors, Actuators and Microsystems Workshop (Hilton Head, SC)*, 2006.
- [24] CUI, W., BICEN, B., HALL, N., JONES, S. A., DEGERTEKIN, F. L., and MILES, R. N., "Optical sensing in a directional MEMS microphone inspired by the ears of the parasitoid fly, *ormia ochracea*," *Micro Electro Mechanical Systems, 2006. MEMS 2006 Istanbul. 19th IEEE International Conference on*, pp. 614–617, 2006.

- [25] DAVIS, S. P., PRAUSNITZ, M. R., and ALLEN, M. G., "Fabrication and characterization of laser micromachined hollow microneedles," *TRANSDUCERS, Solid-State Sensors, Actuators and Microsystems, 12th International Conference on, 2003*, vol. 2, 2003.
- [26] DE BREE, H. E., LEUSSINK, P., KORTHORST, T., JANSEN, H., LAMMERINK, T. S. J., and ELWENSPOEK, M., "The  $\mu$ -flown: a novel device for measuring acoustic flows," *Sensors and Actuators: A. Physical*, vol. 54, no. 1-3, pp. 552–557, 1996.
- [27] DIJKSTRA, M., BAAR, J. J. v., WIEGERINK, R. J., LAMMERINK, T. S. J., BOER, J. H. D., and KRIJNEN, G. J. M., "Artificial sensory hairs based on the flow sensitive receptor hairs of crickets," *Journal of Micromechanics and Microengineering*, vol. 15, no. 7, p. S132, 2005.
- [28] DIJKSTRA, M., DE BOER, M. J., BERENSCHOT, J. W., LAMMERINK, T. S. J., WIEGERINK, R. J., and ELWENSPOEK, M., "Miniaturized flow sensor with planar integrated sensor structures on semicircular surface channels," *Micro Electro Mechanical Systems, 2007. MEMS. IEEE 20th International Conference on*, pp. 123–126, 2007.
- [29] DYER, S. E., GREGORY, O. J., AMONS, P. S., and SLOT, A. B., "Preparation and piezoresistive properties of reactively sputtered indium tin oxide thin films," *Thin Solid Films*, vol. 288, no. 1-2, pp. 279–286, 1996.
- [30] ENGEL, J., CHEN, J., FAN, Z., and LIU, C., "Polymer micromachined multimodal tactile sensors," *Sensors and Actuators: A. Physical*, vol. 117, no. 1, pp. 50–61, 2005.
- [31] ENGEL, J. M., CHEN, J., BULLEN, D., and LIU, C., "Polyurethane rubber as a MEMS material: characterization and demonstration of an all-polymer two-axis artificial hair cell flow sensor," *Micro Electro Mechanical Systems, 2005. MEMS 2005. 18th IEEE International Conference on*, pp. 279–282, 2005.
- [32] ENGEL, J. M., CHEN, J., CHEN, N., PANDYA, S., and LIU, C., "Development and characterization of an artificial hair cell based on polyurethane elastomer and force sensitive resistors," *Sensors, 2005 IEEE*, 2005.
- [33] ENGEL, J. M., CHEN, J., LIU, C., and BULLEN, D., "Polyurethane rubber all-polymer artificial hair cell sensor," *Microelectromechanical Systems, Journal of*, vol. 15, no. 4, pp. 729–736, 2006.
- [34] ENGEL, J. M., CHEN, N., RYU, K., PANDYA, S., TUCKER, C., YANG, Y., and LIU, C., "Multi-layer embedment of conductive and non-conductive PDMS for all-elastomer MEMS," *Solid State Sensors, Actuators, and Microsystems Workshop (Hilton Head, SC, June 2006)*, p. 3169, 2006.

- [35] FAN, Z., CHEN, J., ZOU, J., BULLEN, D., LIU, C., and DELCOMYN, F., "Design and fabrication of artificial lateral line flow sensors," *Journal of Micromechanics and Microengineering*, vol. 12, no. 5, pp. 655–661, 2002.
- [36] FRAZIER, A. B. and ALLEN, M. G., "Piezoresistive graphite/polyimide thin films for micromachining applications," *Journal of Applied Physics*, vol. 73, no. 9, p. 4428, 1993.
- [37] GELORME, J. D., COX, R. J., and GUTIERREZ, S. A. R., "Photoresist composition and printed circuit boards and packages made therewith," November 1989. U.S. Patent number 4,882,245.
- [38] GNATZY, W. and TAUTZ, J., "Ultrastructure and mechanical properties of an insect mechanoreceptor: Stimulus-transmitting structures and sensory apparatus of the cereal filiform hairs of gryllus," *Cell and Tissue Research*, vol. 213, no. 3, pp. 441–463, 1980.
- [39] GOOTEE, T. P., "Easy printed circuit board fabrication," <http://www.fullnet.com/tomg/gooteepc.htm>, May 2008.
- [40] GREGORY, O. J., SLOT, A. B., AMONS, P. S., and CRISMAN, E. E., "High temperature strain gages based on reactively sputtered AlN<sub>x</sub> thin films," *Surface and Coatings Technology*, vol. 88, no. 1, pp. 79–89, 1997.
- [41] HAQUE, M. S., NASEEM, H. A., and BROWN, W. D., "Residual stress behavior of thin plasma-enhanced chemical vapor deposited silicon dioxide films as a function of storage time," *Journal of Applied Physics*, vol. 81, no. 7, pp. 3129–3133, 1997.
- [42] HAUCK, D., "Pandora's box opened wide: UAVs carrying genetic weapons," *Research Paper: Defense Technical Information Center*, vol. 74, no. 13, pp. 3084–3095, 2002.
- [43] HENGYI, J., EROL, C. H., JASON, P. H., MURALIDHAR, K. G., YAO, F., KARLO, J., MATTHEW, S., and KYNAN, G., "Laser-LIGA for Ni microcantilevers," vol. 4935, pp. 263–271, SPIE, 2002. Smart Structures, Devices, and Systems 1.
- [44] HOLLENBERG, B. A., RICHARDS, C. D., RICHARDS, R., BAHR, D. F., and RECTOR, D. M., "A MEMS fabricated flexible electrode array for recording surface field potentials," *Journal of Neuroscience Methods*, vol. 153, no. 1, pp. 147–153, 2006.
- [45] HOLMES, A. S., "Laser fabrication and assembly processes for MEMS," *SPIE*, vol. 4274, p. 297, 2001.
- [46] HONG, S. J., CHOI, S., CHOI, Y., ALLEN, M., and MAY, G., "Characterization of low-temperature su-8 photoresist processing for mems applications," *IEEE Conf. Workshop ASMC 2004*, pp. 404–408, 2004.

- [47] HUANG, A. L., TAI, J., and HO, C. M., "Microsensors and actuators for macrofluidic control," *Sensors Journal, IEEE*, vol. 4, no. 4, pp. 494–502, 2004.
- [48] HUANG, J. C., "Carbon black filled conducting polymers and polymer blends," *Advances in Polymer Technology*, vol. 21, no. 4, pp. 299–313, 2002.
- [49] HUCK, W. T. S., BOWDEN, N., ONCK, P., PARDOEN, T., HUTCHINSON, J. W., and WHITESIDES, G. M., "Ordering of spontaneously formed buckles on planar surfaces," *Langmuir*, vol. 16, no. 7, p. 34973501, 2000.
- [50] JIANG, F., LEE, G. B., TAI, Y. C., and HO, C. M., "A flexible micromachining-based shear-stress sensor array and its application to separation-point detection," *Sensors and Actuators: A. Physical*, vol. 79, no. 3, pp. 194–203, 2000.
- [51] JIANG, F., TAI, Y. C., WALSH, K., TSAO, T., LEE, G. B., and HO, C. M., "A flexible MEMS technology and its first application to shearstress sensor skin," *Micro Electro Mechanical Systems, 1997. MEMS'97, Proceedings, IEEE., Tenth Annual International Workshop on*, pp. 465–470, 1997.
- [52] JIANG, F., XU, Y., WENG, T., HAN, Z., and TAI, Y. C., "Flexible shear stress sensor skin for aerodynamics applications," *Micro Electro Mechanical Systems, 2000. MEMS 2000. 13th IEEE Annual International Conference on*, pp. 364–369, 2000.
- [53] KIM, G., PARK, C., SEO, D. S., and HONG, S. J., "Delamination analysis of low-temperature processed SU-8 photoresist for MEMS device fabrication," *Key Engineering Materials*, vol. 345, pp. 1397–1400, 2007.
- [54] KIM, J. and LEE, H. H., "Wave formation by heating in thin metal film on an elastomer," *Journal of Polymer Science Part B Polymer Physics*, vol. 39, no. 11, pp. 1122–1128, 2001.
- [55] KIM, J. and XU, X., "Excimer laser fabrication of polymer microfluidic devices," *Journal of Laser Applications*, vol. 15, p. 255, 2003.
- [56] KLEJWA, N., HARJEE, N., KWON, R., COULTHARD, S. M., and PRUITT, B. L., "Transparent SU-8 three-axis micro strain gauge force sensing pillar arrays for biological applications," *Solid-State Sensors, Actuators and Microsystems Conference, 2007. TRANSDUCERS 2007. International*, pp. 2259–2262, 2007.
- [57] KNIGHT, M. J., "Effect of structure on the piezoresistive properties of thin metal films," *Journal of Vacuum Science and Technology*, vol. 6, p. 706, 1969.
- [58] LACOUR, S. P., JONES, J., SUO, Z., and WAGNER, S., "Design and performance of thin metal film interconnects for skin-like electronic circuits," *Electron Device Letters, IEEE*, vol. 25, no. 4, pp. 179–181, 2004.



- [59] LACOUR, S. P., WAGNER, S., HUANG, Z., and SUO, Z., "Stretchable gold conductors on elastomeric substrates," *Applied Physics Letters*, vol. 82, p. 2404, 2003.
- [60] LANDOIFA, M. A. and JACOBS, G. A., "Direction sensitivity of the filiform hair population of the cricket cercal system," *J Comp Physiol A*, vol. 177, pp. 759–766, 1995.
- [61] LANGE, D., HAGLEITNER, C., HIERLEMANN, A., BRAND, O., and BALTES, H., "Complementary metal oxide semiconductor cantilever arrays on a single chip: mass-sensitive detection of volatile organic compounds," *Anal. Chem.*, vol. 74, no. 13, pp. 3084–3095, 2002.
- [62] LEE, J. W., PARK, J.-H., and PRAUSNITZ, M. R., "Dissolving microneedles for transdermal drug delivery," *Biomaterials*, vol. 29, no. 13, pp. 2113–2124, 2008.
- [63] LEI, J. F. and WILL, H. A., "Thin-film thermocouples and strain-gauge technologies for engine applications," *Sensors and Actuators: A. Physical*, vol. 65, no. 2-3, pp. 187–193, 1998.
- [64] LEWIS, N. S., LONERGAN, M. C., SEVERIN, E. J., DOLEMAN, B. J., and GRUBBS, R. H., "Array-based vapor sensing using chemically sensitive carbon black-polymer resistors," *Proceedings of SPIE*, vol. 3079, p. 660, 1997.
- [65] LI, J., CHEN, J., and LIU, C., "Micromachined biomimetic sensor using modular artificial hair cells," *Nano Space 2000*, 2000.
- [66] LI, T., HUANG, Z., SUO, Z., LACOUR, S. P., and WAGNER, S., "Stretchability of thin metal films on elastomer substrates," *Applied Physics Letters*, vol. 85, p. 3435, 2004.
- [67] LINDER, V., GATES, B. D., RYAN, D., PARVIZ, B. A., and WHITESIDES, G. M., "Water-soluble sacrificial layers for surface micromachining," *Small*, vol. 1, no. 7, pp. 730–736, 2005.
- [68] LORENZ, H., DESPONT, M., FAHRNI, N., LABIANCA, N., RENAUD, P., and VETTIGER, P., "SU-8: a low-cost negative resist for mems," *J. Micromech. Microeng*, vol. 7, no. 3, p. 121124, 1997.
- [69] LORUSSI, F., ROCCHIA, W., SCILINGO, E., TOGNETTI, A., and DE ROSSI, D., "Wearable, redundant fabric-based sensor arrays for reconstruction of body segment posture," *Sensors Journal, IEEE*, vol. 4, no. 6, pp. 807–818, Dec. 2004.
- [70] LU, M., BERMAK, A., and LEE, Y. K., "Fabrication technology of piezoresistive conductive PDMS for micro fingerprint sensors," *Micro Electro Mechanical Systems, 2007. MEMS. IEEE 20th International Conference on*, pp. 251–254, 2007.

- [71] MA, R. H., LEE, C. Y., WANG, Y. H., and CHEN, H. J., "Microcantilever-based weather station for temperature, humidity and flow rate measurement," *Microsystem Technologies*, pp. 1–7, 2007.
- [72] MAEDA, M. and ITSUMI, M., "Stress evaluation of chemical vapor deposited silicon dioxide films," *Physica B: Condensed Matter*, vol. 324, no. 1-4, pp. 167–172, 2002.
- [73] MAILLY, F., GIANI, A., BONNOT, R., TEMPLE-BOYER, P., PASCAL-DELANNOY, F., FOUCARAN, A., and BOYER, A., "Anemometer with hot platinum thin film," *Sensors and Actuators: A. Physical*, vol. 94, no. 1-2, pp. 32–38, 2001.
- [74] MCFARLAND, A. W., POGGI, M. A., BOTTOMLEY, L. A., and COLTON, J. S., "Injection moulding of high aspect ratio micron-scale thickness polymeric microcantilevers," *Nanotechnology*, vol. 15, no. 11, pp. 1628–1632, 2004.
- [75] MILLER, J. C., *Laser ablation: principles and applications*. Springer, Berlin, 1994.
- [76] MOSS, E. D., HAN, A., and FRAZIER, A. B., "A fabrication technology for multi-layer polymer-based microsystems with integrated fluidic and electrical functionality," *Sensors and Actuators: B. Chemical*, vol. 121, no. 2, pp. 689–697, 2007.
- [77] OZAKI, Y., OHYAMA, T., YASUDA, T., and SHIMOYAMA, I., "An air flow sensor modeled on wind receptor hairs of insects," *Micro Electro Mechanical Systems, 2000. MEMS 2000. The Thirteenth Annual International Conference on*, pp. 531–536, 2000.
- [78] PARK, S., KIM, S., KIM, S., and KIM, Y., "A flow direction sensor fabricated using MEMS technology and its simple interface circuit," *Sensors and Actuators: B. Chemical*, vol. 91, no. 1-3, pp. 347–352, 2003.
- [79] PARKER, R. L. and KRINSKY, A., "Electrical resistance-strain characteristics of thin evaporated metal films," *Journal of Applied Physics*, vol. 34, no. 9, p. 2700, 1963.
- [80] PENG, W., FENG, X., TIANHUI, D., and YUANZHEN, Q., "Time dependence of electrical resistivity under uniaxial pressures for carbon black/polymer composites," *Journal of Materials Science*, vol. 39, no. 15, pp. 4937–4939, 2004.
- [81] PETERSEN, K. E., "Silicon as a mechanical material," *Proceedings of the IEEE*, vol. 70, no. 5, pp. 420–457, 1982.
- [82] PFANN, W. G. and THURSTON, R. N., "Semiconducting stress transducers utilizing the transverse and shear piezoresistance effects," *Journal of Applied Physics*, vol. 32, no. 10, p. 2008, 1961.

- [83] PHAM, N. P., BURGHARTZ, J. N., and SARRO, P. M., "Spray coating of photoresist for pattern transfer on high topography surfaces," *Journal of Micromechanics and Microengineering*, vol. 15, no. 4, pp. 691–697, 2005.
- [84] PHILIP, B., ABRAHAM, J. K., CHANDRASEKHAR, A., and VARADAN, V. K., "Carbon nanotube/PMMA composite thin films for gas-sensing applications," *Smart Materials and Structures*, vol. 12, no. 6, pp. 935–939, 2003.
- [85] RAJANNA, K., MOHAN, S., NAYAK, M. M., GUNASEKARAN, N., and MUTHUNAYAGAM, A. E., "Pressure transducer with Au-Ni thin-film strain gauges," *Electron Devices, IEEE Transactions on*, vol. 40, no. 3, pp. 521–524, 1993.
- [86] RAJARAMAN, S., CHOI, S. O., SHAFER, R. H., ROSS, J. D., VUKASINOVIC, J., CHOI, Y., DEWEERTH, S. P., GLEZER, A., and ALLEN, M. G., "Microfabrication technologies for a coupled three-dimensional microelectrode, microfluidic array," *Journal of Micromechanics and Microengineering*, vol. 17, no. 1, pp. 163–171, 2007.
- [87] RAJARAMAN, S., MCCLAIN, M. A., CHOI, S. O., ROSS, J. D., DEWEERTH, S. P., LAPLACA, M. C., and ALLEN, M. G., "Three-dimensional metal transfer micromolded microelectrode arrays (MEAs) for in-vitro brain slice recordings," *Solid-State Sensors, Actuators and Microsystems Conference, 2007. TRANSDUCERS 2007. International*, pp. 1251–1254, 2007.
- [88] RAMADOSS, R., LEE, S., LEE, Y. C., BRIGHT, V. M., and GUPTA, K. C., "Flexible polyimide film based high isolation RF MEMS switches fabricated using printed circuit processing techniques," *Micro Electro Mechanical Systems, 2005. MEMS 2005. 18th IEEE International Conference on*, pp. 179–182, 2005.
- [89] SCHEER, A. V. and LAST, T., "Process for preparing non-porous membrane layers," December 1990. U.S. Patent number 4,980,235.
- [90] SCHMITZ, G. J., BRUCKER, C., and JACOBS, P., "Manufacture of high-aspect-ratio micro-hair sensor arrays," *Journal of Micromechanics and Microengineering*, no. 10, p. 1904, 2005.
- [91] SENTURIA, S., *Microsystem design*. Kluwer Academic Press, 2002.
- [92] SHAHINPOOR, M., BAR-COHEN, Y., SIMPSON, J. O., and SMITH, J., "Ionic polymer-metal composites (ipmcs) as biomimetic sensors, actuators and artificial muscles-a review," *Smart Mater. Struct*, vol. 7, no. 6, 1998.
- [93] SHIMOYAMA, I., HOSHINO, K., OZAKI, Y., TAMAKI, S., TAKEUCHI, S., and YASUDA, T., "MEMS meets insects," *Proceedings of 11th International Conference on Solid State Sensors and Actuators*, vol. 9, p. 20, 2001.

- [94] SHIMOZAWA, T., KUMAGAI, T., and BABA, Y., "Structural scaling and functional design of the cercal wind-receptor hairs of cricket," *Journal of Comparative Physiology A: Sensory, Neural, and Behavioral Physiology*, vol. 183, no. 2, pp. 171–186, 1998.
- [95] SMITH, C. S., "Piezoresistance effect in germanium and silicon," *Physical Review*, vol. 94, no. 1, pp. 42–49, 1954.
- [96] SU, Y., EVANS, A. G. R., and BRUNNSCHWEILER, A., "Micromachined silicon cantilever paddles with piezoresistive readout for flow sensing," *J. Micromech. Microeng.*, vol. 6, no. 1, pp. 69–72, 1996.
- [97] THAYSEN, J., YALCINKAYA, A. D., VETTIGER, P., and MENON, A. K., "Polymer-based stress sensor with integrated readout," *Journal of Physics D Applied Physics*, vol. 35, no. 21, pp. 2698–2703, 2002.
- [98] TOKO, K., "Measurement of taste and smell using biomimetic sensor," *Micro Electro Mechanical Systems, 2004. 17th IEEE International Conference on.(MEMS)*, pp. 201–207, 2004.
- [99] TURBAN, G. and RAPEAUX, M., "Dry etching of polyimide in O<sub>2</sub>-CF<sub>4</sub> and O<sub>2</sub>-SF<sub>6</sub> plasmas," *Journal of the Electrochemical Society*, vol. 130, no. 11, pp. 2231–2236, 1983.
- [100] VAN BAAR, J. J., WIEGERINK, R. J., LAMMERINK, T. S. J., KRIJNEN, G. J. M., and ELWENSPOEK, M., "Micromachined structures for thermal measurements of fluid and flow parameters," *Journal of Micromechanics and Microengineering*, vol. 11, no. 4, pp. 311–318, 2001.
- [101] VOET, A. and COOK, F. R., "Investigation of carbon chains in rubber vulcanizates by means of dynamic electrical conductivity," *Rubber Chem Technol*, vol. 41, pp. 1207–1214, 1968.
- [102] WANG, Y. H., HSUEH, T. H., MA, R. H., LEE, C. Y., CHOU, P. C., and TSAI, C. H., "A microcantilever-based gas flow sensor for flow rate and direction detection," 2008.
- [103] WANG, Y. H., LEE, C. Y., and CHIANG, C. M., "A MEMS-based air flow sensor with a free-standing micro-cantilever structure," *Sensors*, vol. 7, pp. 2389–2401, 2007.
- [104] WIEGERINK, R. J. F., JAGANATHARAJA, A., IZADI, R. K., LAMMERINK, N., KRIJNEN, T. S. J., and GIJS, J. M., "Biomimetic flow-sensor arrays based on the filiform hairs on the cerci of crickets," *Sensors, 2007 IEEE*, pp. 1073–1076, 2007.
- [105] WRIGHT, O. and WRIGHT, W., "Flying-machine," December 1906. U.S. Patent number 821,393.

- [106] WU, X., ZHAO, Y., YOON, Y. K., CHOI, S. O., PARK, J. H., and ALLEN, M. G., “Wafer-scale micromolding of unitary polymeric microstructures with simultaneously formed functional metal surface,” *Proceedings of  $\mu$ TAS 2005 conference*, pp. 09–13, 2005.
- [107] XIA, Y. and WHITESIDES, G. M., “Soft lithography,” *Annual Reviews in Materials Science*, vol. 28, no. 1, pp. 153–184, 1998.
- [108] YAMAGUCHI, K., BUSFIELD, J. J. C., and THOMAS, A. G., “Electrical and mechanical behavior of filled elastomers. i. the effect of strain,” *Journal of Polymer Science, Part B, Polymer Physics*, vol. 41, no. 17, pp. 2079–2089, 2003.
- [109] YANG, Y., CHEN, N., TUCKER, C., ENGEL, J., PANDYA, S., and LIU, C., “From artificial hair cell sensor to artificial lateral line system: Development and application,” *Micro Electro Mechanical Systems, 2007. MEMS. IEEE 20th International Conference on*, pp. 577–580, 2007.
- [110] ZHANG, X. R. and XU, X., “Development of a biosensor based on laser-fabricated polymer microcantilevers,” *Applied Physics Letters*, vol. 85, p. 2423, 2004.
- [111] ZHANG, X. W., PAN, Y., ZHENG, Q., and YI, X. S., “Time dependence of piezoresistance for the conductor-filled polymer composites,” *Journal of Polymer Science Part B Polymer Physics*, vol. 38, no. 21, pp. 2739–2749, 2000.
- [112] ZHAO, Y., YOON, Y. K., and ALLEN, M. G., “Metal-transfer-micromolded RF components for system-on-package (SOP),” *Electronic Components and Technology Conference, 2007. ECTC’07. Proceedings. 57th*, pp. 1877–1883, 2007.
- [113] ZHAO, Y., YOON, Y. K., WU, X., and ALLEN, M. G., “Metal-transfer-micromolding of air-lifted RF components,” *Solid-State Sensors, Actuators and Microsystems Conference, 2007. TRANSDUCERS 2007. International*, pp. 659–662, 2007.